Next Generation Rechargeable Zn-Air Batteries: Sustainable and Abundant Materials

Christensen, Mathias Kjærgård

Publication date:
2018

Document Version
Publisher's PDF, also known as Version of record

Next Generation Rechargeable Zn-Air Batteries:

Sustainable and Abundant Materials

Mathias Kjærgaard Christensen
November 30 - 2018

DTU Energy Conversion
Department of Energy Conversion and Storage

Next Generation Rechargeable Zn-Air Batteries: Sustianable and Aboundant Materails

Author
Mathias Kjærgaard Christensen
Department of Energy Conversion and Storage
Technical University of Denmark
E-mail: mkch@dtu.dk

Main Supervisor
Prof. Poul Norby
Department of Energy Conversion and Storage
Technical University of Denmark

Co-supervisor
Prof. Tejs Vegge
Department of Energy Conversion and Storage
Technical University of Denmark

Co-supervisor
Prof. Harry Hoster
Department of Chemistry
Lancaster University

Preface

This thesis is submitted in candidacy for the PhD degree from the Technical University of Denmark, DTU. The work was carried out between the 1st of December 2015 and the 30th of November 2018, initially at the section for atomic scale modelling, ASC, and since 1st of January 2017 at the section for Electrochemical Materials, EMA, both sections at DTU.

A part of the project was carried out at Lancaster University's Department of Chemistry, from November 2017 to February of 2018. The main supervisor of the project was Prof. Poul Norby, with co-supervision from Prof. Tejs Vegge, head of the ASC section, and Prof. Harry Hoster, director of energy Lancaster. The project was financially supported by the Horizon 2020 Framework project ZAS, grant number 646186. The synchrotron XRD experiments were possible due to funding from MAX4ESSFUN and DANSCATT.

Abstract

Due to the increased focus on implementing renewable energy and the consequences of the intermittent aspects of these technologies, energy storage has received a lot of attention. Heavy technological progression in recent decades resulted in an apparent solution in the form of batteries. Despite the success of the Li-ion batteries and its variants, there is a push towards developing high capacity, low-cost batteries due to the sheer amount of energy that needs to be stored if the energy sector commits to a full transition to renewable energy generation.

A candidate for this role is the Zn-air battery, a battery with high energy density made from cheap and abundant materials that are already available commercially, but only as a primary battery. Aside from difficulties in recharging, the Zn-air batteries suffer form self-corrosion of the anode in alkaline media, dendrite formation. The aim of this thesis was to investigate Zn-air batteries using in situ techniques and thereby provide the information required to meet these challenges.

A flow cell setup was developed to investigate dissolution of typical Zn-air anode current collectors. It was found that Ti, Cu, Sn and W are all suitable current collectors in alkaline media. Ti appeared to be the most stable, while Cu, Sn and W all dissolve quickly above the dissolution potential for Zn, with the two latter materials dissolving the fastest.

Using a Differential Electrochemical Mass Spectrometer (DEMS), Zn-air batteries with four different electrolytes were investigated with the goal of correlating electrochemical properties to gas evolution. Electron numbers were determined for a KOH electrolyte and an optimised KOH electrolyte with the additives KF and K_2CO_3. Furthermore, a $ZnCl_2^-$ electrolyte at pH 8 and a neutral electrolyte composed of Zn(TFSI) and Li(TFSI) were found not to evolve O_2.

Using the same technique, the effect of dopants on the Hydrogen Evolution Reaction (HER) at a Zn surface was investigated. It was determined that a combination of In and Bi was superior to the dopants by themselves. It was also shown how Ag has detrimental effects, as it enhances the HER while it inhibits the Oxygen Evolution Reaction (OER). These results were used to support a Density Functional Theory (DFT) model that explains why these dopants affect these properties.

Finally, a Zn-air capillary cell was developed. Using spatially and time-resolved X-Ray Diffraction (XRD) synchrotron radiation, it was demonstrated that a Zn/ZnO paste anode developed to promote homogeneous ZnO deposition over time actually lead to inhomogeneous distribution of Zn and ZnO, with the former being preferred in the interface between the anode and electrolyte. The results were supported by time-resolved X-ray computed tomography.

Resume

I de seneste år, hvor bæredygtig energi er blevet mere og mere almindeligt, og videnskabelige undersøgelser viser, at implementerering af bæredygtig energi skal gå endnu hurtigere, er der kommet et stort fokus på energilagring. En ulempe ved de mest normale bæredygtige energiformer er nemlig, at den ikke kan styres centralt og tilpasses det øjeblikkelige forbrug, som samfundet har. Den teknologiske udvikling har i den forbindelse gjort en mulig løsning, batterier, meget nærværende i vores dagligdag. Udfordringen er dog, at den dominerende batteritype lige nu, Li-ion-batteriet, forlader sig på ressourcer som er relativt dyre i forhold til, hvor meget der skal bruges til at lagre en betydelig del af vores energibehov.

Et alternativ er Zn-luft-batteriet, der har eksisteret kommercielt siden 1936 og i dag bruges i høreapparater. Zn-luft-batterier har høj energitæthed og samtidig er Zn relativt billigt. De fungerer ved at optage ilt fra luften som via en katalysator bliver opløst som hydroxid-ioner i batteriet der sammen med Zn danner ZnO. Det er gennem dette princip, at typen opnår høje energitætheder. Denne batteritype er dog et såkaldt primærtbatteri - det kan ikke genoplades elektrisk. For at være en teknisk fornuftig løsning, skal batterierne gerne kunne oplades mindst 200 gange uden at miste mere end 20 procent kapacitet.

I dette projekt er der fokuseret på at forstå og bevise, hvilke forhindringer der er i forhold til at opnå det antal genopladninger. For at forstå disse udfordringer benyttes der primært in-situ teknikker, der kan korrelere elektrokemiske parametre med et anden fysisk parameter - som for eksempel tryk. På den måde kan det belyses, hvordan batteriet opfører sig i de forskellige faser at dets operation.

Da disse batterier under afladning optager og binder ilt i deres anode og afgiver det under opladning, kan man anvende et differentielt elektroke-

misk massespektrometer til at kvantificere sammenhængen mellem den strøm der passerer gennem batteriet og den mængde gas der forbruges og frigives. Denne teknik blev brugt til at undersøge et lille udvalg af elektrolytter, inklusiv den mest almindelige, der bliver brugt i feltet. Denne teknik benyttes også til at undersøge, hvordan legeringer af Zn, der indeholder In og Bi, er gavnligt i forhold til at mindske udvikling af brint fra batteriet som følge af den meget basiske elektrolyt. Disse målinger bliver sammenlignet med teoretiske udregninger, der beskriver, hvordan Zn-overfalden, med legering, opfører sig på fundementalt niveau.

Ved at bygge fungerende Zn-luft-batterier i et kapilarrør benyttes røngtendiffraktion til at demonstrere, hvordan en Zn/ZnO elektrode ville ændre form under af- og opladning. Det demonstreres, hvordan der i hele prøven er ubalance i, hvor hurtigt afladning og opladningsprodukt bliver konverteret, men hvordan der lokalt er endnu større ubalance i Zn/ZnO forholdet med en overvægt af Zn i toppen af anoden. Disse målinger understøttes med røntgentomografi.

Via elektrokemisk cyclisk voltametri, CV, vises det at den basiske elektrolyt kan korrodere de resterende dele i batteriet over tid. Disse målinger understøttes ved brug af en kombination af CV og optisk spektrometri kan korrelere strømmen fra CV-teknikken med en koncentration af det opløse materiale.

Acknowledgements

First and foremost, I have to thank my main supervisor Prof. Poul Norby. It is hard to overstate how much I enjoyed and learned from our many conversations about batteries, X-rays, science and many other subjects. I am grateful for your open door policy, and all the quick informal meeting we have had over the past three years. They have been invaluable, especially in the final months. Your optimism and interest in all things science was encouraging when things, inevitably, did not go as planned.

I am also very grateful to Prof. Tejs Vegge for great academic discussions and advice. I always benefited from our meetings, your feedback and the advice you provided. It constantly challenged me and brought me forward.

The final member of my supervisor team, Prof. Harry Hoster, who during my time at Lancaster University provided exciting challenges, advice and encouragement, both on work and life in general.

A special mention to Jonathan Højberg. I enjoyed building the DEMS with you, which now feels like a long time ago. I am sure I would never have had the PhD-experience if it were not for that project. Thank you for that opportunity.

I also have to express my gratitude to Shahin Nikman, who throughout the last three years has been a great friend and collaborator. I enjoyed the time we spent in the laboratory at Risø, as well as at Lancaster University, all the discussions about Zn-air batteries and everything else. I will miss going to the pub after work with you.

To all the members of the ZAS project, who were a constant source of great discussions, challenges and nice atmosphere at our projects meetings. Of these members I have to thank Alexander Kube from DLR and

Kaushik Jayasayee from SINTEF for their helpfulness and many great conversations.

To all my wonderful colleagues at DTU, present and former, who have made the three years feel like they went by in an instant. Especially Doris who was always helpful and patient when I needed to vent my frustrations about science, lab-problems, Python or life in general. Also Jette and Katrine for all the coffee breaks, lunches and good times. I look forward to seeing you outside work. I also have to thank former colleagues Ane, Mie and Kristian, who when I started taught me everything there was to know about batteries and working at Risø. Also thanks to my office mates Anastasiia, Prasanna and Jessica. Also thanks to the secretaries Anne, Karina and research technician Mike Wichmann, for all the times you helped me fix problems, big and small, thank you.

To my mom and dad for more than once asking me about my project and listening to answers that were longer and more complicated than necessary. Especially when I was frustrated about a leaking O-ring, short-circuits and workloads.

Finally, to Mette Signe, my MS, for your support and understanding when all I could think about was batteries and my experiments. Thank you for visiting me while I was in Lancaster, supporting my long hours in the office and listening patiently to, most of, my explanation about what I was currently working on. I love you.

List of Publications

This thesis includes following papers:

Paper I
Combined DFT and Differential Electrochemical Mass Spectrometry Investigation of the Effect of Dopants in Secondary Zinc-Air Batteries.
Steen Lysgaard, **Mathias K. Christensen**, Heine A. Hansen, Juan Maria Garcia Lastra, Poul Norby and Tejs Vegge.
Status: Published in Chem Sus Chem, march 2018

Paper II
Transformation and migration in secondary Zn-air batteries studied by in In-situ synchrotron X-ray diffraction and X-ray tomography.
Mathias Kjaerrgaard Christensen, Jette Katja Mathiesen, Søren Bredmose and Poul Norby
Status: Submitted to Journal of Materials Chemistry A

Paper III
DEMS characterisation of Zn-air Batteries
Mathias K. Christensen and Poul Norby
Status: In manuscript

Not includes in this thesis:
In Situ Analysis of the Li-O_2 Battery with Thermally Reduced Graphene Oxide Cathode: Influence of Water Addition.
Mie Møller Storm, **Mathias Kjaergaard Christensen**, Reza Younesi, and Poul Norby
Status: Published in ACS Journal of Physical CHemistry, 2016

Comment on my contribution to the appended list of papers

Paper I
All of the experimental work, analysis of said experimental work and writing about this part. The DFT simulations and main part of writing was done by Steen Lysgaard. I am the second author of this paper.

Paper II
All of the experimental work apart from configuring the beam parameters parameters at XRD beamline and for the tomography experiments. Also performed the analysis and the main part of writing. I am the first author of this paper.

Paper III
All of the experimental work, analysis and writing. I am the first author of this paper.

List of Acronyms and Abbreviations

AEI	Anode Electrolyte Interface
CMC	Carboxymethyl Cellulose
CV	Cyclic Voltametry
DEMS	Differential Electrochemical Mass Spectrometry
EV	Electrical Vehicles
HER	Hydrogen Evolution Reaction
ICE	Internal Combustion Engine
ICP-OES	Inductively Coupled Plasma - Optical Emission Spectroscopy
IPCC	International Panel on Climate Change
MS	Mass Spectrometer
NCO	$NiCo_2O_4$
OCV	Open Circuit Voltage
OER	Oxygen Evolution Reaction
ORR	Oxygen Reduction Reaction
XRD	X-Ray Diffraction

Table 1: List of acronyms

Contents

Chapter 1

Introduction

A defining challenge of the 21st century is addressing climate change. The International Panel on Climate Change (IPCC) has estimated that the anthropogenic emission of greenhouse gasses has caused an increase in the global average temperature by approximately 1 °C compared to pre-industrial levels [1]. The heating originates from increased levels of CO_2 and other greenhouse gasses in the atmosphere. The primary emission of greenhouse gasses originates from the use of fossil fuel in energy production and manufacturing of chemicals, plastic products and other products [2]. With the demand for energy and electricity expected to increase towards the middle of the century, the temperature could increase beyond the limit of 1.5 °C agreed upon in the Paris accord. While the transition to renewable energy has been underway since the previous century, the IPCC recommends even further-reaching reforms to the energy sector [1]. This is especially true since the energy consumption, and thus CO_2-emissions, of the world is still increasing, due to the population of developing countries getting access to the energy grid. In 2017, global annual energy consumption rose 2.1 %, with almost 40 % of this being driven by China and India. One quarter of this increased energy demand was met by renewable energy and a few percent by nuclear. As a result, the CO_2 emission rose by 1.4 % [3]. By 2050, the energy demand will have increased even further to 43 TW[4] and will increase even more towards 2100 [5].
Aside from climate change, there are other reasons to decrease reliance on fossil fuels, such as the resources being tied up in geopolitical issues, scarcity and economics.

1.1 The Need for Energy Storage

The energy sector can follow a number of paths to reduce carbon emissions, such as increasing efficiency and employing low carbon content fuel, but ultimately fossil fuel will have to be replaced by renewable energy sources. The challenge is that renewable energy sources, such as pumped hydroelectricity, while providing storage, require special geographical conditions. Photovoltaics and wind power are intermittent sources and will only produce power during the day or under windy conditions. It is obvious that lack of power, when required, is problematic, but so is excess of power when there is no demand on the grid. The energy producers require a return on investment and the grid can be adversely affected. In some cases, if the grid cannot move the power from one region to another, the grid will still be affected even if there is sufficient power available. The degree to which renewable energy can be introduced into a power grid therefore depends on the grid and how it is managed. Grid challenges related to intermittent renewable energy penetration can appear at 20 % integration of renewable energy content [6]. At higher penetrations, the energy price drops dramatically on occasions with high generation and low demand, as seen in Figure 1.1 [7].

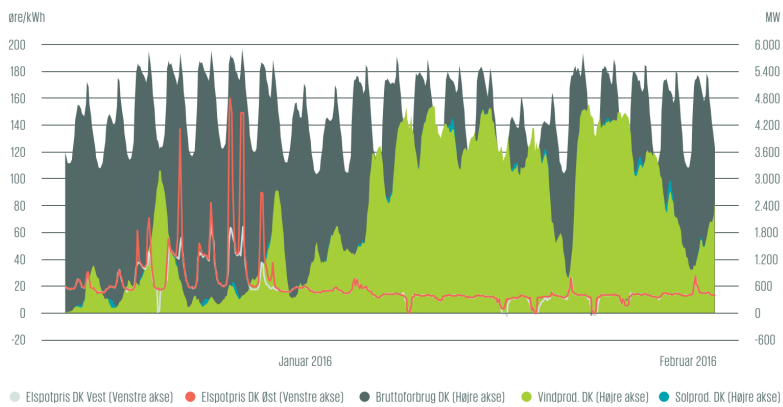

Figure 1.1: The electricity price in the two electricity grids in Denmark for the months January and February 2016 compared to energy consumption (dark green), wind power production (light green) and solar power production (blue). Taken from [7].

Storing energy for use during peak demand is known as peak-shaving and is a proven business case for batteries [8]. For other markets in energy trading, such as arbitrage or storing energy for other seasons within the

grid, prices would have to decrease dramatically due to the large amount of material required to manufacture such batteries. For this purpose, only abundant and cheap materials will be economically feasible [9].

However, electricity is just a part of the total energy consumption. In areas such as transport, there is a heavy focus on internal combustion engine (ICE) cars to be replaced by electric vehicles (EVs). Subsidisation could be a means of introducing more EVs, but generally better batteries are required. Gasoline is a very good energy carrier with a specific energy density of 12.3 kWh/kg and an energy density of 9.0 kWh/L. However, ICE rely on Carnot processes, which means the theoretical maximum energy that can be used to perform work, i.e. move the car, is limited by the temperature difference between the cool and hot temperature reservoir. Conventional Li-ion batteries, which use a $LiCoO_2$ cathode, have a theoretical energy density of 470 Wh/kg and are projected to have a practical maximum of 400 Wh/kg [10]. For airplanes, where weight and space demands are even more severe, the development of even better energy storage technologies is necessary.

Regardless of the application, there is a need to develop new technologies for energy storage. Current battery technologies, and to a large degree Li-ion, are prevalent in the conversation, but over time it is likely that different applications will favour different technologies, such as fuel cells, supercapacitors, synthetic fuel from electrolysis and other battery chemistries and types.

1.2 Battery Technology

The commonly used word *battery* actually refers to one or more electrochemical cells that are electrically connected to allow them to act as a combined power source. An electrochemical cell consists of several parts: anode, cathode, electrolyte, separator, casing and connectors. In this document, the words *battery* and *cell* will appear interchangeably, due to the fact that all batteries herein consist of a single electrochemical cell. The three main parts of an electrochemical cell are:

- Anode - The negative electrode: A material that is oxidised and delivers electrons to the circuit during discharge of the cell.
- Cathode - The positive electrode: The material that is reduced and accepts electrons during discharge of the cell.

- Electrolyte - The ionically conducting medium: The medium that passes ions between the electrodes to balance charge.

These definitions apply to the spontaneous reaction in the electrochemical cells. Battery cells where these reactions are irreversible are called primary batteries, *i.e.* non-rechargeable. Systems where the reactions can be reversed are called secondary batteries and are rechargeable. However, this implies that the cathode and anode switch places due to oxidation and reduction now occurring at the opposite side. In the present document, the terms will be applied as though the studied cells are always discharging [11].

The first battery created was the voltaic pile, described by Alessandro Volta in 1799, and is essentially a Cu-Zn battery. Since then a plethora of batteries have been developed with different capacities, geometries and materials. Today the most prevalent battery is the Li-ion battery that was developed in the 1991 [12], which offers excellent capacity in a small form factor and retains performance over hundreds of cycles.

The primary characteristics of a good battery are high specific energy, high discharge voltage, reliable cyclability and high specific power. The ideal battery would perform well in all of these parameters, but as these a interconnected, the ideal battery for an specific application has to be optimised for that application. Achieving higher capacity could be achieved by employing a larger anode, but this would be detrimental to the power output due to transport limitations in the electrodes. This is a fundamental challenge for most battery types, as illustrated by the Ragone plot in Figure 1.2.

1.3 Metal-Air Batteries

The family of batteries know as metal-air batteries can obtain very high theoretical energy densities and capacities. They do so by foregoing the need for heavy intercalation electrodes, relying instead of pure metal anodes. On the positive side of the battery there is only an air cathode that contributes to the weight, as the oxygen participating in the cathode reactions is outside the battery. As such, the resulting electrochemical device is very light in its charged state as it will gain weight during discharge as it consumes oxygen. Capacities are therefore generally given as open or closed, with the latter including the weight of oxygen.

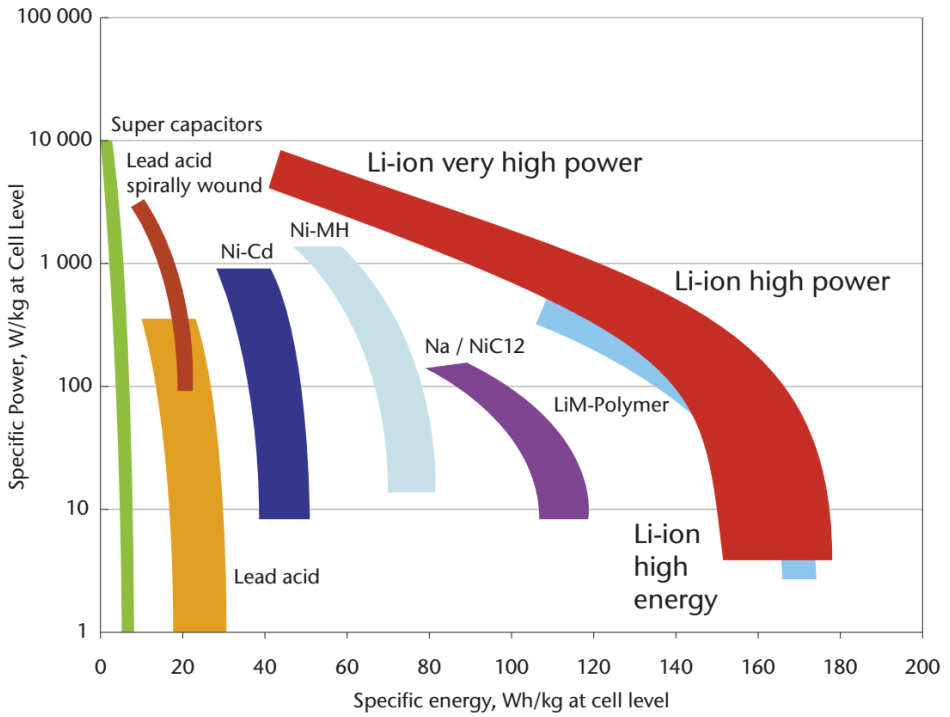

Figure 1.2: A Ragone plot that describes the relation between specific energy and -power for different battery technologies.[13]

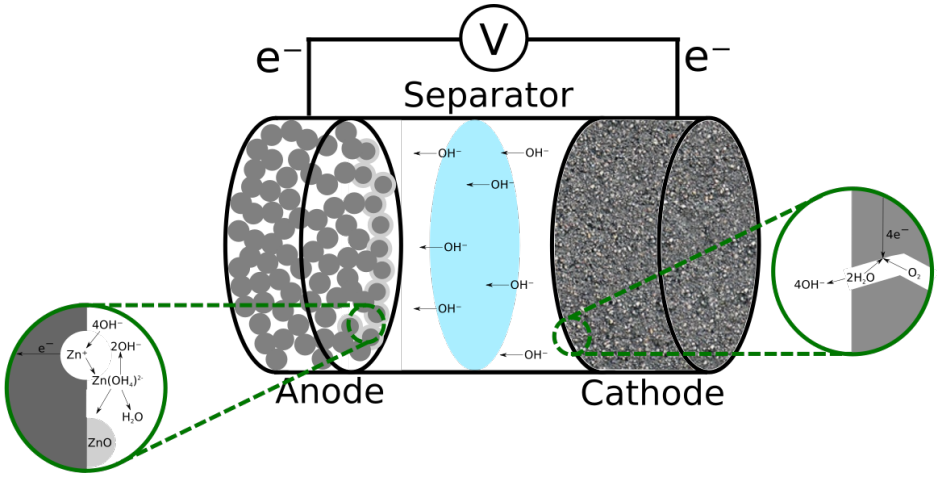

Figure 1.3: Schematic representation of an alkaline Zn-air battery with a porous Zn anode during discharge.

The first mention of a metal-air battery was the Zn-air cell, which was conceived in 1878 in a patent, and in 1933 a commercial product was patented in the United States [14]. They use an air electrode to reduce oxygen which can then be used to oxidise Zn. A schematic can be seen in 1.3. Since then Fe-, Al- and Mg-air batteries were proposed, and more recently non-aqueous variants such as Li-, Na- and K-air batteries were suggested. Each metal has its own benefits and challenges, but generally these chemistries all attain a very high energy densities as can be seen in figure 1.4 . The Al- and Mg-air batteries have very high theoretical energy densities, as seen in Figure 1.4, due to the relatively low weight of these metals and the fact that the number of electrons transferred is 2 and 3, respectively. The Li-O_2 battery has a capacity which is nearly comparable to gasoline's, and as such has attracted a lot of attention [15][16][17][18]. Even with the promising properties of these batteries, they are not readily available commercially.

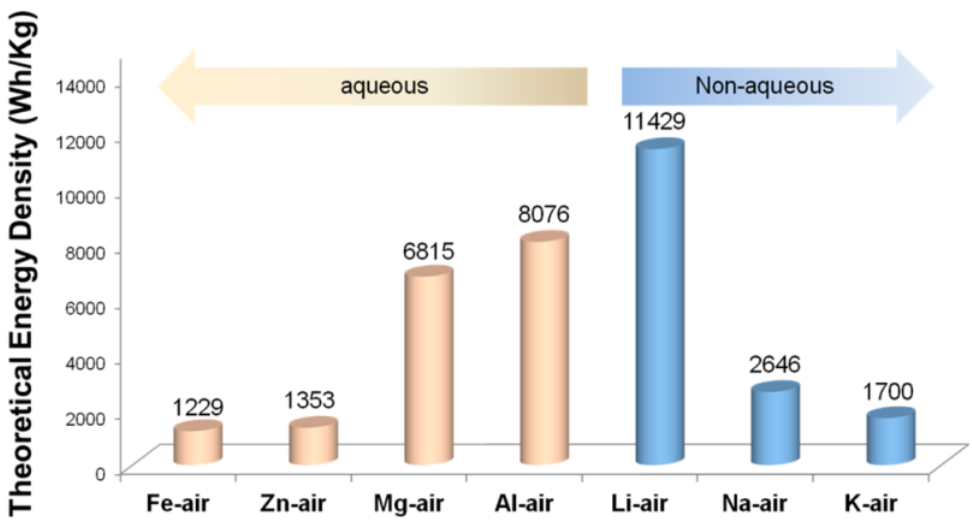

Figure 1.4: Specific energy of different metal-air batteries[19]

The zinc-air battery can be considered as one of the most successful metal-air batteries, as it has seen widespread application as a primary battery for hearing aids and other low-current devices. The Zn-material has a theoretical specific energy of 1086 Wh/kg including oxygen and 1358 Wh/kg for the pure material, which is almost 3 orders of magnitude higher than current lithium-ion batteries. Practical applications of Zn-air batteries report values between 350-500 Wh/kg [19][20]. Further-

more, Zn is very abundant, has a low cost of 2 USD/kg, compared to Li at 8 USD/kg (in 2010), and it can be fully recycled [21]. The theoretical discharge potential is 1.65 V, but practical values are lower due to overpotentials.

Thus far, electrical recharging of these batteries is a challenge that can be circumvented by mechanically replacing the anode or using a flow system, in which case it could be considered as a zinc-air fuel cell[22].

Principle of Zinc-Air Batteries

Zn-air batteries convert O_2 and Zn during discharge to create ZnO. During charge the ZnO is split up, oxygen is emitted from the battery and Zn is redeposited. This process requires the use of an air electrode that employs a catalyst to split O_2. The overall reaction is:

$$\mathrm{Zn} + \mathrm{O_2} \longrightarrow 2\,\mathrm{ZnO}$$

At the air electrode, the Oxygen Reduction Reaction (ORR) turns O_2 into OH^- on the surface of a wetted catalyst.

$$\mathrm{O_2} + 2\,\mathrm{H_2O} + 4\,\mathrm{e^-} \longleftrightarrow 4\,\mathrm{OH^-}$$

At the anode, the hydroxide is consumed when it reacts with Zn to create the soluble intermediate zincate and releases electrons to the circuit, leading to the overall reaction:

$$\mathrm{Zn} + 4\mathrm{OH^-} \longleftrightarrow [\mathrm{Zn(OH)_4}]^{2-} + 2\ \mathrm{e^-}$$

Since the electrolyte is constantly replenished, the zincate concentration will continue to increase until it reaches the solubility limit and ZnO precipitates.

$$\mathrm{Zn(OH)_4}^{2-} \longleftrightarrow \mathrm{ZnO} + \mathrm{H_2O} + 2\ \mathrm{OH^-}$$

However, in alkaline electrolytes the Zn anode corrodes, which forms Zn-hydroxide and forms hydrogen according to the reaction:

$$\mathrm{Zn} + 2\mathrm{H_2O} \longrightarrow \mathrm{Zn(OH)_2} + \mathrm{H_2}$$

This depletes the Zn-anode and the electrolyte during the battery's shelf-life. Another side-effect of the alkaline electrolyte is that K_2CO_3 (hydroxide is provided in the form of a an alkaline electrolyte. precipitates in the pores of the cathode due to hydroxide reacting with the CO_2 in the

air. Moreover the alkaline electrolyte can, redistribute Zncate through the electrolyte which can lead to deposition of ZnO outside the anode or cause dendrite formation.

1.4 Scope of This Thesis

Given the challenges and opportunities in Zn-air batteries and the pursuit of long cycle life, it is essential to develop and apply capable characterisation techniques. Through these techniques, it is possible to improve not only the fundamental materials, but also the the larger cell design.

For the materials that support the electrodes, it is essential that they are stable within the entire life of the battery. Some of the common choices are investigated here by developing in situ optical spectroscopy techniques to investigate dissolution of these. An Alkaline electrolyte was investigated for O_2 and H_2 evolution and compared to another alkaline electrolyte with additives. A pH 8 buffer stabilised $ZnCl_2$ and a neutral electrolyte where investigated using the same techniques. The mechanism for H_2-evolution and means to mitigate it is investigated, by doping the surface with In and Bi. Finally, the structure of a Zn/ZnO anode is investigated during cycling with the intent to visualise how Zn and ZnO is deposited within the battery.

Chapter 2

Characterisation Techniques

The chapter describes the methods and equipment used in this thesis.

2.1 Electrochemical Cells

2.1.1 The EL-Cell

For paper I and II the ECC-air Ni cell, commonly referred to as the EL-cell, was used. It is a hermetically sealed commercial 3-electrode cell with air in and outlets. In the present document it was only used in 2 electrode. The body of the cell is made out of PEEK in order to resist the alkaline environment of the electrolyte. The metal anode is contacted through the bottom of the cell through a Ni pin. The air cathode is contacted through a Ni spacer. The cell is connected to DEMS setup through metal tubes using quick connects. The cell is seen in figure 2.1 with the normal parts that goes into it in various stages.

2.1.2 DEMS-cell

A few measurements in this thesis employs the DEMS swagelok cell. This cell is developed by [23] [24] with the intention of mimicking the a system described By Macloskey et al. in [25]. The cell consist of number of swagelok parts, custom made steel parts and a glass tube. In this thesis it was used to perform DEMS measurements on the Highly Concentrated Zinc Electrolyte (HCZE) measurements as the other system in this thesis

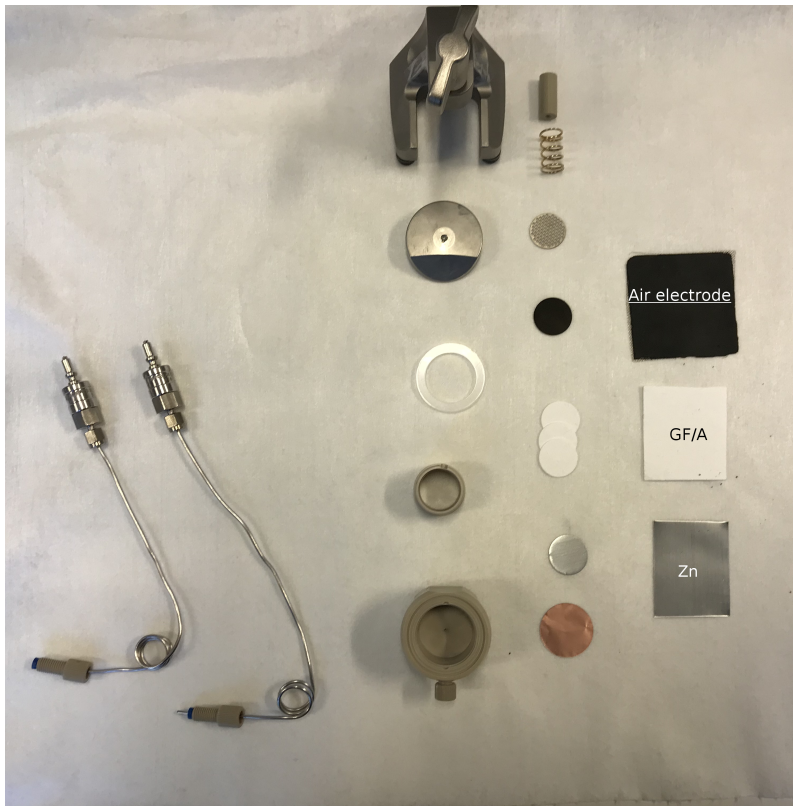

Figure 2.1: The ECC-air Ni test cell seen with the various components that go into assumbling a Zinc-air within this cell

would corrode the steel. Additionally the smaller headspace of this cell increases sensitivity of the DEMS measurements.

2.1.3 In-Situ Capillary Cell

This cell was designed for *in situ* synchrotron XRD experiment on Zn-air batteries. For these type of experiments it is important that information is obtained from the entire sample. Even with very hard radiation the interaction volume needs to be small when investigating metals due to their absorbency, which requires small cells. The cell is made from two sizes of borosilicate capillaries with external diameter of 3 and 2 mm and internal diameter of 2.4 and 1.6 mm respectively. The commonly used electrolyte in Zn-air batteries is highly concentrated KOH which is known to decompose glass, but this material was chosen because it is easy to work with and the general lifetime of these cell is short so that

it does not impact the chemistry significantly. The capillary cell consist of three prepared parts, the anode glass part, the electrolyte glass tube,, and the cathode glass part. These three parts the assembled result can bee seen in 2.2

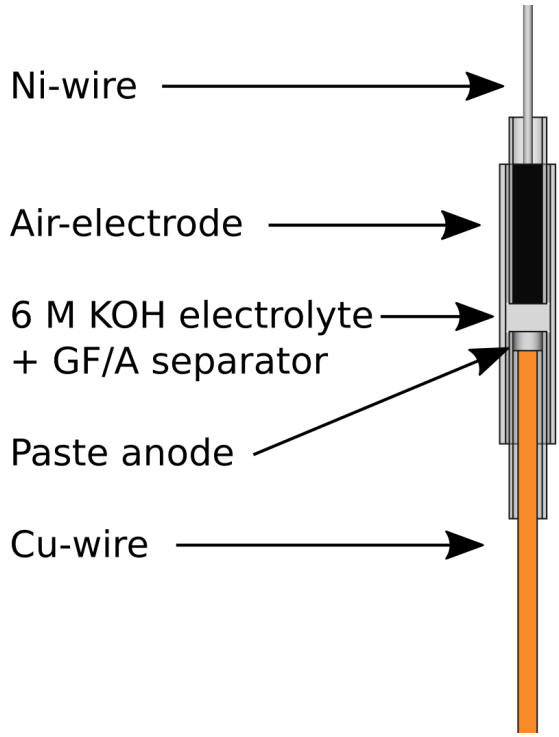

Figure 2.2: Schematic of the capillary cell

The anode assembly consist of a 1 mm wide Cu-wire with a polished end inserted into a roughly 2 cm long piece of the 2 mm OD capillary. The polished end will be the current collector and should be be a millimetre from the end of the tube. When the wire is in the correct position it is secured with UV glue. The glue is applied to bottom of the capillary and will be transport up into the glass tube by surface tension. By adding small amounts of glue at the time the height of the anode compartment can be controlled. The anode paste is applied to the top of the this part immediately before full assembly. The air electrode is made from a 2 cm long piece of the 2 mm OD capillary. The desired powders are mixed by mass and dispersed into a 300% wt solution of isopropanol. The slurry is transferred to the capillary and a 0.5 cm thick Ni wire is inserted into the slurry. The capillary is heated in an oven at 340 °C for 1 hour,

after which the Ni wire is secured in place and will act as the current collector. With these parts a full battery can now be prepared The paste anode is applied to the anode glass piece and is inserted into a 2 cm long piece of the 3 mm OD glass tube and secured in place using UV glue. Again the glue is applied by using surface tension, it is important that this glue seal is watertight. A 2 cm long 1 mm wide piece of Whatman GF/A glassfiber is applied to serve as a separator. It is advise to add the separator before the electrolyte. When the electrolyte is applied assemble the cathode parts is inserted into the wider tube with electrolyte and separator without bubble formation and secured in place via UV-glue. The cell can now be mounted and contacted through the bottom Cu and the Ni top wire.

2.1.4 Cathodes

Aside from the capillary cell air electrodes, all air electrode, such as the one seen in 2.1, were supplied by a partner in the the ZAS project, Alexander Niederstrasse from DLR. The cathodes mixture was made by dry mixing powders (catalyst, additives if any and binder) and subject it to hydraulic pressing on a Ni grid a 3 bar after which they were heated in to 340 °C for 1 h. For each experiment a piece from the supplied sheets were wrapped in paper and cut using an MTI disc cutter with the grid facing the piston. The resulting size for the cathodes would be to 18 mm for the EL-Cell and 10 mm for the Swagelok DEMS cell. Each 18 mm anode would weigh between 500 and 560 mg and would only be used once. No relation between OCV and air electrode mass was found. Each cathode represented herein is only used once.

2.2 Characterisation methods

2.2.1 Galvanostatic Discharge and Charge

A simple and intuitive measurement to investigate is galvanostatic discharge and charge. By employing voltage or time limits to these measurement provides an easy means to control or determine capacity. It is also an easy means to measure degradation as capacity loss or overpotentials. Discharge and charge is determined by the current between the electrode.

2.2.2 Cyclic Voltametry

Cyclic Voltametry is 3-electrode technique where an applied potential is imposed onto a system while measuring the resulting current. The imposed potential is swept, at a constant sweep rate between the two potentials, called vertex potentials. When the vertex potential is reached the potential is swept back again resulting in a saw tooth pattern for the potential. The direction of the potential sweep is an import parameter when interpreting a CV, going towards high potentials is labelled as the *anodic* direction and the response here indicates oxidation of the working electrode. Sweeping towards lower potentials, *cathodic*, is associated with reduction of the working electrode[26]. A the voltage profile and a typical CV of Zn can be seen in figure 2.3. As mentioned Each peak is associated

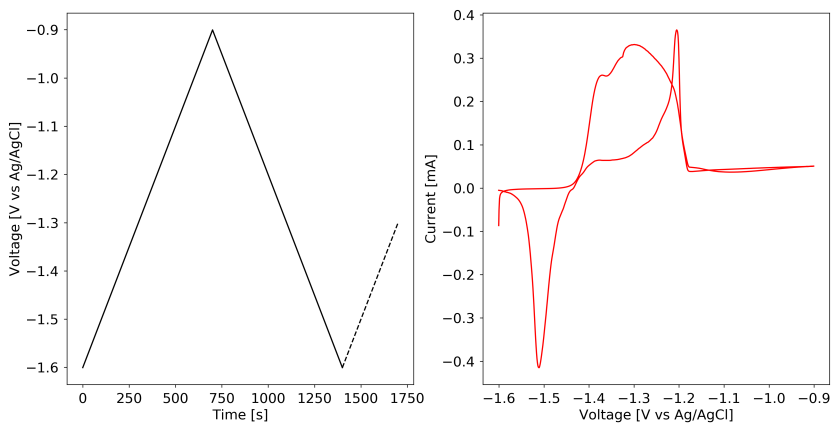

Figure 2.3: a) the voltage profile in a cyclic voltametry experiment. b) A cyclic voltamogram of Zn.

with an electrochemical process on the working electrode, in this case the anodic direction involves oxidation and dissolution of Zn while during the cathodic scan it is deposited. The sweep rate of scan affects the size of the peaks and can be related to electrochemical proprieties if parameters are properly controlled.

2.3 Inductively Coupled Plasma - Optical Emission Spectroscopy

Inductively Coupled Plasma and Optical Emission Spectroscopy is technique that can identify metallic compounds in liquids in very low concentrations. The liquid is vaporised in a nozzle with a high flow of argon. The vapour is transferred into an RF coil where it is heated to 10 000 K using electromagnetic fields. The hot plasma produces radiation which can then be used to identify the compounds within stream by their emisson lines. The concentration of the compounds can be quantified by the use of calibration solutions with a well defined content of these materials.

2.4 Differential Electrochemial Mass Spectrometry

Differential Electrochemical Mass Spectrometry (DEMS) is a measurement technique that can quantitatively characterise the emission of evolved gaseous species in an electrochemical device. The method can be dated back to Bruckenstien *et. al.* [27], but the term DEMS originates from Wolter *et. al.* in 1984 [28]. Since then several variations and modification have been made to these setups but the one used in the present document can be traced to McCloskey *et. al.* who refined the method to investigate Li-O_2 batteries[25]. This version of the technique is specialised for full electrohcemical cells that employ electrolytes with high vapour pressures where evaporation is critical and as such it uses a six-way rotation valve. The particular setup was developed by Jonathan Højberg for use to investigate Li-O_2[23].

This setup has two operation modes, one that measures pressure change during cycling, and one that employs the MS. The latter mode flushes the evolved gasses in the head space of cell with Ar into the volume of V_{MS} and its content is then lead to the MS for analysis. The valve movement and the the Ar affects the pressure in the setup so that getting electron numbers is not possible, therefore to get both electron numbers and MS data two identical experiments have to be conducted. MS data is only possible to obtain during OCV and charge, even when flusing with oxygen as the discharge potential is related to O_2 partial pressure.

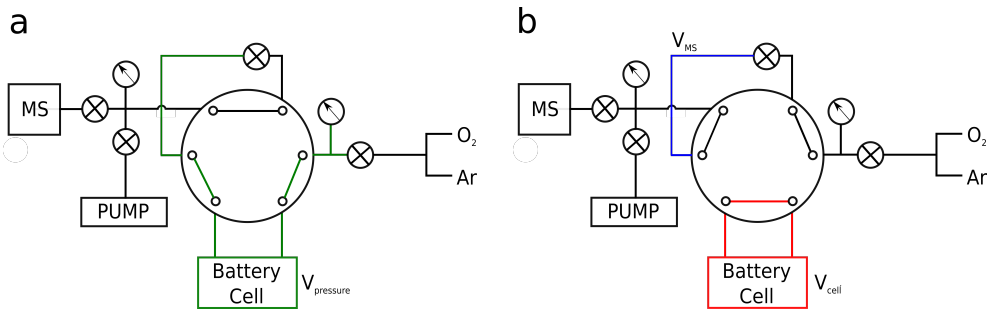

Figure 2.4: Schematic of the Differential Electrochemical Mass Spectrometry setup a) The open position that would be used for determining electron numbers in discharge and charge configuration, and the calibrated volume $V_{pressure}$ (green) b) The closed position that is used when the MS is being used and the calibrated volume V_{MS} (blue) and V_{cell} (red).

2.4.1 Number of Electron per Oxygen Molecule e^-/O_2

A staple of electrochemistry is reporting the columbic efficiency, but this property often relies on the assumption that none of the electron passed in the cell is being used to degrade its components. Verifying this assumption requires the electrochemical cell to be contained in a hermetically sealed enclosure while cycling in which the pressure can be measured. The number of electrons per O_2,$n_{\Delta e^-/O_2}$, can be calculated using 2.1 which relates the pressure change to the number of electrons passed through the cell.

$$n_{\Delta e^-/O_2} = \frac{\Delta Q R T}{\Delta P V_{cell} F} \tag{2.1}$$

Where ΔQ is the passed charge, R is the ideal gas constant, T is the temperature in Kelvin, ΔP is the pressure change, V_{cell} is the volume of the employed cell and F is Faradays constant. This simple measure is an effective means to verify columbic efficiency. While it is possible to calculate this value by inserting the relevant parameters it is recommended to apply an approach where a calculated pressure curve is calculated an inserted and matched to the measured pressure curve using the calculations:

$$\Delta P = \frac{n_{O_2} R T}{V} \tag{2.2}$$

$$n_{O_2} = \frac{It}{n_{\Delta e^-/O_2} F} \tag{2.3}$$

Where ΔP is the resulting pressure, which is a function of the number moles O_2, n_{O_2}, developed or consumed in running a current through the cell, T is the temperature, V is the Volume of the cell and tubing, I is the current, t is the length of the experiment, F is Faradays constant and $n_{\Delta e^-/O_2}$ the variable that is controlled to adjust the fit. By using this approach, different regimes of of the pressure curve can be fitted individually. The mass spectrometer requires purging of the cell and as such when it is employed measuring electron numbers is not possible. Qaudropole Mass Spectrometers, QMS, measures the amount of ionised gas that reaches the filament for a given *mass-to-charge ratio* - m/z, which is unitless. In this document m/z values are converted and referred to the chemical equivalent, *e.g.* CO_2 would correspond to the m/z= 44. This implies calibration of the sensitivity of the MS using reference gasses with known amounts of each constituent and investigation that there are no overlapping m/z for evolved gasses. Given a m/z value that is not covered by the calibration gasses the sensitivity parameters for the closest neighbour with a known sensitivityapplied. As an example m/z = 31 would be converted through the use of the m/z = 32, which is using an O_2 calibration gas.

2.5 X-Ray Diffraction

X-rays provide a convenient means of investigating materials as they provide the ability to probe very small structures. X-rays can largely be considered to be non destructive depending on your sample. The wavelength of X-rays often in the order 1×10^{-10} m, which is comparable to the inter atomic distances in most crystal lattices. Crystal lattices are made from a large array of well ordered atoms. The structures are described by a unit cell, which is the smallest structure that can describe the larger array in all directions. This unit will contain six parameters, the length of its axes (a,b,c) and the angles between these (α,β,γ). By considering this unit cell in all directions it is possible to identify planes in the lattice along each axis, which can be described in 3 dimensional space by Miller indecencies *hkl* and a characterised by a lattice constant.

Using a monochromatic beam, X-rays can be elastically scattered on such an lattice plane. The scattered beam interacts with itself and produce

strong *reflections* where constructive interference conditions is fulfilled. Braggs law can be used to calculate at which angles θ constructive interference is obtained:

$$n\lambda = 2d\sin\theta \tag{2.4}$$

Where d is the lattice constant, n is a positive integer that describes the order, and λ is wavelength the incident X-rays.

2.5.1 Synchrotron X-ray Radition

Synchrotrons are large facilities where electrons are accelerated to high speeds in an evacuated ring. By altering the path of the electron through magnetic field created by devices such as wigglers or undulators X-ray radiation is created. Through this method the wavelength of the X-ray radiation can be tuned, with higher intensity and resolution than in-house sources. Using these beamlines it is possible to perform very fast measurements on battery materials.

2.6 X-Ray Tomography

Tomography refers to imagining a subject by a penetrating nondestructive waves, in this case X-rays. The technique requires obtaining several transmission images of the sample while the samples is being rotated in small increments between each image. By correlating the these images and the angles they were obtained at, the geometry and structure of the sample can be recreated. When the reconstruction is obtained it can be cut and or segmented so that different phases of can be identified and quantified or simply to create images of the a cross section in the sample. Performing these measurements requires small samples, high intensity, relatively hard X-rays or long exposure times to ensure a statistical significant signal which determines the resolution.

Chapter 3

Anode Current Collectors

In the transitioning from primary to secondary Zn-air batteries each cell will be expected to operate for hundreds of cycles [29]. Which creates high demands for the active battery components but also current collectors, separators and contact pins. As these have to withstand the cycling and the electrolyte environment throughout the cells lifetime. The commonly applied electrolyte KOH restrict the choices of materials significantly, common materials such as steel, carbon and glass corrode in this electrolyte. In this chapter the focus is on developing a method for correlating electrochemistry with degradation effects, and using it on a subset of current collector materials. That means employing cyclic voltametry could with ICP-OES analysis of the resulting products, which means developing af cell where electrolyte can be reliably extracted and analysed in real time.

An important part of the battery is the anode current collector, it will have to support the anode throughout the cells life and will have to retain its shape, and conductive properties while not interfering detrimentally in the battery. A secondary Zn air battery has potential window of 2 V in aqueous solution which also means that gassing can occur.

A variety of materials have been suggested for Zn-air batteries but Cu or Sn are commonly applied [30][31]. Other materials such Ni, Ti, W and stainless steel have also been proposed for various purposes [32][33][34][35][36].

3.1 Experimental Details

In Figure 3.1, the potential window for a for a Zn-air battery is seen using a Pt wire as an air electrode. The CV of Zn is in decent agreement with what was found by [37]. Zn dissolves as Zn_2^+ until the potential reaches 1.1 V vs Ag/AgCl where a film is created that blocks dissolution, the current after this peak is associated with current passing through this film. Zn starts dissolving again once the during the cathodic scan once the potential is low enough for the film disappear. This continues until the Zn is redeposited. The Pt CV has a clear O_2 evolution peak above 0.5 V vs Ag/AgCl and ORR 0.3 V vs Ag/AgCl.

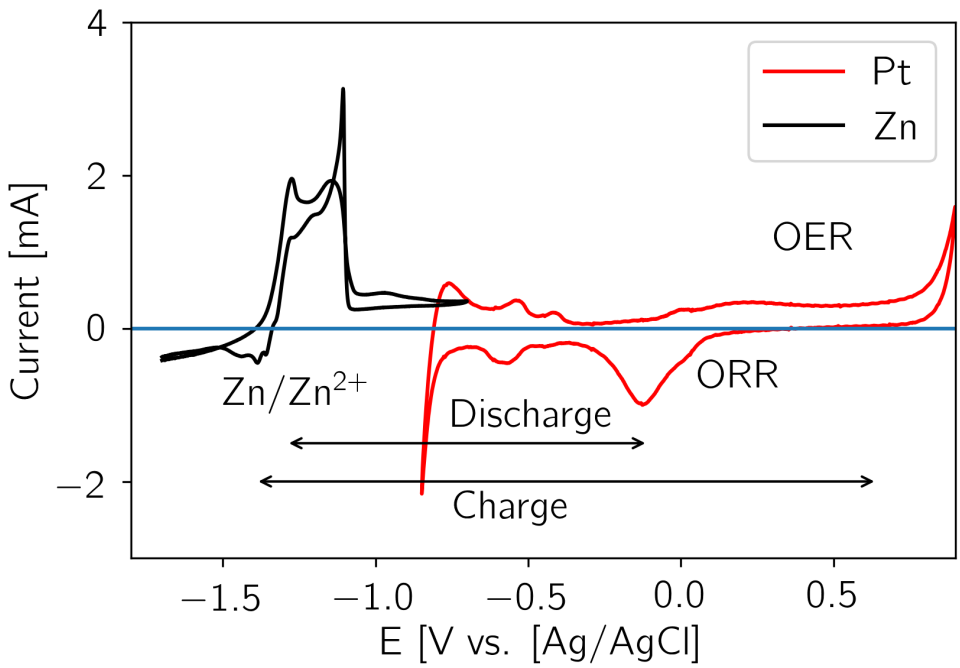

Figure 3.1: The potential ranges of Zn dissolution/deposition (Black) with O_2 ORR and OER on Pt. surface in the flow cell.

Knowing where the relevant peaks potential are it is now possible to investigate other materials. T figure 3.3

To avoid cycling these batteries several hundred cycles, Cyclic Voltametry, CV, was applied to test the materials Cu, Sn, W, SS and Ni and Ti. The materials were all more than 99.5 % except Sn which was 95 % pure with the remainder consisting primarily of Ca.

3.2 The Flow cell

The flow cell used in these experiments is seen in figure 3.2 and is inspired by the design of Ogle *et. al.* who has employed a similar cell to investigate Cu film on stainless steel and the effect of adsorbed H_2 on the dissolution of steel[38][39]. It was constructed in acrylate in three parts that when connected would form a compartment as seen in figure 3.2. The diameter of the working electrode area is 1 cm and the inlet and outlet channels are 1 mm wide. The electrolyte was pulled into flow cell in by peristaltic pump that would also pull the liquid into the ICP-OES for analysis. The flowrate at 30 RPM was determined to 3 mL/min . The piping 1/8 inch polyethylene tubes. The working electrode is separated by from the reference and counter electrode by a permeable membrane made from Cellgard 3401. The purpose of this membrane is simply to provide flow resistance and to confine the flow to the surface of the working electrode. The electrolyte would be emptied between experiment to remove residual material in the tube and in the chamber of the cell. The reference electrode was a leak free LF-1.6-45 Ag/AgCl 1.6mm wide from Innovative Instruments and the counter electrode was Pt/Ir wire. The N2 purged 1 M KOH electrolyte was moved using a peristaltic pump and PE tubing.

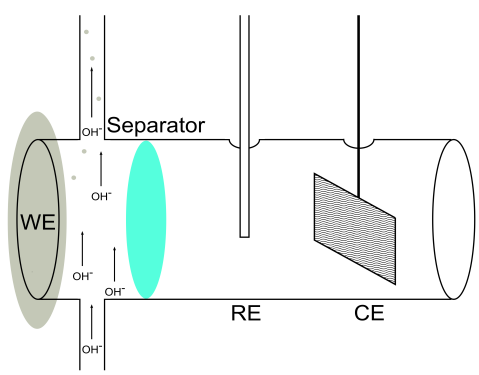

Figure 3.2: A schematic of the developed flow cell used for combined CV and ICP-OES experiments.

3.3 Cyclic Voltametry Results

Before the metal sheets are tested in the flow cell they are tested offline in regular 3-elctrode CV experiments. In Figure 3.3 the CV for all the materials is seen.

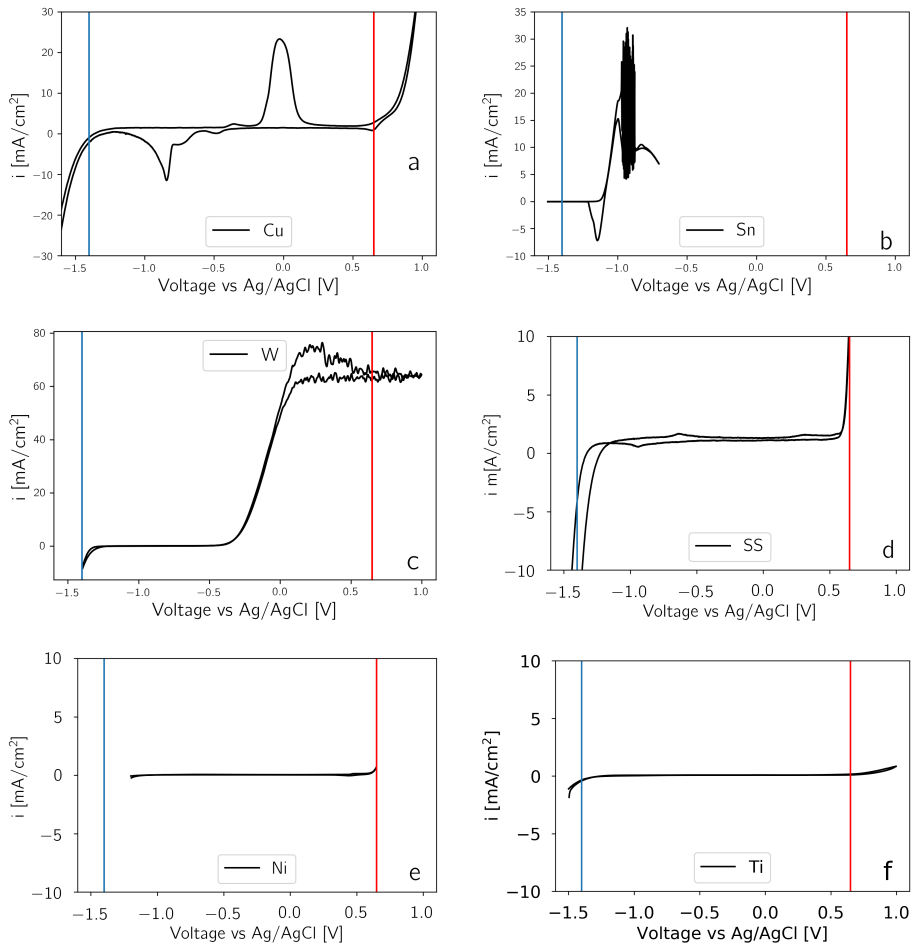

Figure 3.3: CVs of a) Cu, b) Sn, c) W, d) SS, e) Ni alloy and f) Ti Alloy in 1 M KOH at 10 10 mV/s, except Sn which is at 1 mVs with the potential of Zn (blue dashed line) and onset of the O_2 reduction red dashed line.

The Cu CV is in agreement with what is found in literature [40] [41] with the Cu(O) to Cu(I) and the further oxidation to Cu(II). At the vertex potential there is heavy gas evolution which would make it unsuitable for a cathode in case it would come into contact with the electrolyte.

On cathodic scan the reduction of Cu(II) to Cu(I) and later Cu(I) to Cu(0) are clearly visible before hydrogen evolution starts, which slightly overlaps with the Zn deposition potential.

W exhibits significant oxidation above $-0.5\,\mathrm{V}$ vs. Ag/AgCl where it ultimately dissolves into WO_4^{2-}. until it reaches a plateau which is slightly noise due to the surface changing quickly.[42] [43]

Sn which is a common current collector oxidises and dissolves through Sn(II) to Sn(IV) at $1.1\,\mathrm{V}$ vs. Ag/AgCl until a passivisation film is formed and the current goes down until the vertex potential. The static above $-1\,\mathrm{V}$ vs. Ag/AgCl is due to the very high current which makes it difficult for the potentiostat to measure the voltage. The static subsides at more positive potentials due to passivisation of the Sn surface. is On the cathodic scan the Sn foil exhibits a reduction peak at $1.15\,\mathrm{V vs Ag/AgCl}$ and exhibits no gas evolution at the lower vertex potential.[44]

Stainless steel can immediately be disqualified for the anode current collector since there is significant gas evolution already from the initial vertex potential. After which there are few small peaks on the way to the second positive vertex potential which could dissolution of Chromium or other chemical in the steel. At the positive vertex potential there is again significant gas evolution which also disqualifies for the cathode. On the back scan there is a single cathodic reduction peak imitate before the gas evolution commences.

The Ni CV is started higher than the others as it already exhibits significant gas evolution already at $-1\,\mathrm{V vs Ag/AgCl}$. Scanning more anodic the CV is completely until a slight oxidation of $Ni(OH)_2$ to NiOOH at $0.5\,\mathrm{V vs Ag/AgCl}$[45]. Which with is followed by significant gas evolution, which is expected as Ni is a known OER catalyst.

Ti is very stable and has no reduction or oxidation peaks within the two vertex potentials an exhibits only slight gas evolution beyond the potential of Zn deposition and O_2 evolution.

3.3.1 ICP-Correction

From the cyclic voltamograms it is possible to understand at what potentials processes occur on the surface on the metals. Some reaction like oxidation of Cu(O) to Cu(1) is not associated dissolution while oxidation

of the Cu(I) to Cu(II) is. Using the flow cell these the exact rate at which the dissolution occurs. The distance between the working electrode compartment and the ICP detection chamber is kept as small as possible, the tubing will delay the signal. Additionally the ICP response will experience broadened due to mixing and resistance in the tube. Therefore CV and ICP signals have to be aligned. This is done through a series of current steps and measuring the ICP response signal. Using a stop watch the delay was determined to be 10.78 s. From figure 3.4 it is seen that the ICP further correction is needed as there is a between the time signals. The delay was determined to be 30 s while the time of set was 0.93 at 30 RPM. For each current step, the ICP signal peaks after 24 seconds and is almost entirely gone by the next current step.

3.3.2 ICP-OES results

Ni and Ti are not tested in the flow due to their early onset of HER and flat voltage profile respectively. The other material Cu, Sn, W and SS were investigated in the flow cell under a flow of 3 mL/min and a scan rate of 1 mVs on fresh metal foils. The vertex potential where chosen to span the full potential window of the Zn-air battery. Except for materials that had gas significant gas evolution within this window, to avoid damage to torch and vaporisation source in the ICP-OES.

In figure 3.5 the CV voltamograms for Cu, Sn, W and SS are plotted over time to avoid confusion between anodic and cathode current. For Ni and Ti no species were detected despite being exposed to multiple long cycles.

In the ICP-OES, the Cu 324 emission peak can be collrected to peaks are in the anodic scan of the CV. Scanning anodically there is no significant dissolution until the Cu(I) and Cu(II) and after more than 2000 s of scanning anodically there is a significant dissolution peak but this is is related to the O_2 evolution from the Cu anode. The O_2 bubbles in mixes the solution better and empties any dead volume in valves and bends that contain Cu. On the cathodic no dissolution can occur although there is the presence of a reduction peak after 3800 s indicating that there is Cu available for deposition. This indicates that the interaction volume with the working electrode is to large as it can hold Cu-ions, or that there static volumes along the flow. When are not detected in the ICP this indicates that at the flow is not flushing the flow cell and tube volume

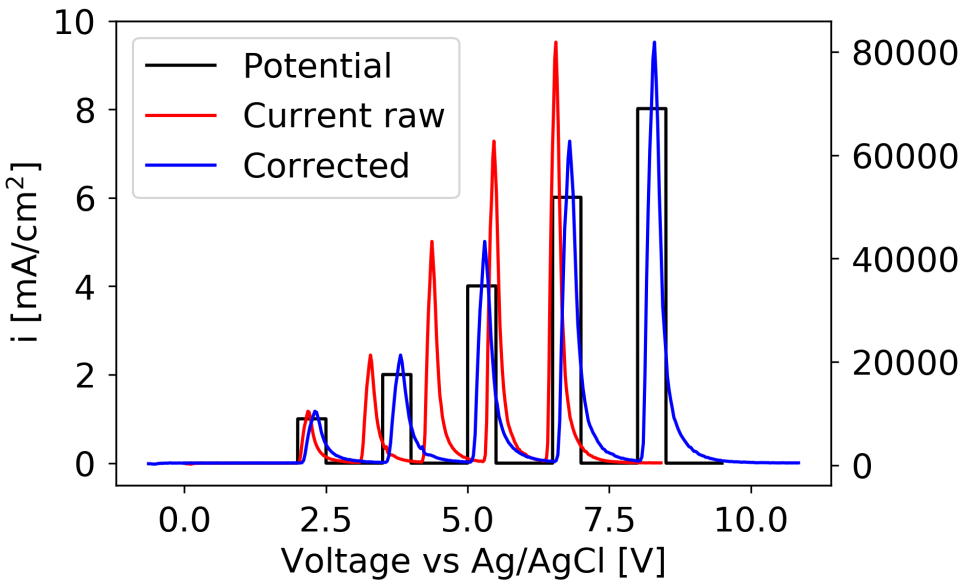

Figure 3.4: Current steps at 1 mA/cm^2,2 mA/cm^2,4 mA/cm^2,6 mA/cm^2 and 8 mA/cm^2 and the ICP Zn 206 nm emission peak with and with time corrected.

correctly or that the Reynolds number is to high which allows for stable pockets electrolyte.

The Sn dissolution after less than 500 s with strong dissolution current in the CV and high signal of 125 ppm as seen in the Sn 189.9 nm emission line. Despite the static that occurs in the CV the Sn signal is high until after 620 S where the passivisation film occurs and the current and Sn signal decrease until the vertex potential where after the potential increases again. As with Cu there is a clearly visible reduction peak of Sn on the cathodic scan, and the concentration of Sn ion in the chamber can be detected in the ICP, likely because the concentration is much higher. After this peak however there are no discernible features meaning that H_2-evolution is suppressed on Sn compared to Cu.

The W signal is the highest in all of the investigated materials, at more 250 ppm the peak oxidation of W starts −0.4 V vs Ag/AgCl and levels. On the anodic scan the current saturates briefly as the cell hits the is cell voltage limit but the dissolution continues to increase, likely due to

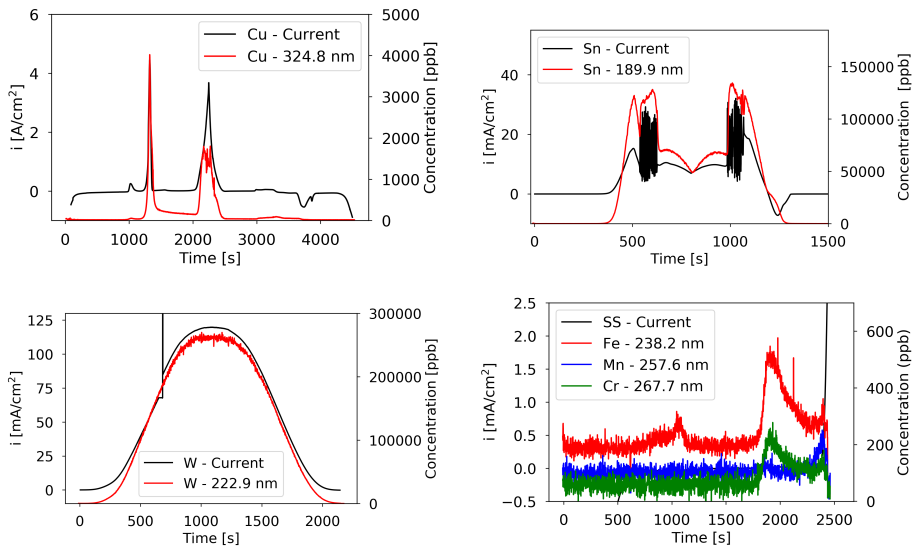

Figure 3.5: CVs of a) Cu, b) Sn, c) W, d) SS, in 1 M KOH at 10 11 mV/s with the potential of Zn (blue dashed line) and onset of the O_2 reduction red dashed line.

delay in the signal. Tungsten dissolves quite far from the conditions of the current collector and exhibits only slight hydrogen evolution as those potentials also making it a potential.

The stainless steel signal is very low but dissolution is detected. The strongest signal is Fe has two distinct peaks after a 1000 s of anodic scan this dissolution cannot be tied to feature in the voltamogram. Both the Fe and the alloying constituent Cr dissolve at the peak located beyond 0.0 VvsAg/AgCl. When the hydrogen dissolution starts at 0.5 VvsAg/AgCl. No backscan was performed because the signals are too low and the irreversible nature of dissolving steel.

While Sn is superior in terms of hydrogen evolution the material dissolves quickly and close to the potential of the Zn electrode. Tungsten would perform well in terms of chemical resistance in the anode but still exhibit hydrogen evolution. Of the materials investigated here only SS and Ni is disqualified for the anode while Cu, Sn and W would not be suitable for the cathode. Ni, a well established current collector was confirmed to do well as it experience little dissolution around the OER evolution potential and is also here seen to have significant OER activity. These conclusion are made only in relation to their dissolution, and there other aspects to

account for such as conductivity and price. This line of experiments has confirmed that the produced flow cell is working and that it can be used to investigate current collectors for Zn-air batteries. It would be ideal to improve the cell design by reducing the interaction area and volume of the cell to avoid high currents and difficulty controlling the potential. Another modification would be to improve the flow over the working electrode to become more laminar, this could be achieved by tapering the inlet and outlet or perhaps adopt a geometry similar to Schuppert *et. al.* [46].

3.4 Summary of Anode Current Collector Investigation

Through the development of the a flow cell combined with ICP-OES the dissolution of Zn and stability of Cu, Sn, Stainless steel, W, Ni alloy, and Ti alloy in alkaline solutions were investigated. The emission peaks could be correlated to the CV data by calibrating the ICP-OES for time and concentration. The CV for each material exhibited CV similar to what is found in literature apart from static and artefacts related to difficulties in controlling current or voltage. Which was suggest could be remedied by lowering the active area of the cell and applying a new geometry. Further work would also include investigating air-electrodes.

Off these materials stainless steel were unsuitable for both the anode and cathode current collector as it exhibits a strong gas evolution at both the anode and cathode, but no chromium or other metal were detected with the ICP-OES. From these it was found that Ni and Ti could be suitable for cathode current collectors, and in the case of Ti also the anode. In agreement with literature Cu and Sn are quite well suited for Zn-air battery anodes. W would be suited for anode current collector also.

Chapter 4

DEMS investigation of Zn-air batteries

The first section in this chapter covers Paper III with some additional results. The electrolyte of choice for Zn-air batteries is highly concentrated KOH, various values are reported but generally molarities higher than 5 M are found. It provides high conductivity, high oxygen diffusion coefficients and with the high concentration the vapour pressure of H_2O is reduced which is good for open systems as it reduces the requirement for water management[47]. However, the KOH does present challenges, such as reaction with CO_2 in their air, self corrosion and the tendency to create dendrites. Quite a few other electrolytes have been proposed over the years with various advantages challenges.

4.1 Alkaline Zn-air battery with 6 M KOH electrolyte

A constant challenge when dealing with highly alkaline electrolytes is self corrosion. This process is occurring whether the battery is in storage or in use. For small disposable batteries the amount of hydrogen is can be overlook but in larger system such as power storage the problem has to be accounted for as it depletes both Zn surface and the electrolyte. Additionally when characterising Zn-air batteries the experiment is constantly affected by this conversion. The self corrosion can of a material is easily determined by collecting the evolved gasses a Zn sample in an

electrolyte container. For full cells the however, the surface is constantly changing and the gassing will be affected by this. There are means to migitate self corrosion as will be demonstrated later but as long as it is no zero it is important to understand how to investigate and correct for it. To this end Zn-air batteries where assembled in the EL-cell with a 18 mm diameter 0.125 mm Zn foil anode, supported on Cu was tested in 6 M KOH against a$NiCo_2O_4$ cathode.

In figure 4.1 the electrochemical cycling data and measured pressures for such a Zn-air battery is seen. During the initial 1 h of OCV the pressure increases by 0.004 bar and the OCV which initially increases, peaks after about 20 min and decreases again to its original value just before the discharge starts. The initial increase is believed to be related to the wetting of the cathode while the decrease is related to self-corrosion of the surface. The operating pressure of the DEMS, in this case, 1.85 bar of pure oxygen is likely responsible for the increase. During discharge the voltage is flat at more 1.3 V while pressure decreases linearly. On charge there is a small bump in the charging profile before it flattens out and in this time the pressure is static, this bump appears at 1.8 V and is an oxidation of the air electrode because the high OCV will persist if reused in a new battery, although it decreases slightly over time. It is noted that until the voltage reaches ∼1.95 V the pressure does not increase. By measuring the pressure during discharge and applying equation 2.1 electron numbers can be obtained. During discharge the measured electron number is 4.53 on discharge and 3.61 on charge which is quite far from the ideal 4.00. This is indicative of difficulty of making bi-functional air electrodes, but also resembles that H_2 evolution is occurring. However, since the pressure sensors cannot distinguish between O_2 and H_2 and a significant portion will drive the numbers away from the ideal. Assuming that the rate discovered in the OCV measurement is constant this amount can subtracted from the pressure and yield ratios of 4.24 and 3.81 for discharge and charge respectively, much closer the ideal 4 that is expected for the OER. The electron number for the charge takes into account that some of the electron spent on some oxidation process in the cathode, as these do not contribute to gas evolution. The battery was cycled for at total of 3 times total and the adjusted discharge and charge values are 4.32 and 3.68 in the second cycle and 4.5 and 3.82 for the third cycle. It could be argued that the H_2 evolution is not constant, the Zn surface will passivate during OCV leading to reduced available active area, during discharge the surface will dissolve and redepositing

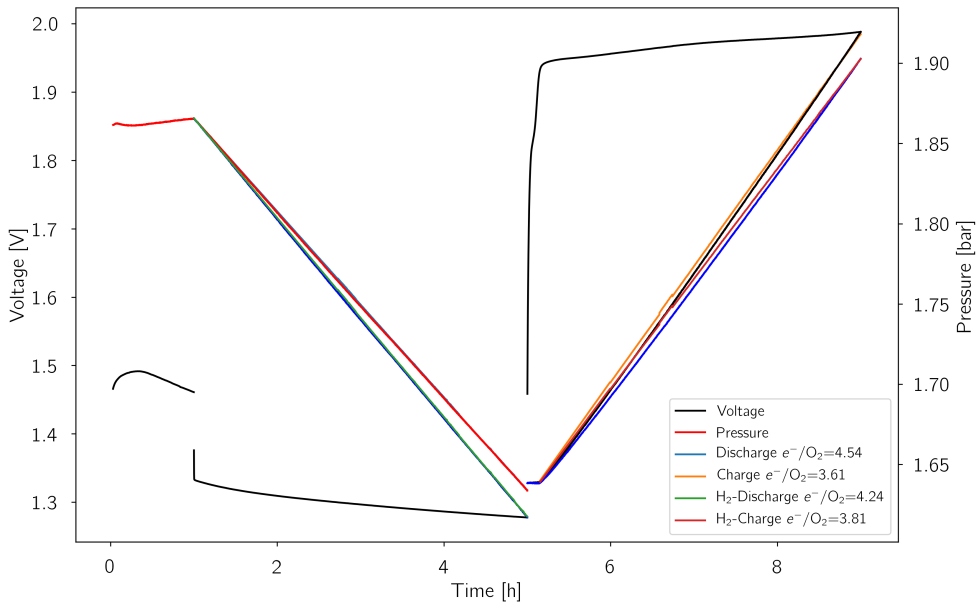

Figure 4.1: Electrochemical cycling and corresponding pressure data for a Zn-air at 1 mA/cm^2 with the electron number fit-lines with and without correction for H_2-evolution.

during charge leading to a different surface-area. This assumption can be tested by applying the mass spectrometer during OCV and Charge, the working principle of the sampling mechanism makes it difficult to get meaning signals during discharge. However, looking at figure 4.2 the gas evolution is seen during a similar battery during 3 charges.

It is seen that the H_2 signal starts to increase during the flushing period until it reaches 2.5 µmol/h after which it continues to increase and ends at 5 µmol/h. The average production in this time is 3.4 µmol/h which corrosponds to pressure increase in the EL-cell by 0.026 bar, 650% higher than in the pressure by itself. In the following cycles the H_2 signal what is measured in the first cycle. The O_2 signal in the final hour of the charge is 22.5 µmol/h, 20.9 µmol/h and 19.23 µmol/h and since the battery is cycled at 2.545 mA given a ideal 4 electron process should yield 23.7 µmol/h which yields electron numbers of 4.21, 4.53 and 4.93 respectively. A significant difference from the H_2 pressure measurements. This indicates that there is significant H_2 evolution, and therefore pressure cannot be employed itself. All of the e-numbers are summarised in Table 4.1.

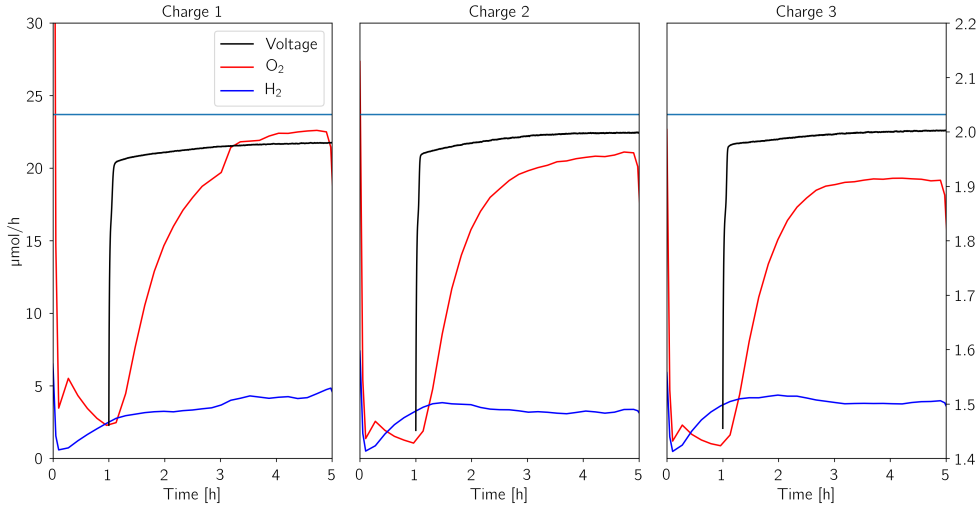

Figure 4.2: MS signals for H_2,O_2, during the first and second charge of a Zn-air battery with a 6 M KOH. The blue horizontal lines indicates a the expected O_2 signal for a 4 electron process.

Even with the H_2 evolution correction attributing these discrepancies from the ideal 4 is beyond the DEMS technique by itself but is indicative of a deficit of gas consumption and evolution. These experiment are performed at constant capacity and requires investigation by Electrochemical Impedance Spectrocopy, EIS, CV and other in-situ techniques.

	Discharge	Charge	H_2-Corrected Discharge	H_2-Corrected Charge	MS-Charge
Cycle 1	4.54	3.61	4.24	3.81	4.21
Cycle 2	4.79	3.50	4.49	3.68	4.53
Cycle 3	4.83	3.49	4.50	3.83	4.93

Table 4.1: The e^-/O_2 numbers for a Zn-air battery with and without H_2-correction and finally the e^-/O_2 as determined by the MS

Correction for H_2-evolution is necessary as it significantly impacts the e^-/O_2. In the case of the 6 M KOH the correction reveals that the e^-/O_2 are still at least 0.21 away from the ideal numbers. Over time, even with the H_2 correction it is revealed that the battery deteriorates over time, especially during discharge. For the MS derived electron numbers it is

obvious that the H_2 evolution is important to correct for as the pressure assumption is not sufficient the longer an experiment goes on.

4.2 Additives to KOH

As alkaline electrolytes have been widely applied there have been a series of investigation where adding various additives to KOH such as ZnO, KF and K_2CO_3 has been investigated in literature. As is investigated later in this document, adding the discharge product ZnO to the electrolyte is beneficial as it reduces Zn-dissolution and minimises migration of $Zn(OH)_4{}^{2-}$ and this way create more uniform deposition of ZnO [48]. Adding K_2CO_3 to an alkaline electrolyte in concentrations as high as $\sim$ 30 mol% does enables higher DoD due because it reduces the electrolytes reaction with CO_2 in the air [49][50]. Adler *et. al.* confirmed that KF benefited the battery cell overall by retarding the appearance of dendrites even though it impacts and others have suggested that this additive also benefited the overpotenial of ORR and OER on a $\alpha-MnO_2$ [51] [52]. Mainar *et. al.* investigated mixtures of these additives and found an optimal formulation for a full Zn air battery. A cell with this 7 M KOH + 1.4 M KF + 1.4 M K_2CO_3 electrolyte was made with Zn foil supported on Cu and a NCO air electrode with a Ni current collector. Since the setup test the cell in pure O_2 the additive K_2CO_3 is only relevant in the brief time the cell is assembled until the experiment start where the cell is purged. The discharge potential is 1.275 V and declines during slightly during the 4 h long discharge and the pressure drops 0.25 bar which yeilds a e^-/O_2 number of 4.15 close to the ideal 4. The shoulder in the charging is similar to reference battery which is related to the cathode materials and in the time it takes to overcome it there is no pressure increase. As the charging potential reaches 1.9 V the pressure starts to increase with a e^-/O_2 of 4.20. Accounting for the hydrogen evolution during OCV these numbers change to 3.99 and 4.35 which is very ideal for discharge but worse for charge. To understand these numbers further we can employ the MS during charge and in figure 4.4 where it is seen that H_2 signal never exceeds 5 µmol/h which is very low for a Zn foil. The O_2 signal is $\sim$ 23.3 µmol/h and 23.7 µmol/h in the second charge. The voltage profile during charge exhibits small dips every 10 minutes which corresponds to the timing of the Ar purge that leads the produces gasses to mass spectrometer. It is noticeable that the charging shoulder is wider in the first cycle than in the second. Using the MS we arrive at electron numbers

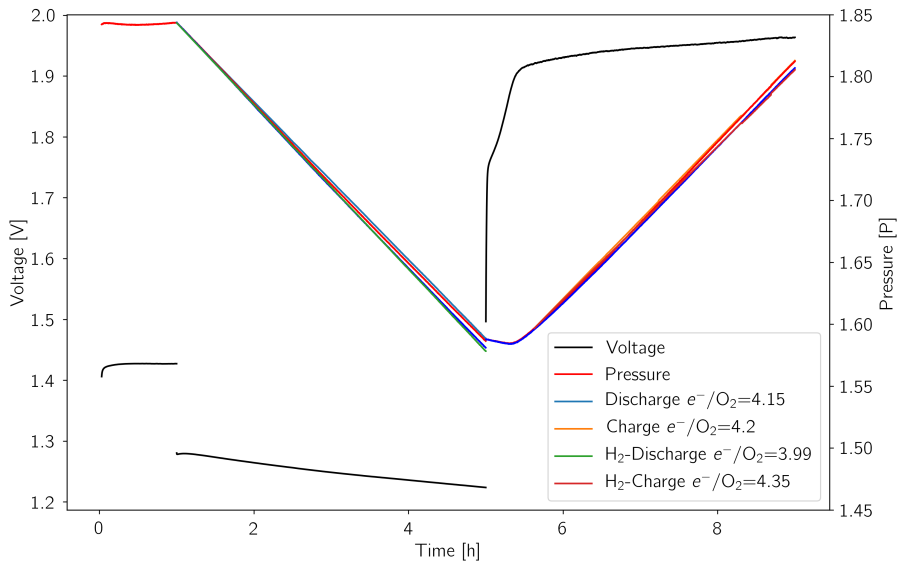

Figure 4.3: Electrochemical cycling and corresponding pressure data for a Zn-air at 1 mA/cm^2 with the electron number fit-lines with and without correction for H_2-evolution

4.07 and 3.98 discharge and charge respectively. All the numbers are collected in Table 4.2.

	Discharge	Charge	H_2-Corrected Discharge	H_2-Corrected Charge	MS-Charge
Cycle 1	4.15	4.20	3.99	4.35	4.07
Cycle 2	4.12	4.1	4.04	4.12	3.98

Table 4.2: The e^-/O_2 numbers for a Zn-air battery 7 M KOH + 1.4 M KF + 1.4 K_2CO_3 electrolyte with and without H_2-correction and finally the e^-/O_2 as determined by the MS.

Compared to the pure KOH electrolyte, using the additives yield lower deviation from the ideal electron number. This indicates that when accounting for the during discharge there is lower than expected gas consumption while the production during charge is also too small. But because both numbers are above 4 correction for a very small H_2 evolution draws the electron numbers during charge very close to the ideal

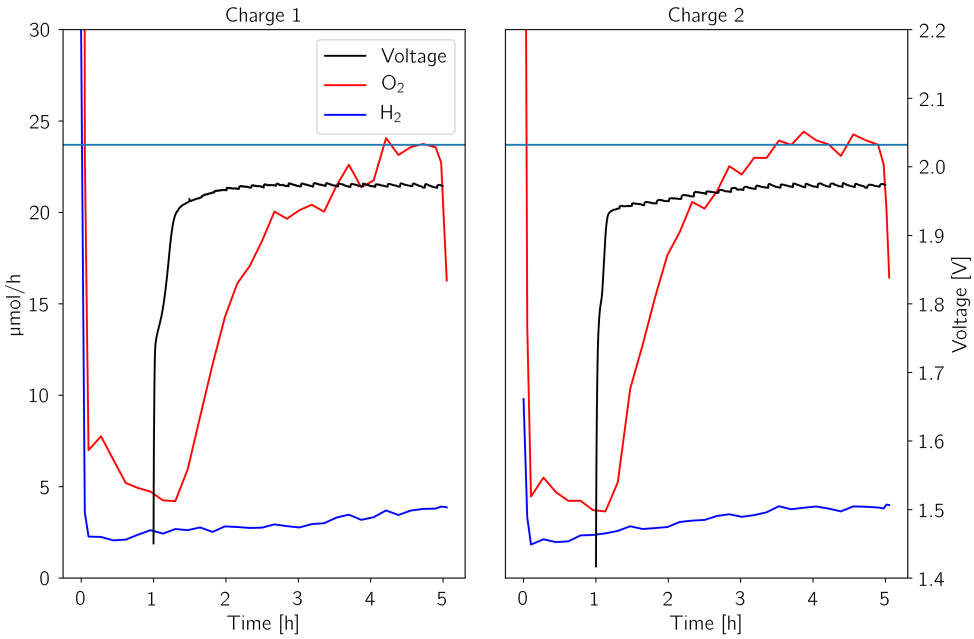

Figure 4.4: MS signals for H_2,O_2, during the first and second charge of a Zn-air battery with a 7 M KOH + 1.4 M KF + 1.4 M K_2CO_3. The blue horizontal lines indicates a the expected O_2 signal for a 4 electron process.

4 while during charge it creates an even larger deficit of gas production. This leads to the conclusion that the additives somehow limit gas production. Applying the mass spec to determine the e^-/O_2 shows a discrepancy between the H_2 corrected numbers and the O_2 signal in the mass spectrometer. This is despite the MS data revealing a low H_2-signal. Summarised e^-/O_2 with and without H_2 correction for this electrolytes can be seen in 4.2.

Applying the mass spec to determine the e^-/O_2 shows a discrepancy between the H_2 corrected numbers and the O_2 signal in the mass spectrometer. This is despite the MS data revealing a low H_2-signal.

4.3 Chloride electrolyte

As opposed to the highly alkaline electrolyte reviewed thus far are a family of near-neutral electrolytes known from Zn electroplating processes. These are based on either $ZnSO_4$ or $ZnCl_2$ in weak acidic solutions ex-

hibit have been shown enable long cycle life [53] [54]. Other benefits are that the lower pH avoids the reaction with CO_2 from the air. The chemistry of this battery is however very dependent on the pH and therefore has to be stabilised by buffers such as NH_4Cl and NH_4OH. Because of this conversion of Zn will only slightly affect the pH of the solution, and thereby the equilibrium of the dissolved intermediates is maintained and unwanted precipitates are avoided. A $ZnCl_2$ solution was prepared and with 0.5 M $ZnCl_2$, 1.6 M NH_4Cl and adjusted to pH 8 by NH_4OH as this electrolyte should favour precipitation of $Zn(OH)_2$[55]. Two batteries where prepared with 200 µL of this electrolyte with and air-electrode made from 75 % wt.MnO_2 and 25 % wt. graphite and a Zn-foil anode was prepared to investigate the gas evolution in these cells, with pressure and the mass spectrometer. The cell has OCV of 1.2 v which is relatively

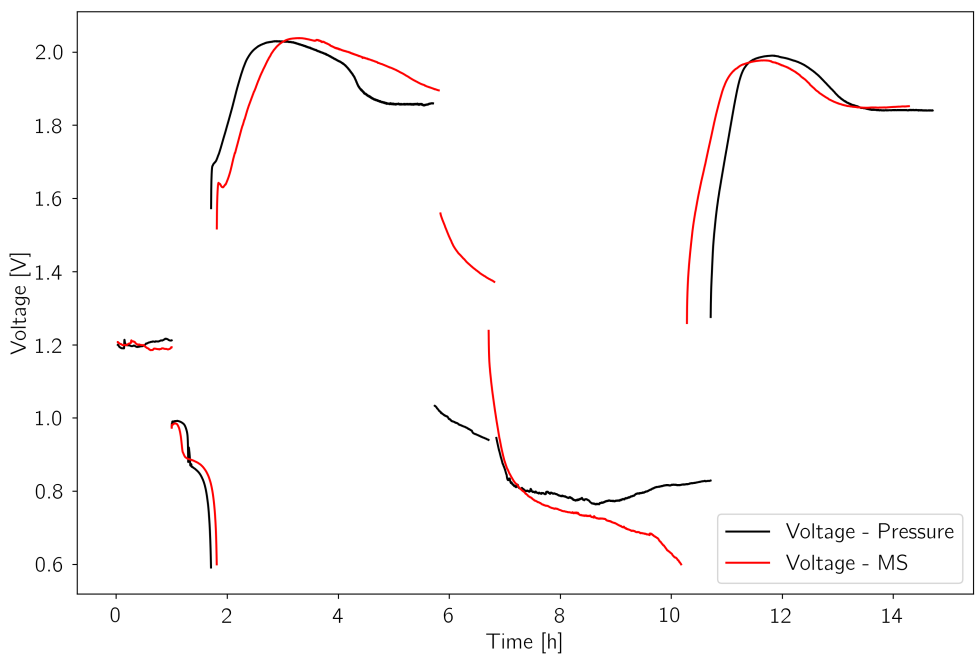

Figure 4.5: Cycling profile for identical two Zn-air cell with an pH 8 ZnCl electrolyte 75 % wt.MnO_2 and 25 % wt. graphite air electrode

stable which is relatively stable. On Charge the current increases to 2 V where OER should be expected but proceeds to fall around 1.8 V until the charge ends. On the second cycle the discharge plateau decreases to 0.8 V with a less smooth discharge profile. The second charge mirrors

the profile in the first charge with the cell reaching 2 V before decreasing. During the charging of cell 2 seen in figure 4.5 the evolved gasses

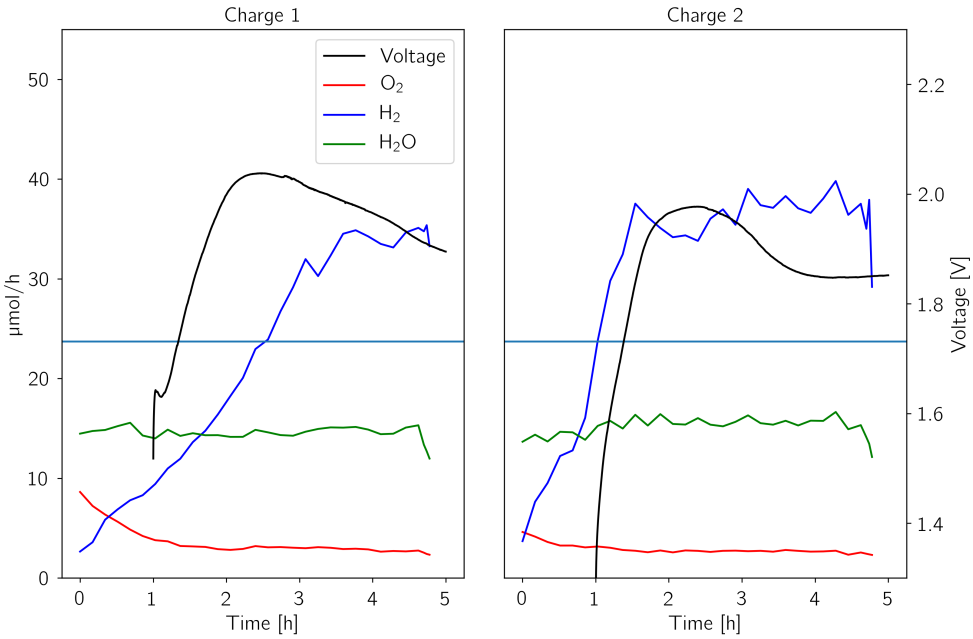

Figure 4.6: MS signals for H_2,O_2,H_2O during the first and second charge of a Zn-air battery with a 200 µL p 8 ZnCl electrolyte

where quantified by the use of the mass spectrometer. In both cycles there is a residual O_2 leftover from the discharge of the cell that was not flushed away between cycles and no O_2 is produced for the remainder of the cycles. The most significant signal is hydrogen which in both cycles reaches 40 µmol/h making electron number calculation without relevance. As with any aqueous electrolyte the vapour pressure of water means it is present in the mass spectrometer data, this complicates the detection of NH_3 that appears on m/z=17 which is also a significant peak for ionised water. The relative intensity of the m/z 17/18 is 0.2 while the measured ratio from 4.6 is $\sim$ 0.3 suggesting that a third of this intensity would be ammonia resulting in a total signal of $\sim$1.5 µmol/h in both cases. A signal this of this magnitude would mean that the lower ionisation m/z for mass 16 and 15 are not seen as these would be below the detection limit. While it has been proposed that Cl containing electrolytes can develop chlorine none of the significant $m/z = 35$ and 37 where detected in this experiment.

4.4 Highly Concentrated Zinc Electrolyte

A neutral electrolyte was proposed by Wang *et. al.* who developed a highly concentrated electrolyte consisting of 1 m $Zn(TFSI)_2$ + 20 20 m LiTFSI for use in Zn batteries because of its ability to limit self corrosion and dendrite growth. They demonstrated how it exhibited high capacity retention for a $Zn/LiMn_2O_4$ battery. To show the versatility of this electrolyte and its ability to enhance Zn deposition without dendrite they created a Zn-air battery with this electrolyte and a porous carbon paper cathode in which the ZnO would precipitate on the air electrode during discharge similar to what is found in aprotic Li-air batteries [56].

Two cell with this electrolyte was created and tested in the DEMS-cell as there is no material constraints in a neutral electrolyte and due to the lower volume which provides higher sensitivity. Using the $NiCo_2O_4$ cathode described applied in figure 4.1. Both cells were cycled twice at The cycling profile can be seen in figure 4.7 with discharge OCV values of 1.2 V and discharge potentials of approximately 0.8 V and charging potentials of 2.0 V which is similar to what Wang and co-authors observe. The pressure in the cell decreasing during OCV and continuing to do so during discharge without change in slope which indicates that the cell is leaking and that the electrochemistry that is occurring during discharge is not a Zn-air battery. During charge the pressure graph breaks indicating that some gas evolution is occurring during charge.

A battery similar to the one figure 4.7a is seen in figure4.7b which was used for DEMS experiments. It exhibts the same cycling parameters as the former battery although there is a dent in discharge profile in the second discharge cycle while the charge plateau is more constant. By reviewing the mass spectrometer data in Figure 4.8 reveals no production of H_2, N_2, O_2,CO, CO_2 or gasses any on any of the other 20 m/z values that are tracked. The only significant signals are H_2O at $\sim$18 µmol/h and the various Ar traces. This could be because the MS is simply not sensitive enough to detect these signals or that the peaks appear on m/z that are higher than range of the qaudropole mass filter can separate. Nevertheless this suggest this the pressure increase in these experiments is not related to the O_2 evolution reaction. The use of a $NiCo_2O_4$ air electrode that is not optimised for deposition of material onto it is surface is undesirable and the low currents will obscure any gas evolution. It is also possible that the electrochemistry in that battery is related to Li-

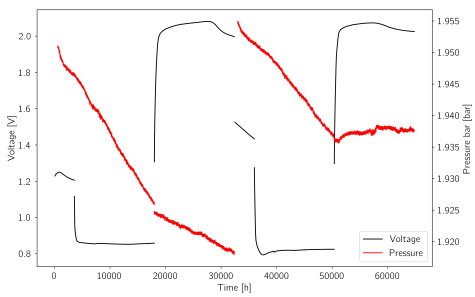

(a) MS signals for H_2,O_2,H_2O during the first charge of a Zn-air battery with a 80 µL of the HZCE electrolyte

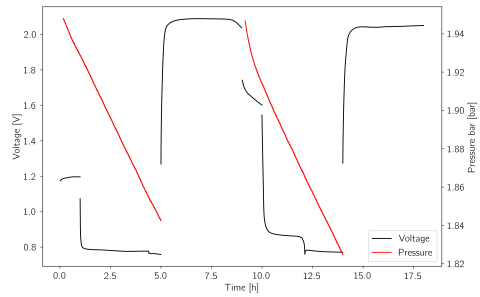

(b) MS signals for H_2,O_2,H_2O during the second charge of a Zn-air battery with a 80 µL of theHZCE electrolyte

Figure 4.7: Cycling profiles for batteries with the HCZE electrolyte cycled at 0.1 mA/cm^2.

intercalation into the $NiCo_2O_4$-cathode material and Zn plating onto the Zn anode.

4.5 Summary of e^-/O_2 on Zn-air batteries

It was possible to determine electron numbers for Zn-air batteries with a KOH electrolyte and demonstrate how H_2 correction is necessary to get accurate determination of e^-/O_2. With the correction it was found that in both discharge and charge was a deficit of gasses consumption and production meaning that there are processes in the battery either consume evolved gasses or consume electrons in processes that do not contribute to gas conversion. Applying the mass spectrometer gave decent agreement with the constant gas assumption until the third cycle likely due to changing surfaces.

The 7 M KOH electrolyte with KF and K_2CO_3 additives had more ideal e^-/O_2 numbers for both charge and discharge, both above 4. Correcting for H_2 drove the charge numbers away from this ideal number while the discharge would within noise. The Mass spectrometer confirmed that the electrolyte with additives is more ideal in terms of H_2 and O_2 evolution during charge. However an unexplained discrepancy between the pressure measurement and mass spectrometer in e^-/O_2 numbers that requires more investigation.

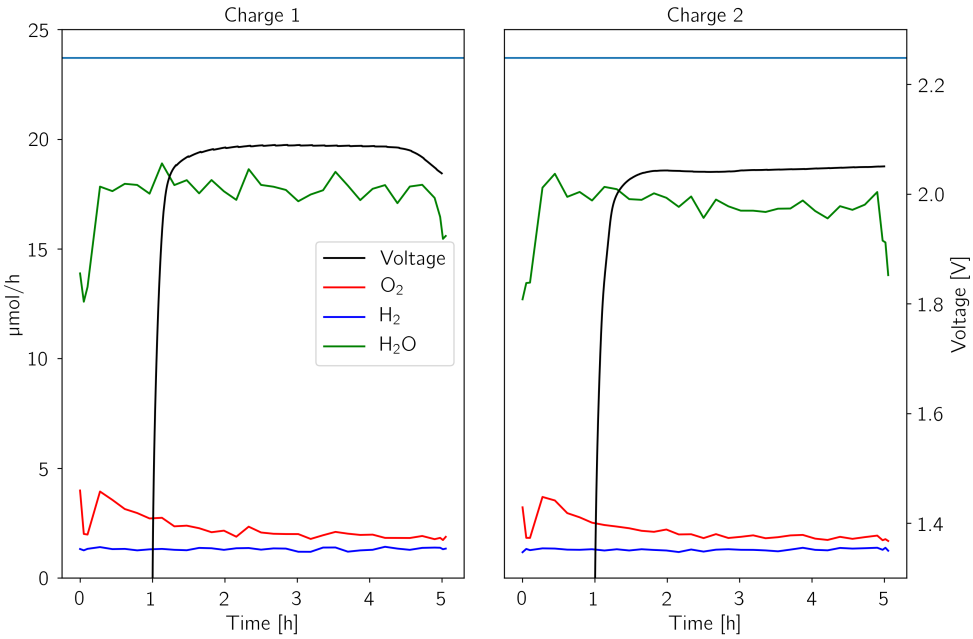

Figure 4.8: MS signals for H_2,O_2,H_2O during the first charge of a Zn-air battery with a 80 µL HZCE electrolyte

The pH8 $ZnCl_2$ exhibited low initial discharge capacity and did not develop O_2 during charge although there was a significant H_2 signal. Although there was discharge capacity in the second discharge there was no O_2 during the corresponding charge. The ammonia signal was determined to be 1.5 µmol/h and no Chlorine evolution was detected.

Using the highly concentrated Zn-Ion electrolyte was found to not involve any consumption or production of O_2 in detectable amounts. The pressure measurement did suggest there was slight gas evolution during charging. It was not possible to determine the makeup of this gas despite tracking 25 m/z ratios across a range from 2 to 56. It is suggested that what is driving the electrochemistry is intercalation of Li-ion into the $NiCo_2O_4$-cathode.

In summation from the experiment herein, the non alkaline electrolytes require more investigation and possibly other catalyst, the alkaline KOH electrolytes exhibit meaning O_2 evolution that is similar for 2-3 cycles. Going forward understanding H_2 evolution during will be important to develop long lasting Zn-air batteries.

Chapter 5

Dopants and the Effect on Self Corrosion

This chapter will cover the content of paper II with focus on the experimental part, including some additional measurements and figures to clarify and underline the results presented therein. As the content of paper is a combination of theory and experiments, the theory part will be explained here and related to the results in order to convey the full message.

The challenge of preventing self corrosion was initially addressed by adding Hg to the anode material of at least $100\,\mathrm{g/cm^2}$, which was patented and applied in Zn batteries [57][58]. As the toxicity of Hg became increasingly apparent, legislation was put into place to curtail its use and a replacement was needed. A number of materials were considered as replacements, and in 1994 various mixtures of Al, Bi, In, Ca and Li added to Zn powder in dopant levels were patented [59]. These mixtures have since been applied and investigated in a number of publications. Indium, while soluble in Zn [60], was proven to segregate between the grain boundaries of Zn, which promotes Zn dissolution and decreases the Hydrogen Evolution reaction, (HER) rate [61]. Alloying Zn with Ni and In can in certain combination reduce dendrite formation and shift the HER towards more negative potentials [62]. Another commonly found dopant in Zn powders, Bi, has a very low solubility of 0.1 % in Zn [63] and can be used to improve the conductivity of Zn particles [64][65]. It has been suggested that Bi is mostly beneficial in combination with other dopants, as it was found to precipitate into the grain boundaries of Zn

in the soldering material Sn_8Zn_3Bi[66] where it cannot affect the Zn surface. In combination with $Ca(OH)_2$, Bi has been suggested to increase the number of cycles achievable by reducing dendrite growth [67][68]. The co-dopant efficiency of In and Bi was investigated by Yano *et. al.* and it was found that the dopants reduced the HER rate by the same amount as a Hg dopant.

The way these elements affect the HER is understood once the mechanism is investigated. However, this requires a reiteration of how Zn behaves during cycling. Zincate formation originates from Zn atoms accepting OH^- until it goes into solution as $Zn(OH)_3{}^-$, where it can accept another hydroxide ion to form $Zn(OH)_4{}^{2-}$, as summed up in the following equations:

$$Zn4OH^- \leftrightarrow Zn(OH) + 3OH^- + e^- \leftrightarrow Zn(OH)_2 + 2OH^- + 2e^- \quad (5.1)$$

$$Zn(OH)_2 + 2OH^- + 2e^- \leftrightarrow [Zn(OH)_3]^- + OH^- + 2e^- \leftrightarrow [Zn(OH)_4]^{2-} + 2e^- \quad (5.2)$$

5.1 A Brief Summary of DFT

It is beyond the scope of this thesis to cover in detail the fundamentals of Density Functional Theory (DFT). In *very* short, DFT is a framework by which the ground state electronic density of a quantum mechanical system can be calculated numerically, the required chemical properties including the energy can be determined with the density. By dealing with the electronic density rather than individual electrons, the size the of the calculation required is reduced to within supercomputer levels. The procedure is in principle exact apart from an approximated exchange correlation functional that exists in many flavors and forms. Picking the right functional for your system is a compromise between accuracy and computational cost.

5.2 Zinc Surfaces and Self Corrosion

In paper I, the impact of dopants in the Zn electrode self corrosion or gassing was investigated. The active material, Zn, is consumed by reaction with water, leaving $Zn(OH)_2$ according to reaction 1.3. This is

detrimental for both primary and secondary Zn air batteries, as it reduces the discharge capacity. For secondary batteries it is a recurring problem, because the zinc hydroxide is converted back during charge. However, this presents another problem over the life of the battery, aside from the reduced coulombic efficiency and capacity loss; the electrolyte is consumed during gassing.

In 2013, Siahrostami *et al.* applied DFT to investigate the dissolution of Zn on pure Zn surfaces[69] and found that kink sites were favourable for dissolution of Zn compared to a surface site. The Zn (0001) surface binds each atom strongly, and creating a vacancy is furthermore associated with an energy barrier. At the edge of a Zn surface, while the atom is not nearly as strongly bound as at the surface, there is still an associated energy barrier, unlike at the kink sites where the surface is the same before and after the outermost Zn atom is removed. Even so, the free energy diagram shown in Figure 5.1 reveals that the kink site and edge have a very similar potential. When accounting for the formation of the vacancy in the two final steps in reaction step 5.2, determined to be 0.35 eV, the kink sites become favourable.

With the mechanism for Zn dissolution clarified, there is now a basis for introducing dopants and evaluating their effect on the HER and zincate formation. However, since these reactions are confined to the surface, it is essential to determine if a dopant will remain at the surface. During charging, Zn atoms will continuously be added to the kinks, driving away any dopants from the reaction sites and thus diminishing their effect. Reviewing the relative energy of different sites in the Zn surface in Figure 5.2, it is seen that Ag is unlikely to stay at the surface, as the energy for bulk sites, coordination 9-12, is very similar to lower coordinated sites. Silver was included in this study because it is a promising catalyst in combination with Co_3O_4, which could leech into the anode during cycling [70]. In contrast, the established dopants Bi and In largely favour kink and edge sites. As such, these elements that are applied in primary batteries can be used in secondary batteries as well.

5.3 Understanding the Effect of Bi and In.

When reviewing the patents on Zn powders, most of the described mixtures contain some quantity of both Bi and In, as does the commercial

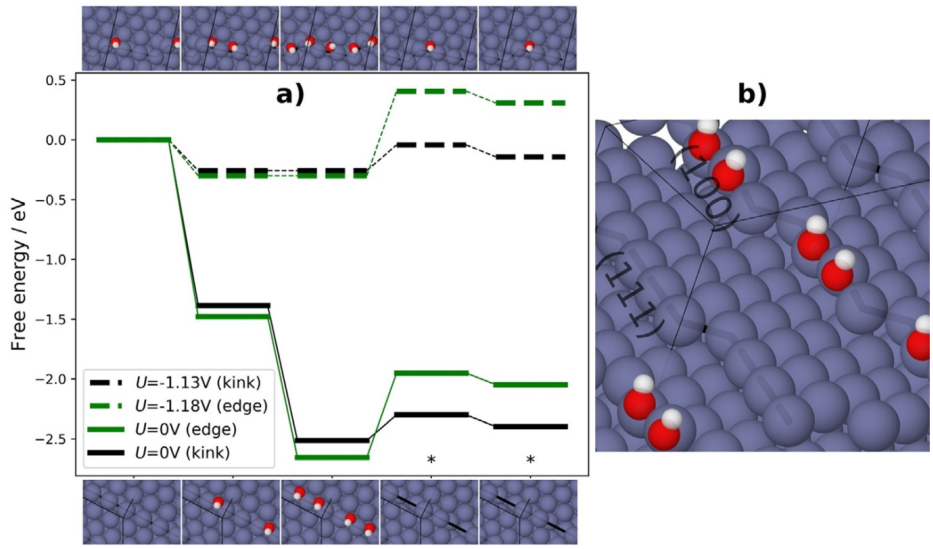

Figure 5.1: a) Free energy diagram for each step of the Zn dissolution reaction on a kink (black) and edge (green) edge-site, respectively. The dashed lines show the free energies when a limiting potential is applied. The two final steps marked by * are fixed to experimentally determined dissolution potentials. Above and below the graph the mechanisms by which Zn is dissolved at a kink and edge site are displayed. Zn is indicated in grey, O in red, and H in white. b) Side view of the second step where Zn is dissolved from a kink site with indicated planes.

powder from Umicore. The affinity of In and Bi towards lower coordinated sites, mean they both stay at the surface during cycling is an essential property to positively affect the Zn for many cycles. To understand the effect of these combinations, the DFT calculations of Zn dissolution in Figure 5.1 are revisited, but now with the dopants present at the surface, which is shown in Figure 5.3. With the Bi now at the kink site, OH is forced to react at an edge site, which now operates at the previously determined potential of 1.18 V. When the step is doped with In, the OH now binds with the neighbouring Zn atom and when this dissolves, the In will rearrange itself into this position, avoiding the penalty of creating a vacancy. The determined limiting potential of this reaction is 1.21 V, which is closer to the equilibrium potential of 1.199 V resembles this fact. When In and Bi are added together, this configuration is stabilised by 0.1 eV compared to the In-In and Bi-Bi doping. The effect of Ag was determined to be similar to effect of Bi, in the sense

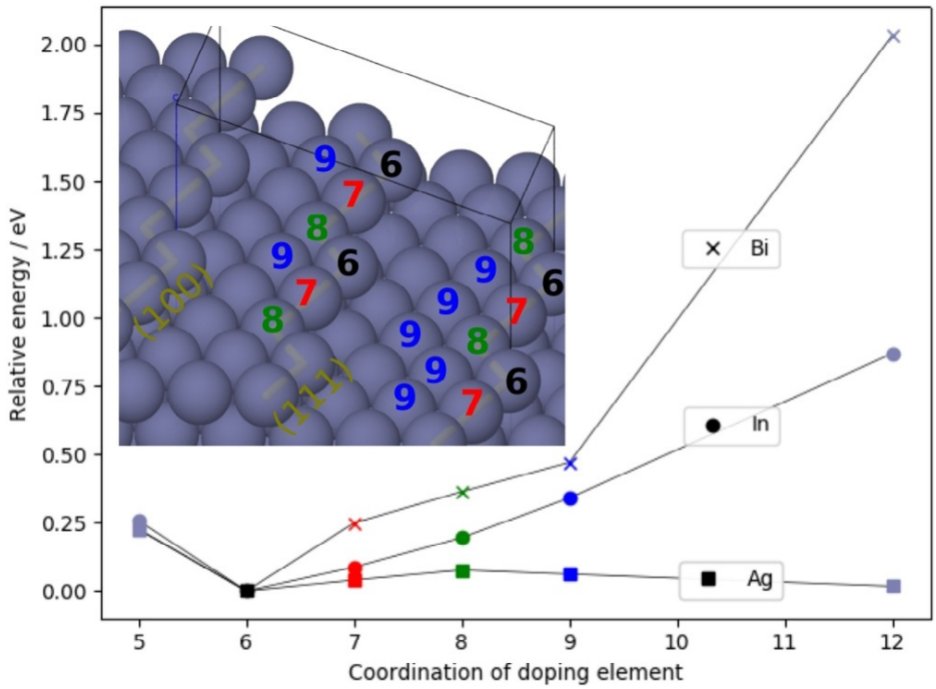

Figure 5.2: Relative energy of Ag, Bi and In in differently coordinated sites at the Zn surface, normalised with respect to kink sites (coordination 6). The insert indicates sites with coordination 6 (kink), 7 (edge), 8 (behind kink), 9 (surface site) and the two micro facets (100 and 111).

that Ag forces OH away from the kink sites. To understand the usefulness of Bi in commercial pastes, the binding of hydrogen adsorbates and ultimately H_2 evolution have to be examined.

Figure 5.4 shows the binding energies of OH and H adsorbates on a Zn surface with different dopants. The result is that Bi and Ag increase the free energy gained by binding OH to the surface more than they increase the binding of the H adsorbate, likely because they are blocking the edge sites, especially in large concentrations. For the In dopant, the binding energies increase until 2/3 coverage, where it decreases again for both H and OH. The beneficial effect of In is that the OH binding energy decreases more than the H binding energy. From Figure 5.4 it is not clear how combined In and Bi doping is beneficial, as OH binding is heavily increased, but it could be argued that the curve should be shifted right by 1 due to the increased number of dopants at the surface. The

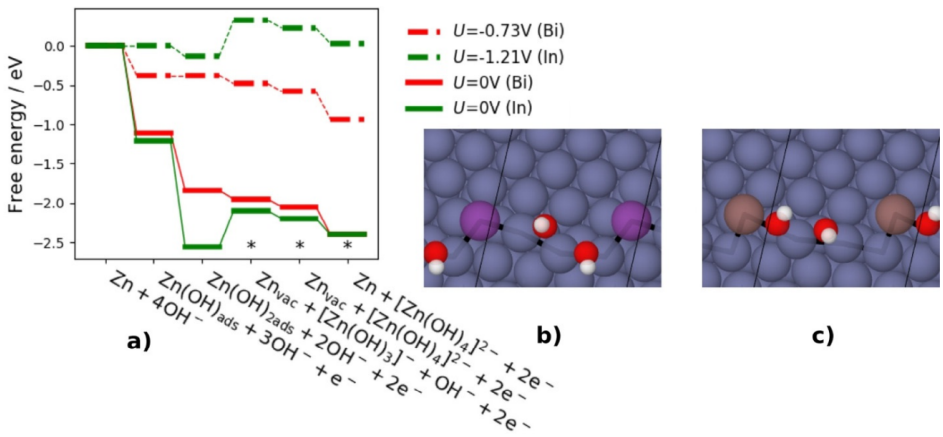

Figure 5.3: Free energy diagram of electrochemical Zn dissolution at a Zn surface doped with In and Bi with a limiting potential (dashed line) and without (full line). The * indicates steps that are fixed to experimental values. b) and d) is the structure of the second step with Bi and In doping respectively.

H adsorbate binding energy is pushed to values where the surface (0001) can also adsorb H, which does not incur H_2-evolution in a rate that is detrimental to the battery.

5.4 DEMS Experiments with Dopants

To verify the findings discussed above, 5 Zn-air batteries were assembled, 1 reference and 4 doped with Ag, Bi, In and an equal mixture of In+Bi. These additives were added in nitrate solutions made from $In(NO_3)_3 \cdot xH_2O$, $Bi(NO_3)_3 \cdot 5\,H_2O$, AgCl and $Ga(NO_3)_3 \cdot xH_2O$ that were all at least 99.9 % pure. The amount of dopant was 28 µL of 0.005 M, calculated using the anhydrous weight, nitrate solution to the KOH electrolyte, based on the anhydrous molar weight, which was added to the 200 µL 6 M KOH electrolyte. As such, the total molarity of dopants is 0.61 mM, which is roughly a factor 20 of the number of atoms on a flat 0001 Zn surface. The anode was a 18 mm wide and 0.125 mm thick 99 % pure Zn foil. Given the way the additives are added, it is likely that the surface concentration is significantly higher than the original patent suggests[59].

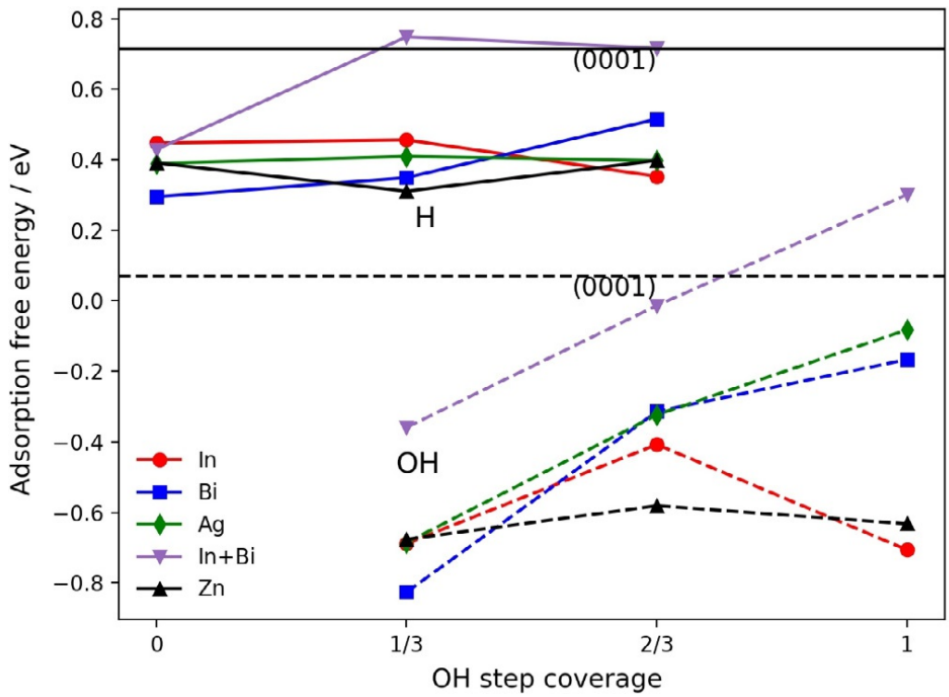

Figure 5.4: Binding energy of H- and OH adsorbates at kink sites of Zn surfaces doped with In, Bi and Ag, respectively, as function of OH adsorbed. The horizontal lines represent the adsorption energies of the adsorbates of a (0001) terrace.

Each battery was held at OCV for 10 h before being discharged and charged for 4 hours at 1 mA/cm^2, resulting in the electrochemical profiles seen in Figure 5.5. The OCV period of 10 h was found to be necessary to allow the dopant and nitrate solutions to establish an equilibrium in the electrolyte. The specific mechanism was not determined and is likely different depending on the species, however, without this long OCV time the batteries would settle on a charging plateau 1.8 V and not produce any gases.

The dopants affect the cycling behaviour both in terms of electrochemical properties and the gas evolution from the cell. It is seen in Figure 5.5 that the reference battery, without dopants, has the lowest discharge potential of any of the batteries through all three cycles, especially in the final two cycles where the reference battery voltage starts to decline rapidly during discharge. The charge plateau for the reference sample is also the lowest

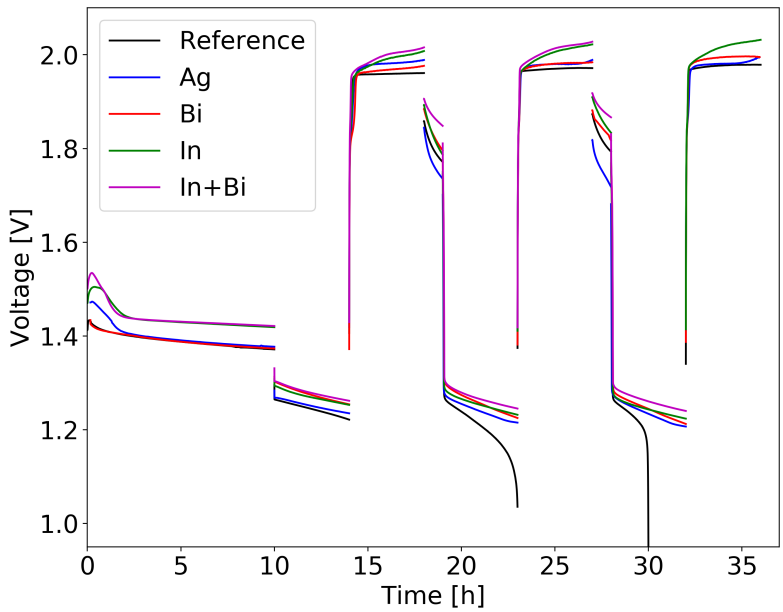

Figure 5.5: Galvanostatic cycling data for 5 Zn-air batteries, 1 reference without any dopants (black) and 4 with different dopants. The additives are Ag (blue), Bi (red), In (green) and a 50:50 mixture of In and Bi (magenta). The initial OCV measurement time was 10 h and 1 h OCV was held between cycles. Discharge and charge times were limited to 4 h.

of the samples throughout cycling. In the third and final cycle, the charge continues well beyond what would be expected the because the discharge was cut short by almost two hours. That means that there is leftover ZnO and Zincate in the cell. It is conceivable that the charge continues due to competition between $Zn(OH)_2$ produced by the HER and conversion of ZnO produced during discharge. The battery with Ag dopants has the second lowest potential of all the batteries and its performance is very similar to the reference battery's. In the first charge the Ag-doped battery has the third highest potential, surpassed by the batteries with In. In the second and third cycle the potential decreases slightly. The In-doped batteries exhibit the highest OCV, discharge potentials and charging potentials, although with only In doping the discharge potential wanes with time.

The oxygen and hydrogen evolution for each battery during each charge is shown in Figure 5.6 broken down into hourly average production, with

row c) showing the ratio between these signals. The oxygen signal is nearly the same in all instances except for the Ag-doped battery where it drops after the first cycle. It is worth noting that even after 4 h the oxygen signal still has not plateaued although in all cases the signal is going towards a slope of zero. Interestingly, it seems the battery with Ag-dopants largely stops functioning after the first cycle, as the hydrogen signal is the largest during the first charge but drops in the following two cycles. The hydrogen output of the reference sample doubles after the first cycle, possibly due to increased surface area, while the oxygen output is constant.

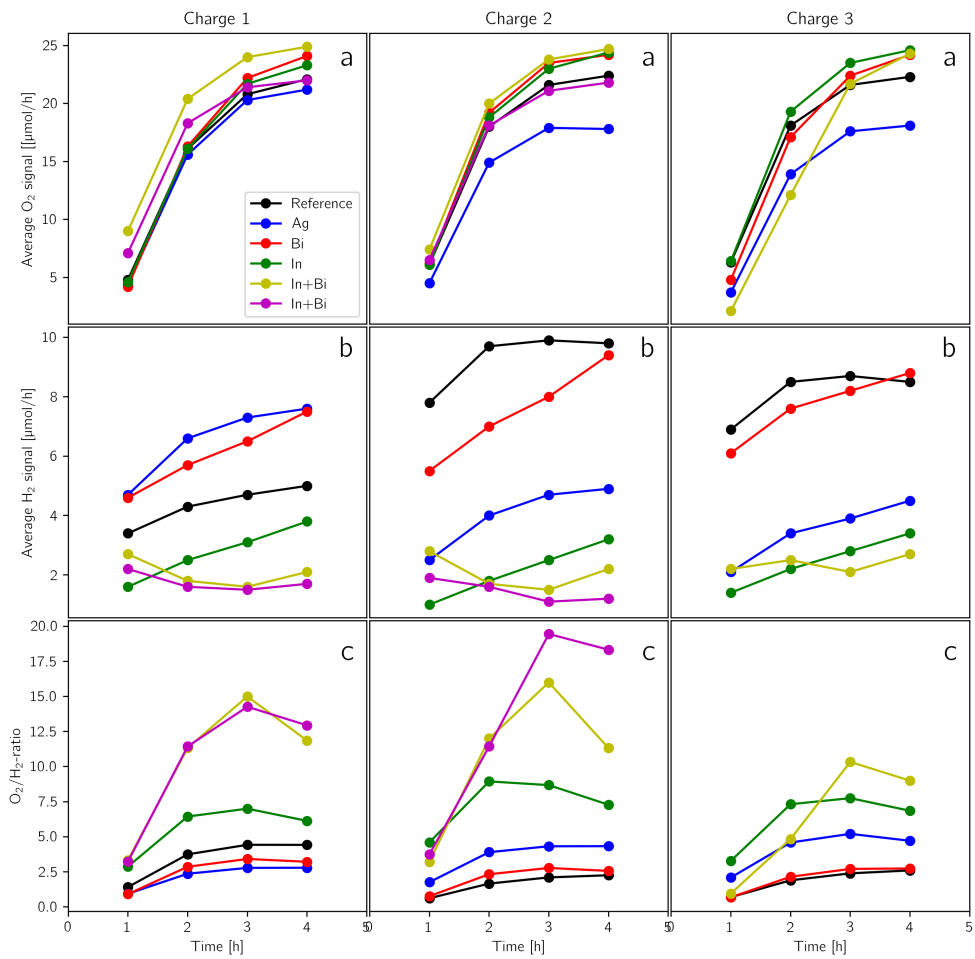

Figure 5.6: Average hourly production of a) O_2 and b) H_2 in µmol h^{-1} and c) the ratio O_2/H_2.

The Bi-doped battery initially exhibits higher hydrogen evolution than the reference battery, but stabilises over in the following cycles. The In-doped battery has consistently lower H_2 evolution than the other single dopant batteries and still exhibits high O_2 evolution, yielding a very favourable ratio of approximately 7.5 between oxygen and hydrogen. The 50:50% In and Bi mixture is superior to the reference battery and the dopants by themselves, as both batteries with this dopant-mixture exhibit very low hydrogen evolution across all cycles. Not only is the hydrogen signal lower, the signal also stays low throughout the charges, which indicates that the combination of In and Bi at the surface has a synergetic effect. No significant CO_2 or N_2 evolution was detected in these experiments.

5.5 Zn/ZnO Paste Anode

The company Everzinc (formerly Umicore) provides BIA100 Zn powder with these dopants, which according to their own analysis contain Bi, In and Al in concentrations of 95 ppm, 87 ppm and 197 ppm, respectively, along with Pb, Fe and Cu all bellow 10 ppm. The powder has a stated gassing rate of 1.87 µl/g/day at 45 °C after 72 h. A cell otherwise identical to the cells with dopants was created, but with a mixture of this Zn-powder and a ZnO powder from the same company in a composition of 49.3% Zn, 21.1% ZnO, 28.2% electrolyte, and 1.4% CMC, and tested for gas evolution during five hour long charges.

The gas evolution from the paste cell is seen in Figure 5.7. It is immediately clear that the O_2 evolution is about ∼17 µmol/h lower than in the comparable dopant experiments and also well below what could be expected at this current. The accompanying H_2 signal is on average ∼5.3 µmol/h, which is similar to the reference battery and inferior to the batteries with dopants that contains In, but the level is almost constant throughout the cycle. Comparing the gassing ratio to the doped batteries is difficult, however, due to the area difference. It is also seen that the gas evolution starts before the current is applied, meaning that the evolution is entirely from chemical HER. In following cycles the gas evolution is essentially similar to the first cycle, indicating that this mixture is very stable over time. The to tal mass of the paste was 207.6 mg, which yields a gassing rate of 1.1 mL/h/g of Zn at standard conditions. This is well above what Everzinc reports, which is likely due to their measurement

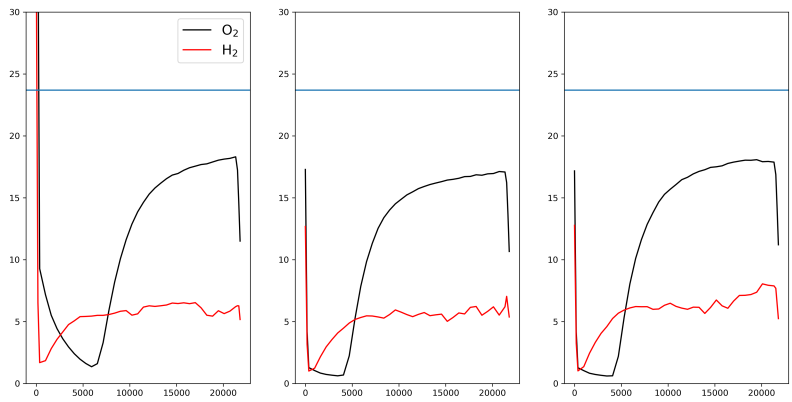

Figure 5.7: Gas evolution from a Zn-air battery with Zn/ZnO paste anode during charging in three discharge/charge cycles for 4 h each way at 1 mA/cm^2.

method including a static system, while the present value represents a model battery. The Zn powder contains other additives, but the paste contains ZnO powder that is 99.99 % pure, and it is uncertain how this behaves when the ZnO is converted to Zn during charging. Finally, it is unknown how the gelling agent CMC contributes to gas evolution.

5.6 Summary of Dopants and Their Effect on Self Corrosion

Through DFT, the mechanism of Zn dissolution was elucidated and determined to occur through the kink sites, because it would avoid the energy penalty of creating a vacancy. It was determined that the commonly used additives in primary batteries, In and Bi, would be suited for secondary batteries due to the relative energy loss in highly coordinated (bulk and surface) sites, while Ag would favour higher coordination (bulk sites). The individual contributions from In and Bi were found by DFT to originate from the way these elements affect the energy of OH attached to the kink sites, with Bi hampering the binding and In increasing it, despite rearrangement. Finally, the combined effect of In+Bi was explained by individually reviewing the O and OH binding energy of the surface of

Zn.

A reference Zn-air battery was cycled 3 times and determined to have a O_2/H_2 ratio of almost 5 in the first cycle, after which it would decrease to below 2.5. This showed how a pure Zn surface is unable to reach high cycling numbers in highly alkaline media. Adding Bi and In is beneficial to the discharge voltage, but alone the effect deteriorates over time. In terms of gas evolution, Bi is similar to Ag with very high H_2 evolution, while In has almost no hydrogen evolution. Ag dopants were found to be detrimental to the batteries' performance as they resulted in high hydrogen evolution and lower oxygen evolution, although it was suggested to move away from the Zn-surface over time due Zn plating. Adding Bi and In together was beneficial for the discharge plateau, and now the effect lasts through all three cycles. Adding any dopant with In increased the charging plateau by roughly 0.025 V by the end of the cycle. The hydrogen signals were, however, the lowest of all the dopants at levels below 3 µmol/h, a level which was maintained over all three cycles. This leads to the conclusion that In and Bi co-doping is the superior of the investigated dopants, in agreement with the DFT simulations.

A Zn-air battery with a Zn/ZnO oxide paste anode was tested, with the commercial Zn powder containing In and Bi in 95 ppm and 197 ppm concentrations, respectively. This battery was to evolve H_2 at a level of 5 µmol/h, slightly higher than for the Zn foil experiments. The rate of H_2 evolution was determined to be 1.1 mL/h/g of Zn, which worked out to be was considerable higher than the raw materails, gassing rate. Indicating that in a full battery testing gassing is increased. Unlike the foils these levels were constant and similar in each cycle indicating the robustness of these dopants.

Further improvement of this work would include conducting more cycles on each single battery with the different dopants. Preferably, the dopants could be added in other chemicals such as acetates or dry mixing and an oxidised dopant powder with Zn powder. It would also be beneficial to conduct experiment with lower concentrations of dopants than applied in these experiment to elucidate the co-dopant effect of In and Bi.

Chapter 6

Transformation and Migration of Zn/ZnO in Secondary Zn-air Batteries

A fundamental mechanism of the alkaline Zn-air battery is the conversion of the anode through precipitation of ZnO and dissolution of Zn. Both mechanisms rely on the intermediate $Zn(OH)_4{}^{2-}$. As such, the transport and concentration of this species determines the structure of the anode, and thereby the voltage profile and cycle life of the battery. Since there are only a few commercial and proposed batteries that employ Zn in their chemistry, such as the Zn-Ag, Ni-Zn, Zn-MnO and finally Zn-air batteries, the structure and growth of Zn has been investigated in literature by both XRD, tomography and other in situ techniques. Horn *et. al.* investigated the Zn-MnO battery using SEM and found that ZnO deposition is heavily influenced by the current applied to the anode [71]. Commercial Zn-air batteries have been investigated by Schröder *et. al.* using tomography, who determined that Zn conversion begins at the separator and progresses away from this interface. In the process, it was found that the structural expansion ratio could be as high as 1.5 [72]. By also applying tomography, Arlt *et. al.* developed a custom battery cell for Zn-air batteries and found that the pores of the air electrode would be flooded by the electrolyte as the anode expands, leading to early end of life [73]. Improving on the same technique, Franke-Lang *et. al.* found it was beneficial to decrease the Zn anode size, as in would let the anode accommodate the expansion during discharge. It was also suggested

that bubble formation could displace loose particles for detrimental effects in the battery. Furthermore, it was possible to show that Zn would deposit in the cathode, confirming that the intermediate zincate can be transported through the separator [74]. Naktata *et. al.* applied in situ XRD and X-ray tomography on Zn-electrodes, where it was shown that low currents could completely dissolve dendrites. Following this, it was found that suppressing non-uniform Zn deposition would enhance cycle life [75][76].

The present study focuses on a Zn-air battery with a Zn/ZnO anode, as the addition of ZnO improves cycle life by providing nucleation sites for ZnO [48][77]. The Zn/ZnO applied herein was developed by Mainar *et. al.*, and it was found to encourage homogeneous deposition of ZnO on the anode. The paste consisted of 49.3 wt % Zn, 21.1 wt % ZnO, 28.2 wt % electrolyte, and 1.4 wt % carboxymethyl cellulose (CMC). To elucidate how the structure of this anode changes during cycling, a capillary battery was created. The goal was to achieve very high time-resolution and obtain spacial information; therefore the cell was kept very small. The anode and cathode were 1.6 mm in diameter and required another 1.4 mm of glass around them where the X-ray beam would hit the sample.

Sample	Cathode	Time [h]	Current [mA]	Segments
Zn1	10.0 $NiCo_2O_4$ + 15 % wt.PTFE	4	0.5	10
Zn2	9.2 $NiCo_2O_4$ + 25 % wt. PTFE	1.25	0.4	8
Zn3	10.3 $NiCo_2O_4$ + 15 % wt. PTFE + 10 % wt. graphite	1	0.25	8
Tomography	$NiCo_2O_4$ + 15 % wt. PTFE	4	0.5	~ 8

Table 6.1: Overview of the parameters of the Zn-air capillaries presented in the present document, with sample name, capacity, cathode configuration and cycle parameters.

Table 6.1 provides an overview of the capillary batteries tested in the beam line and of the tomography battery. It was not possible to weigh

the anode for the tomography battery but from the resolution of the tomography the height of the sample was estimated to be $\sim 1.41\,\mathrm{mm}$. This would yield at least 8 segments, resulting in a capacity in the same range as the other samples.

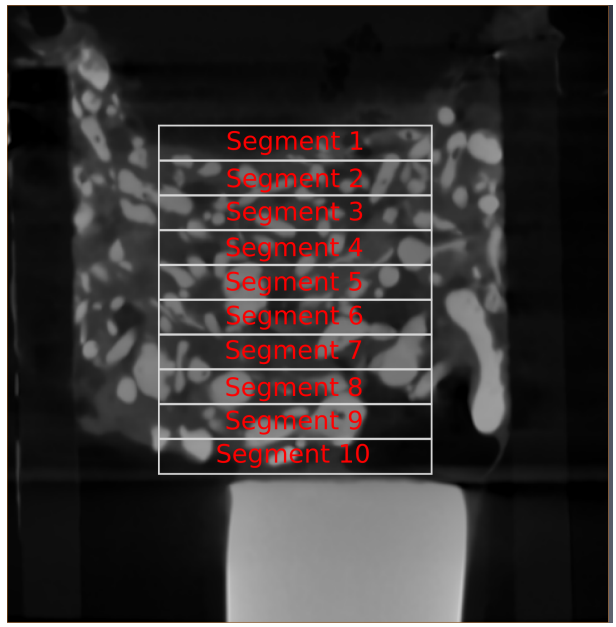

Figure 6.1: Cross section of a Zn/ZnO anode for a Zn-air battery with the segments highlighted.

The electrochemical performance can be seen in Figure 6.2. The cells exhibit a flat voltage plateau on both discharge and charge with OCV values around 1.4 V, discharge potential of 1.0 V and charge potential of 2.0 V, which is acceptable for a Zn-air battery. The cycling parameters for the cells was a balancing act between observing changes in the XRD patterns and not overwhelming the anode with deep discharges and high currents. The longest lifetime achieved was $\sim 12\,\mathrm{h}$ at currents between 0.25 and 0.5 mA. This is in contrast to the tomography cell which ran for more than 20 h, but with a significant overpotential on discharge. The overpotential on discharge was likely related to difficulty for the cathode to run the ORR reaction, which could be due to a an issues with the wetting of the air-electrode, this is seen by the fact that the overpotential is only present on discharge.

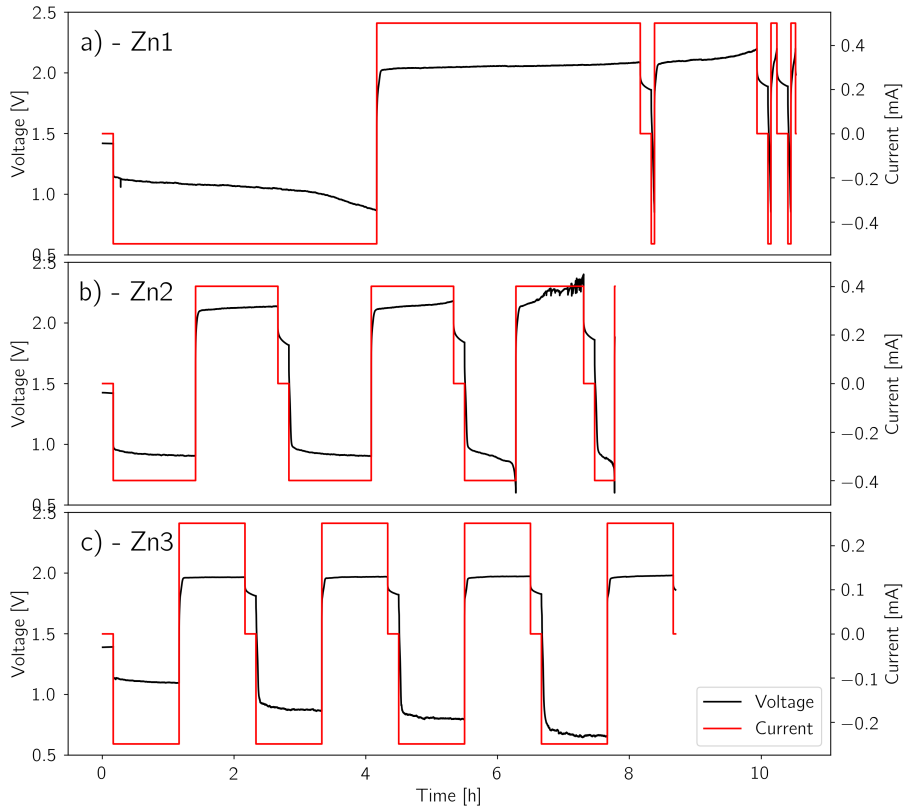

Figure 6.2: The cycling data for two batteries Zn-air batteries capillary cell at 0.5 mA in 4 hour long cycles (top) and 0.4 mA in 1 h hour long cyles

6.1 XRD-Experimental Details

The *in situ* synchrotron experiment were conducted at the scattering beamline P02.1 at the PETRA III syncrotron in Germany [78]. The X-ray beam was conditioned by a diamond 111 Laue crystal and a silicon 111 Lause crystal and collimanted by slits. The wavelength was determined to be 0.2072 Å, using a diffraction pattern standard of silicon provided by NIST. The data was collected using a Perkin Elemer XRD 1621 area detector with an area of 400x 400 mm^2 and with a pixel size

of 200x200 µm^2. Calibration of the tilt parameters, beamcenter, sample detector distance was performed using a LaB_6 standard sample and was handled in the DAWN software [79][80]. For the data reduction a mask was applied for the beam stop and threshold mask was applied to eliminate over-exposed pixel from the large zinc crystalites. Each segment was exposed by the beam 10 s before the stage would move the sample so that beam would expose the segment below, the resulting time bet weens exposures is roghly 2 min which accounts for the beam exposure and the movement of the stage. When the entire sequence of the sample was scanned the stage would be lowered to return the beam so that it would expose the top segment. The detector used in these experiments experience "afterglow" meaning that the pixel may not be cleared entirely during the reading process, and will therefore contribute to to the intensity in the following images. To counter this effect, a dark image (i.e. no exposure) would be collected with regular intervals of 10 min to compensate for for this effect. This is why there appears to be gaps in the data for every 5 data points in figure 6.7b.

6.1.1 XRD-Results

For each segment of the anode detector images, cutouts such as the ones shown in Figure 6.3, were obtained during cycling and converted into diffractograms. For sample Zn1, The peaks of both Zn and ZnO are clearly visible in figure 6.4 and it is also immediately apparent that the intensity of the peaks change over time.

Due the size distribution of the Umicore BIA100 Zn powder that was used in the anode, which had with some very large Zn crystallites, the detector became saturated. This is also clearly visible in the detector images, where the Debye-Scherrer rings are broken initially. Consequently diffraction peaks are difficult to fit, and Rietveld or Lebail refinement could not be employed effectively. The fine ZnO crystallites, yield well-defined and smooth Debye-Scherrer rings. To track the changes in the anode, each peak in the diffractogram was identified, the amorphous scattering background was subtracted, and peaks were normalised to the inital background scattering intensity between the ZnO 100 and ZnO 002 peak in the initial scan which is illustrated in Figure 6.5. The synchrotron runs in top-up-mode, which results in very small variations in the ring current of $\sim 1\,\%$, and where therefore not corrected for this. This analysis led to 110 identified peaks that were tracked over time for each

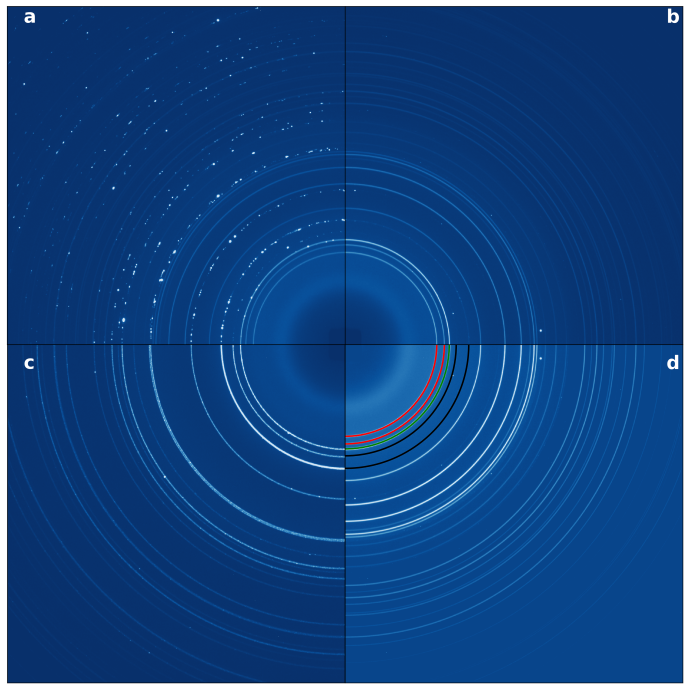

Figure 6.3: Cutout of detector images obtained during cycling for the Zn1 sample 0.2 mm beneath the anode electrode interface (AEI) in the anode. a) Is obtained during the initial OCV ,b) Is after 4 hours of discharge, c) the anode an additional 4 hours of charging) Is a reference image to facilitate interpretation using highlighted Debye-Sherrer rings. The red ring corresponds to ZnO, green to overlapping reflections between Zn and ZnO and black to Zn.

segment of the sample, an example for a single segment and tracking the peaks over time can be seen in the appendix Figure 8.1 and 8.2. Aside from a few instances where Zn and ZnO reflections overlap the trend for all the reflections of each compound follow the same trend. Therefore, the Zn 102 peak and the ZnO 002 reflections were used as descriptors for the overall Zn and ZnO amount in the sample, even though the Zn signal is not a perfect descriptor.

The intensity for these peaks in the entire sample can be seen in Figure 6.6 a). For the Zn1 sample with deep discharge there is a clear inverse relation between to material in the anode, however, after first 8 hours (4 hours of discharge and 4 hours of charge) the ZnO intensity is slightly lower than initially and Zn is slightly higher compared to when the cycle

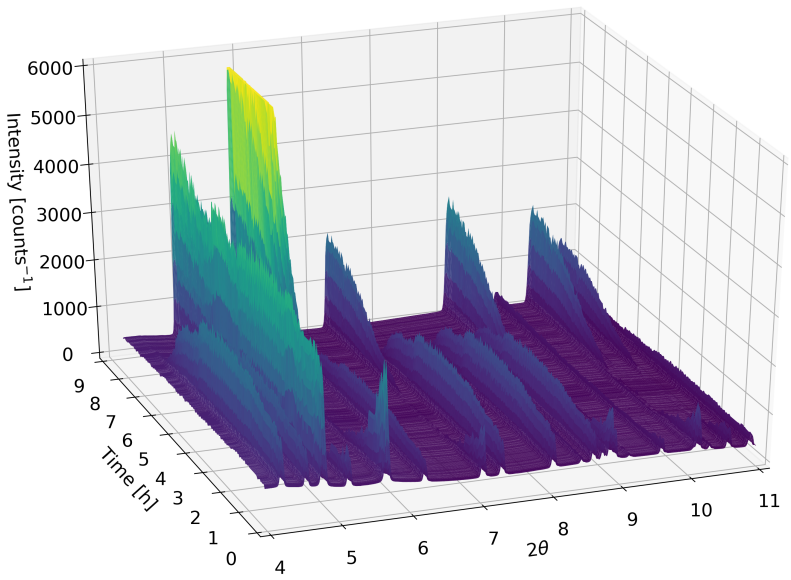

Figure 6.4: Time resolved XRD data of the Zn/ZnO anode during cycling in a Zn-air capillary battery. The data is cropped at 6000 counts/s to enhance the contrast of the lower intensity reflections.

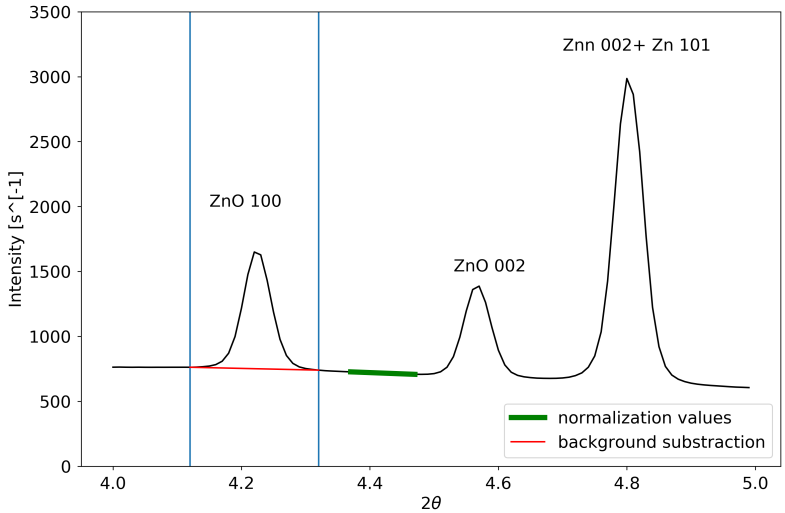

Figure 6.5: Example of XRD data that show how a peak value was background subtracted and the values to which they where normalised

started. After a brief attempt to discharge the cell, which was unsuccessful despite there being available Zn and ZnO nucleation sites, the charge resumes. The increase in Zn signal continues until around the 10 h.

For the other sample in 6.6 b) where the discharge depth of discharge was 1/4 of the first sample, the ZnO intensity increased during discharge but decreased more during charge. After 6 hours the amount of ZnO the anode was reduced by half, with the remainder of the ZnO located in the bottom. Meaning that both samples experience an overall loss of ZnO in the anode. The Zn signal is seemingly constant which is likely due to the error associated with the very large crystalites in the Zn powder.

To further understand the conversion and the change in Zn and ZnO, the segments were reviewed individually. The top segment containing the anode-separator interface is shown in Figure 6.7a and 6.7b. The the top segments require special attention as the amount of material is small due to curvature of the sample and difficulty with identifying the interface. Which makes it difficult to get reliable conclusions. The initial intensities indicate that the amount of material in the interface is about 10 % of the segments below, which results in dramatic changes in the intensities. For the Zn1 sample, the Zn signal levels out after two hours but does not deplete entirely, which could indicate that some

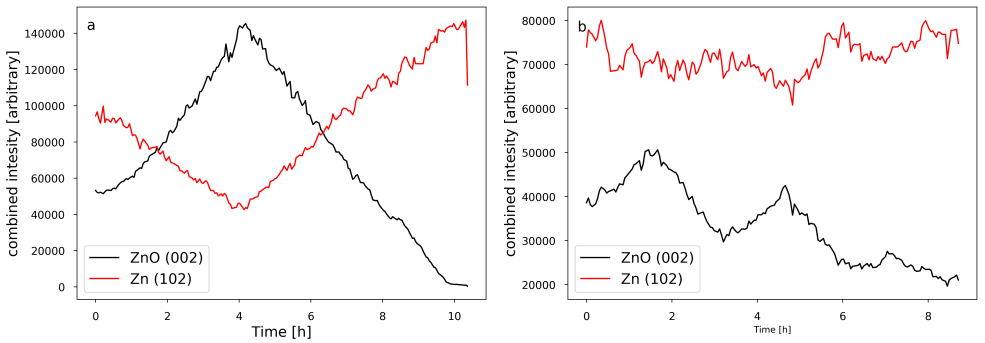

Figure 6.6: The development of the ZnO (002) peak Zn (102) reflection intensities along with cycling data for a) Zn1, b) Zn2 and c) Zn3

of the Zn is not electrically connected. For the same sample ZnO is largely unchained during discharge and quickly depletes during charge. For sample Zn2, there are clear signs of deposition of of ZnO in the initial discharge, while the amount of Zn decreases. In the following cycles the ZnO does not reappear in this interface, although Zn does. The intensities in the top four segments of sample Zn1, shown in Figure

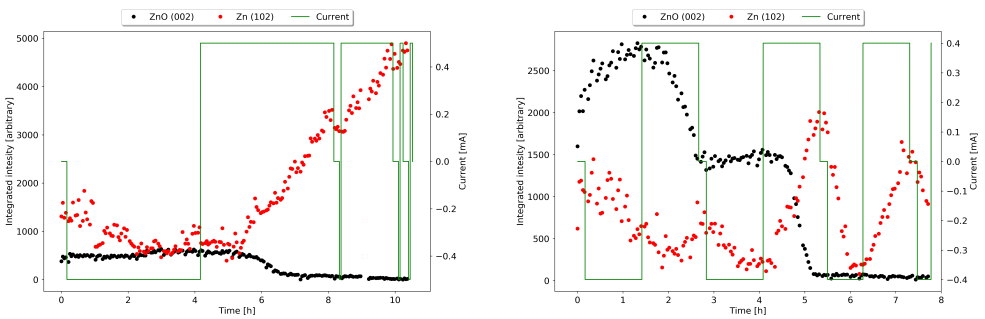

(a) The ZnO 002 and Zn 102 signal intensity over time at the anode electrode interface for sample Zn1 during cycling at 0.5 mA.

(b) The ZnO 002 and Zn 102 signal intensity over time at the anode electrode interface for sample Zn2 during cycling at 0.4 mA.

Figure 6.7: Intensities of Zn and ZnO in segment 1 of sample Zn1 and Zn2

6.8, suggests that also segment 2 in 6.8 a) is likely affected by a non flat interface with the electrolyte. The Zn and ZnO intensities are 1/3 of the other, deeper, segments, which could be due air bubbles or a very curved surface. Unlike the AEI in the segment above, Zn was entirely

depleted less than two hours into discharge, while the ZnO intensity increased slightly throughout the discharge. During charge, ZnO was depleted entirely in all of the displayed segments during the initial 4 hours of charging, with the higher segments being depleted earlier than lower segments. This indicates that the conversion of ZnO is a interface phenomenon that moves downward in the anode during charge. Zn is preferentially deposited at the top of the anode as segment 4 and 5 in Figure 6.8 c) an d) do not display a notable increase in Zn. During the final hours before the cell fails Zn is continuously deposited in the top of the anode even when no ZnO is present in these segments. The capacity of the Zn1 anode is 4.085 mAh, (Table 6.1) corresponding to a C-rate of 1/8 which during a 4 h discharge means that half of the Zn should be converted. This is consistent with the accumulated data in Figure 6.6 a). Following the 4 h of charge, the ratio of Zn to ZnO is shifted heavily in favour of Zn in the part of the anode. It is not immediately clear why the cell was unable to discharge after 4 h of charge. In the top part of the anode there is Zn available, likely deposited as a fine structure. A possibility is that the air cathode is compromised in its ability to perform the ORR reaction due to chocking or flooding. During a postmortem on XRD scan of the cathode, performed on in-house equipment, no Zn or ZnO was found in the Air-electrode as is reported by [74], but ZnO was found in the separator.

The capacity of the sample Zn2 was 3.75 mAh which at a current of 0.4 mA yields a C-rate of 1/9. This is comparable to Zn1 rate, but with the discharge reduced to 1 h and 15min the passed charge is reduced to 1/4 of the Zn1 sample. The intensities of Zn 002 and Zn 102 can be seen during cycling are shown in Figure 6.9 for the top 4 segments in beneath the AEI. Again, it appears that segment 2 contains less Zn and ZnO compared to deeper segments, presumably due to same reason as with sample Zn1. The shorter cycles results in less conversion of Zn, and as such the large crystallites are not are not significantly reduced in size for the Debye-Scherrer cones to become smooth in the way it did for the longer discharge. Because the Zn signal now, no longer necessarily represent the true amount of Zn. Additionally, due to the smaller charge passed the conversion did not proceed deeper into the sample results is that the Zn signal this is only easily understood in segment two, 6.9 a). The Zn was never fully depleted but was generally reduced in intensity, and by the end of the experiment it follows a sawtooth pattern exactly as should be expected. The intensity of ZnO in the same segment

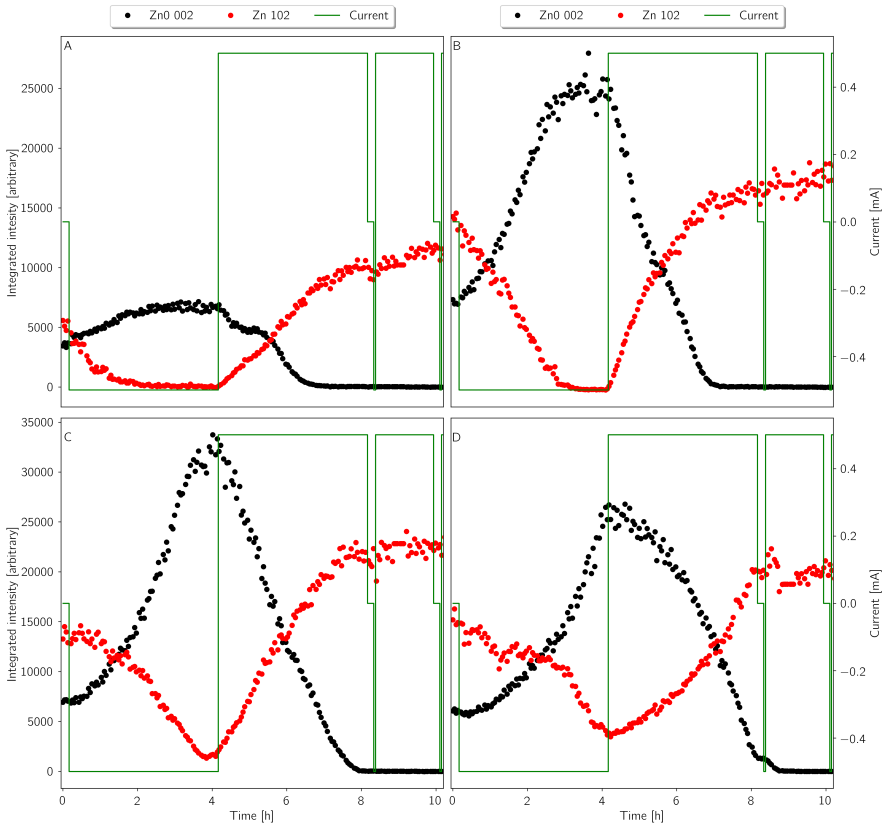

Figure 6.8: The intensity of Zn 102 and ZnO 002 for the top 4 segments of the anode in the Zn1 sample a) 0.2 mm below the AEI, b) 0.4 mm below the AEI, c) 0.6 mm below the AEI and d) 0.8 mm below the AEI during cycling.

was however, generally decreasing although it is clear it was deposited in each segment. In b and c), a sawtooth pattern is observed for Zn and the overall intensity increased slightly, while ZnO was generally depleted, although it is partially deposited during charge. In the segment between 0.6 and 0.8 mm into the anode, neither Zn nor ZnO appears to be significantly converted. As for the previously mentioned sample it is not obvious why the sample is unable to discharge after roughly 10 h, as there is a significant amount of Zn available. During the final charge of the Zn2 sample the charging plateau increasing and experiences noise which could suggest that the air-electrode is failing. An explanation could be that bubbles were formed in cathode which are unable to escape the electrode, which in turn reduces the area, which drives up the

potential. If the bubbles were trapped that would explain why there is some discharge capacity, but as the cathode is not functioning properly it cannot obtain more o_2 it, when these are consumed.

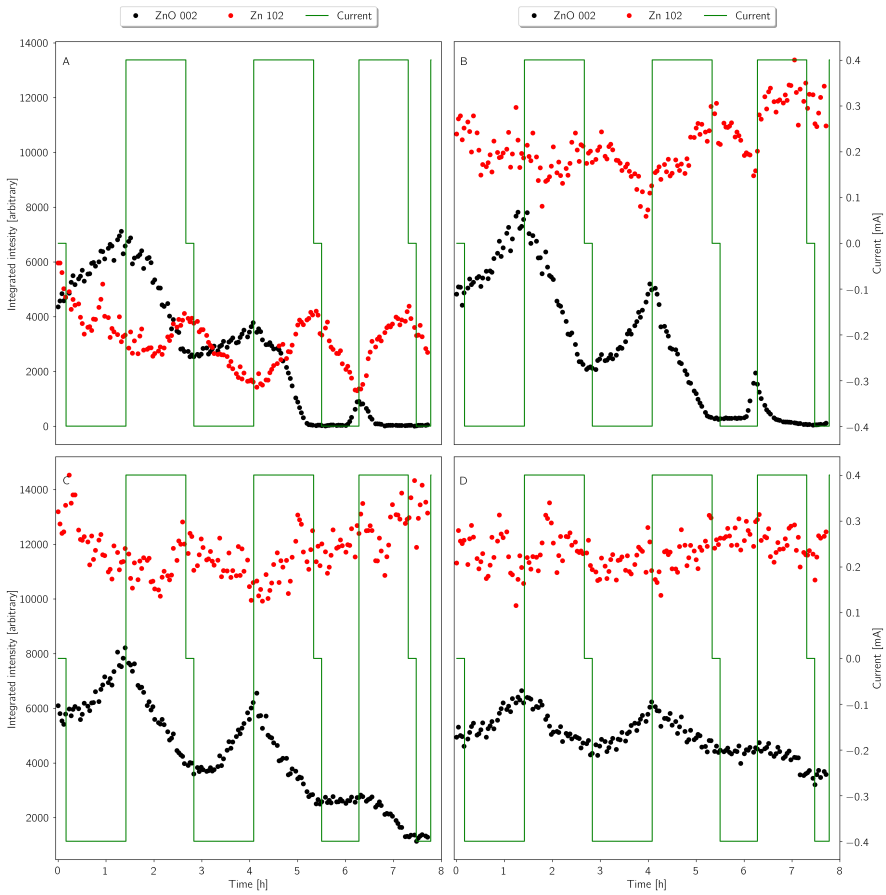

Figure 6.9: The intensity of Zn 102 and ZnO 002 for the top 4 segments of the anode a) 0.2 mm below the AEI b) 0.4 mm below the AEI c) 0.6 mm below the AEI and d) 0.8 mm below the AEI during 1 h and 15 min long cycles.

The third sample Zn3 had a capacity of 4 20mAh and was cycled for 1 h at a current of 0.25 mA, yielding the lowest C-rate applied of of 1/17. Due to experimental constraints, which are discussed later, this sample had 10 wt% mixed into its cathode. The electrochemical cycling is shown Figure 6.2 c), the first discharge plateau is 1.1 V which is en agreement what should be expected for Zn-air, but with increased cycling the discharge plateau decreases with each cycle and ultimately decreased to 0.6 V. The

charging plateau is entirely flat at approximately 2 V throughout the experiment.

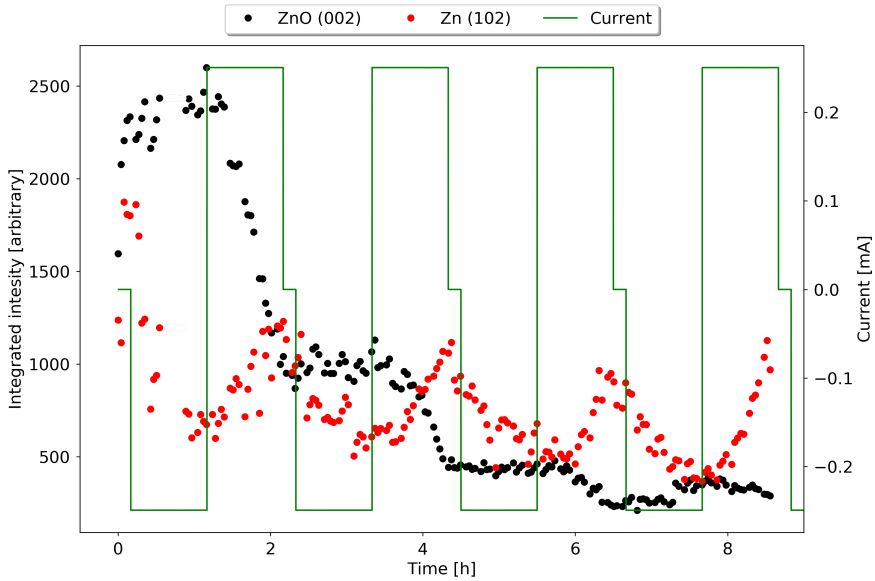

Figure 6.10: The intensity of Zn 102 and ZnO 002 for the top 4 segments of the anode a) 0.2 mm below the AEI b) 0.4 mm below the AEI c) 0.6 mm below the AEI and d) 0.8 mm below the AEI during 1 h and 15 min long cycles.

For sample Zn3 in the interface between the anode and the electrolyte 6.10 the conversion is significant due to the small amount of material here. While Zn does follow a sawtooth pattern it is clear that ZnO is quickly depleted and does not reapear in significant amounts. In the two segments below, segments 2-3, display a clear decrease in the ZnO intensity during charge and only slight increase during discharge, as shown in Figure 6.11 a) and b). In both these cases, the ZnO is almost entirely depleted throughout the four cycles. In the lower segments, figure 6.11 c) and d), the ZnO intensity generally decreased with time, which is consistent with the observation from the previous samples where deeper segments were less affected by the conversion. Conversion of Zn is most clearly observed in the top segment, while it is relatively constant in he other segments. As with the other samples, it is clearly seen that Zn and ZnO do not return to the same ratio as at the beginning of the cycling, but is changing in favour of the Zn.

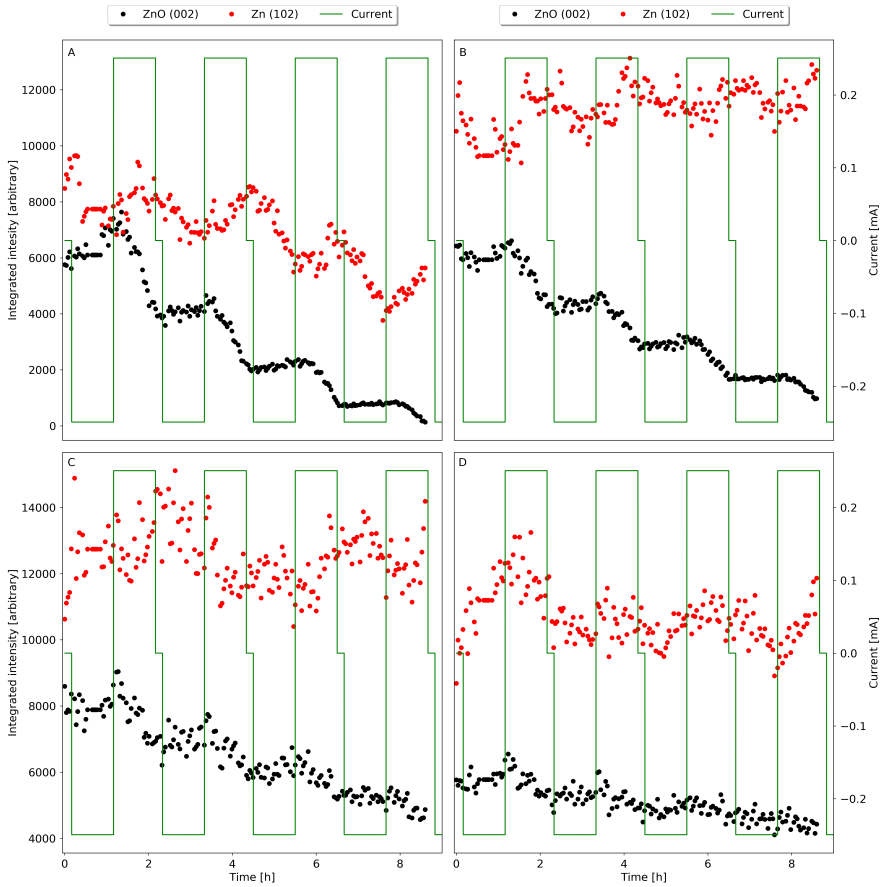

Figure 6.11: The intensity of Zn 102 and ZnO 002 for the top 4 segments of the anode In the Zn3 sample a) 0.2 mm below the AEI, b) 0.4 mm below the AEI, c) 0.6 mm below the AEI, and d) 0.8 mm below the AEI during 1 h long cycles.

6.2 Tomography

To further investigate the structure change in the anode during cycling the cell was adopted for tomography, which required contacting the air-electrode in a way that it an rotate along its length axis. The anode was contacted through the stage it was mounted in, while the cathode was connected via a 63 µm Cu thread attached via conductive silver epoxy. In this configuration tomograms where obtained over 52 minutes. Due to the length of each tomogram an hour of measuring the OCV was inserted between each charge and discharge to avoid overlap between tomograms.

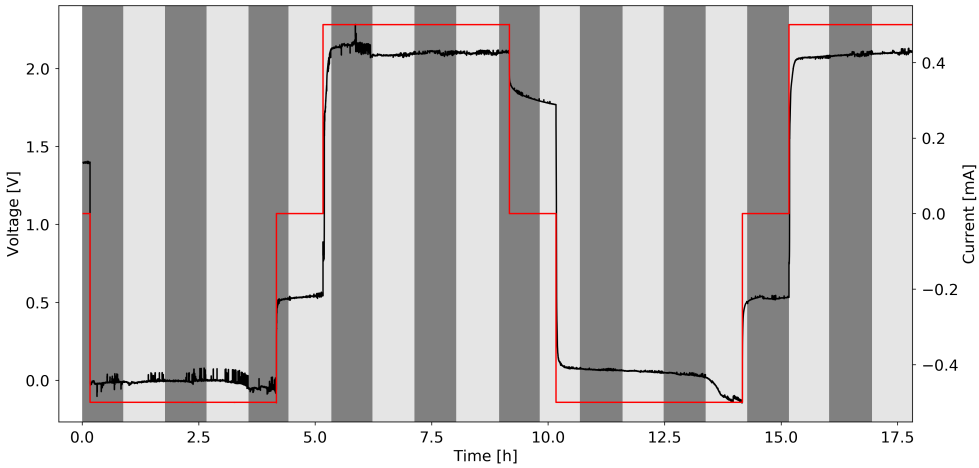

Figure 6.12: Electrochemical cycle data at 0.5 mA for a capillary cell during tomography. Each tomogram is indicated by alternating grey vertical bars.

In-skute X-ray μCT scans were conducted with an Xradia Versa XRM-410 instrument using a W reflection target. Scans were performed at a voltage of 140 kV, a power of 10 w, no filter, 4x optical magnification, binning 4, an exposure time of 1 s and a total of 1451 projections over a 186° rotation, resulting in a pixel resolution of 4.5 μm. The acquisition time of one tomogram was set to approximately 1 hour but in practice was only 52 minutes, and 20 tomograms were recorded successively without breaks in between. The recorded data was reconstructed using the Feldkamp-Davis-Kress reconstruction algorithm with a beam hardening constant of 0.05 and a smooth filter constant of 0.5. All the extracted images are obtained through Avizo Lite 9.5.0

All the resulting tomograms are shown in Figure 6.13. The contrast was inverted so that the densest material, Zn, appears white, while ZnO appears grey, and the reaming the dark voids are likely pockets of electrolyte or air bubbles, where the material content is very low. The cylinder in the bottom of each picture is the Cu-current collector that appears very identical to Zn due to their similar density. The first five tomograms a-e) were acquired during discharge, and it is clear that the Zn particles in the top part of the anode was entirely depleted of Zn particles and replaced in with dark spots. Further down the larger Zn particles remain after

the discharge ends, but are severely reduced in size. Here the conversion of Zn does not result in hollow spots.

Once the charge started in Figure 6.13 g) Zn was deposited at the interface between the previously hollow anode, with a lower brightness. Zn and ZnO are already close in density so if the Zn is deposited as fine particles, as the XRD data suggest, and porous structures it will appear closer to ZnO. Larger particles in the lower part of the anode only regrow slightly. Once the Second discharge starts in Figure 6.14 k) the entire anode starts to shrink as the entire top layer is depleted as Zn is converted, and no discernible redeposition of ZnO is observed. In the final three cros s sections, during charge, Zn is once again deposited in the top of the anode. But the with now even less ZnO in the structure. While the Zn does build up in the top of the anode it does not resemble the conventional depiction of dendrites as pointy elongated structures.

6.2.1 Discussion

The capillary batteries were assembled by hand, and therefore each cell will exhibit differences to each other. These differences include the length, or total mass of the anode and air-electrode, homogeneity of anode and cathode, alignment of the glass capillaries, and alignment of current collectors and contact. Furthermore, the cathode is very fragile and needs to be handled carefully when contacted. Finally, when assembling the cell, bubble formation needs to be avoided. Each cell was made from prefabricated cathode and anode assemblies, which only needed Zn/ZnO, electrolyte and separator to function. Each cell was assembled carefully and was rejected if the anode or cathode were damaged in any way. Despite these difficulties, the results herein are believed to accurately represent the processes occurring in a Zn-air, such as in conventional button cell, during discharge, or testing cells as seen in previous chapters of this thesis.

The results are also comparable to results obtained from several capillary cells tested on in-house equipment during the development of the cell. The XRD results from the three capillary cells presented herein represent a subset of 16 experiments that were conducted at the beam line, of which more than half were cycled at different currents, all supporting the conclusion is this section. The three experiments presented herein were selected from the obtained electrochemical data with highest quality that

still support each other without using identical cycle parameters. The three experiments each employed a different cathode mixture, which is due to the fragile nature of the cathode, despite preparing more than 120 cathodes (60 of which were NCO + 15 %wt PTFE) were prepared and inability to produce new cathode glass parts at the beamline.

Similarly for the tomography cell, with the addition of the Cu wire to the sample and Ni current collector, it is the author's opinion that the chemistry is representative of the real electrochemistry and the data herein is a subset of 3 experiments that all support the conclusions herein, even with the relatively high overpotential during discharge. From these observations, it is clear that a more robust cathode is a highly desired improvement for this cell architecture. This could likely be achieved by investigating different mixtures and preparation procedures of the catalyst slurry to obtain a less brittle composition. Another approach could be to coat the inside of the capillary with a conductive film, preferably Ni, by means of physical vapour deposition. A cathode like this could provide longer cycle life, which could more accurately elucidate the failure mode of the transformations seen in the experiments. This could also reduce the discharge overpotential observed in the tomography experiments to resemble the values observed in the other investigated cells. A further modification of these experiments would be to use finer and more uniform Zn powder, which would provide accurate Zn signal throughout the experiments and smaller conversion rates.

6.3 Summary of XRD and Tomography on Zn-air anodes

A functioning Zn-air capillary cell small enough for *in situ* characterisation using XRD and tomography was developed and employed. By tracking the intensity of ZnO 002 and Zn 102 peaks, the conversion of these materials was tracked and resolved, even when the Zn peaks do not exactly represent the amount, due to detector saturation. It was found that the conversion of Zn initially occurs closest to the separator and proceeds away from the this interface, in agreement with the findings of Arlt *et. al.* [73]. During charge, the Zn was preferentially deposited closer to the separator, and similarly to its counterpart, ZnO was also converted closest to the separator. ZnO did however not precipitate at the same rate as it was depleted, resulting in a different Zn/ZnO ratio than the

initial value, skewed toward Zn. This was revealed to be a consequence of ZnO entirely disappearing from the top layers and being found in the separator, as shown for experiments with a 50% DoD at C-rates of C1/8 and 12.5% DoD at an almost similar C-rate of C1/9. Even so, depletion of the anode was not clearly shown to be the reason for the failure of these cells, which is suspected to originate from the anode, possible due to flooding or a loose connection resulting from the way the anode is fixated.

Using a similar cell, quasi in situ tomography data was obtained with a time resolution of 52 minutes and pixel resolution of 4.5 µm. This cell worked for more than 20 h, despite having a high overpotential during discharge, which was likely related to the air electrode. Using this cell, it was shown that the interface was converted first during discharge and that Zn was preferentially deposited here, while ZnO was depleted over time. While the Zn is deposited at the top of the anode, it does not appear as dendrites, but rather in larger particles that could be porous.

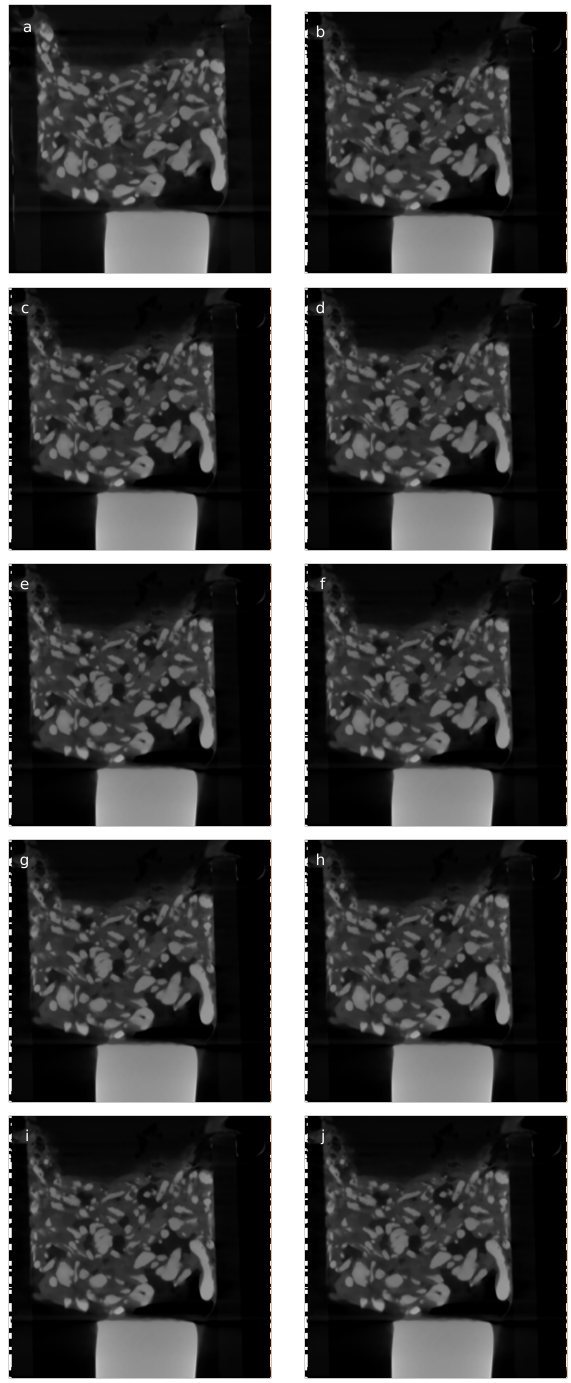

Figure 6.13: Cross section a-j) of a the Zn-air tomography battery anode during cycling.

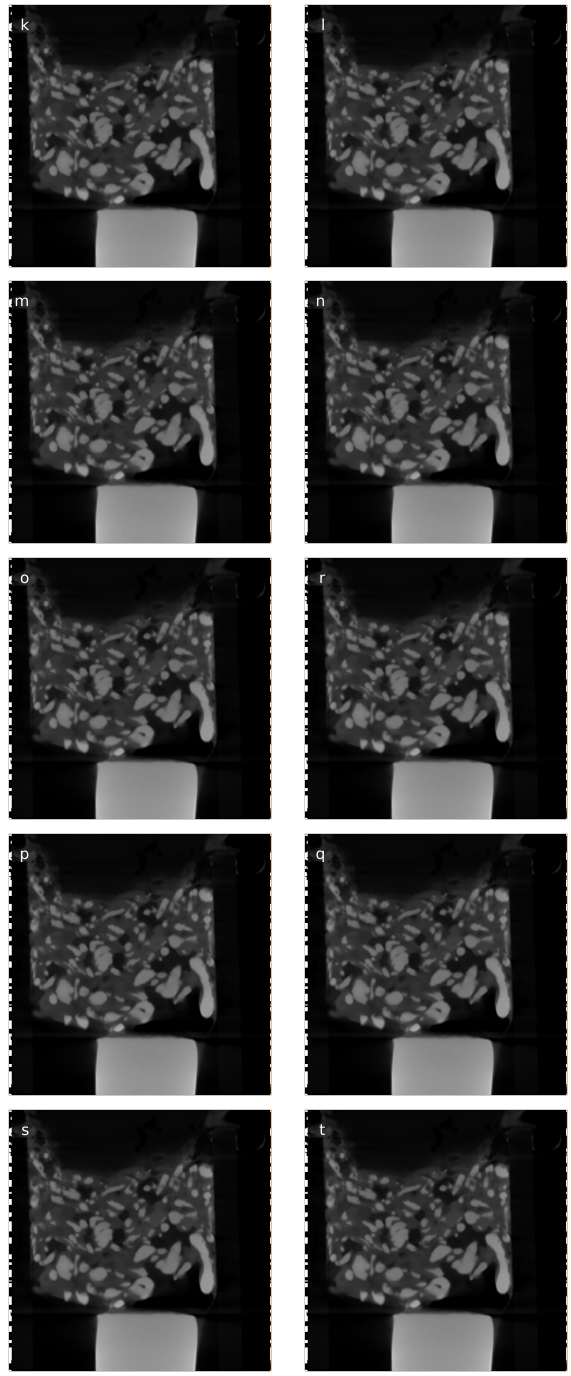

Figure 6.14: Cross section k-t) of the Zn-air tomography battery anode during cycling.

Chapter 7

Conclusion and Outlook

7.1 Summary of the Main Results

The aim of this project was to investigate the operation of Zn-air batteries using in situ techniques and determine how the fundamental mechanisms of these batteries affect cycle life and performance.

Materials that are commonly found as current collectors were tested for dissolution within the potential window of a Zn-air battery. This study showed that Ti, Cu, W and Sn were suited for the anode current collector, but only two, Ni and Ti, would be suitable for the cathode. It was demonstrated that stainless steel would not be stable for neither the anode nor cathode current collector. It was found that, while successful, the in situ ICP-OES flow cell setup needed improvement to gain better resolution with lower noise.

In alkaline Zn-air batteries the conversion of Zn to ZnO occurs through the soluble intermediate zincate, $Zn(OH)_4{}^{2-}$. During discharge, this intermediate is free to diffuse into the battery and deposit as ZnO in the separator as the solubility limit of the intermediate is reached. An anode will therefore over time preferentially deposit Zn in the interface between the anode and the separator. Adding ZnO can alleviate this problem somewhat, because it provides nucleation sites and saturates the solution with zincate. Having developed a Zn-air capillary battery with such an anode, and by using time and spatially resolved synchrotron XRD, it was proven that initially ZnO is indeed deposited in the anode. Dur-

ing charging, however, more ZnO was converted back to Zn than was produced during discharge, skewing the ratio in favour of Zn. Using the spatial resolution of this cell, it was shown that this effect was exacerbated because the Zn/ZnO ratio would be skewed in favour of the Zn closer to the separator. This was confirmed to be true for 3 DoDs and at two very different C-rates. It was suggested that during long term cycling this effect would significantly alter the structure of the anode. Which could compromise the battery performance.

Using the DEMS setup, a neutral, a slightly alkaline $ZnCl_2$ and a highly alkaline electrolyte with additives were investigated. It was found that the neutral and $ZnCl_2$ electrolytes despite cycling did not evolve O_2, they did however develop significant amounts of H_2. A neutral electrolyte with very high content of Li(TFSI) and $Zn(TFSI)_2$ was investigated, and was found not to develop O_2, likely due to intercalation of Li into the cathode. By applying the same technique for a Zn-air battery with an alkaline electrolyte, the n_{e^-/O_2} ratio was determined, and it was found that accounting for the H_2 evolution from the battery is essential to get accurate measurements. It was also suggested that using static measurements for H_2 evolution will lose its efficacy over time, likely due to changing area during cycling. Finally, an alkaline electrolyte with the additives KF and K_2CO_3 was found to reduce the severity of H_2 evolution with a very ideal n_{e^-/O_2} ratio, once corrected for H_2.

By applying DEMS on Zn-air batteries with dopants, the effect of dopants was investigated and compared to DFT results. The experiments and DFT models demonstrated that In and Bi each affect the battery, with In limiting hydrogen evolution while Bi would benefit the battery by optimising the potential characteristics. It was shown how these dopants are useful in secondary Zn-air batteries, as they would be able to stay at the surface during Zn-plating due to the materials favouring the kink sites at the Zn surface. By co-doping Zn with both In and Bi, their beneficial effect were compounded and led to consistently low H_2 evolution. It was shown that Ag was detrimental to the battery, as it would amplify the HER, and at the same time Ag would be buried during Zn plating because it favours higher coordinated sites. Finally, it was shown how a commercial Zn powder with these dopants, among others, had consistent low H_2 evolution.

7.2 Outlook

To achieve fully rechargeable Zn-air batteries, self corrosion needs to be entirely mitigated. Not only does it interfere with the electrical efficiency of the battery, it also depletes the electrolyte, which increases the need for water management in a system that already gives off water. Better understanding of the Zn surface by modeling and confirmation by experimental techniques could help reduce this effect even further by suggesting new additives, co-doping, optimal dosage and methods in which to apply them. Another option could be moving to more neutral electrolytes, with a system that has high ionic conductivity and low solubility of intermediate species, which would increase ZnO precipitation. Additives to KOH which show promise need to be investigated for long term detrimental effects.

Another important feature is to develop an anode that allows deep discharges, while being able retain a structure that ensures homogeneous deposition of Zn and ZnO. By developing tools such as the capillary cells even further, it would be possible to investigate the changes in different anode structures at high cycle numbers. This could be done through determining a optimal way cycle Zn-air batteries to avoid inhomogenous deposition of Zn-air. Perhaps charging the battery slower or in a pulsed produce to allow the internal concentration gradients time to even out. Additionally, by improving this cell, the cathode and its long term degradation could be investigated by tracking the wetting and oxidation/reduction cycle experienced air electrode, as seen with the $NiCo_2O_4$ and Ni cathode.

Bibliography

[1] IPCC. IPCC special report on the impacts of global warming of 1.5 °C - Summary for policy makers. (October 2018), 2018.

[2] Thomas R. Anderson, Ed Hawkins, and Philip D. Jones. Co2, the greenhouse effect and global warming: from the pioneering work of arrhenius and callendar to today's earth system models. *Endeavour*, 40(3):178 – 187, 2016.

[3] IEA Internation Energy Agency. Global energy & co2 status report. Technical report, IEA, 2017.

[4] Nathan S. Lewis and Daniel G. Nocera. Powering the planet: Chemical challenges in solar energy utilization. *Proceedings of the National Academy of Sciences*, 103(43):15729–15735, 2006.

[5] IEA Internation Energy Agency. World energy outlook 2017. Technical report, IEA, 2017.

[6] NREL. HAWAII SOLAR INTEGRATION STUDY : Executive Summary.

[7] Energikommissiones anbefalninger til fremtiden energipolitik, 2017.

[8] Mathew Aneke and Meihong Wang. Energy storage technologies and real life applications – a state of the art review. *Applied Energy*, 179:350 – 377, 2016.

[9] Bruce Dunn, Haresh Kamath, and Jean-Marie Tarascon. Electrical energy storage for the grid: A battery of choices. *Science*, 334(6058):928–935, 2011.

[10] Andrew Ulvestad. A Brief Review of Current Lithium Ion Battery Technology and Potential Solid State Battery Technologies. *eprint ArXiv*, page https://arxiv.org/pdf/1803.04317.pdf, 2018.

[11] Thomas B. Reddy David Linden. *Handbook of Batteries*. McGraw-Hill, 2001.

[12] George E. Blomgren. The development and future of lithium ion batteries. *Journal of The Electrochemical Society*, 164(1):A5019–A5025, 2017.

[13] IEA Internation Energy Agency. Electric and plug-in hybrid electric vehicles. Technical report, IEA, 2011.

[14] G W Heise. Aug. 29, 1933. 1933.

[15] G. Girishkumar, B. McCloskey, A. C. Luntz, S. Swanson, and W. Wilcke. Lithium-air battery: Promise and challenges. *The Journal of Physical Chemistry Letters*, 1(14):2193–2203, 2010.

[16] Tejs Vegge, Juan Maria Garcia-Lastra, and Donald J. Siegel. Lithium–oxygen batteries: At a crossroads? *Current Opinion in Electrochemistry*, 6(1):100 – 107, 2017.

[17] Jake Christensen, Paul Albertus, Roel S. Sanchez-Carrera, Timm Lohmann, Boris Kozinsky, Ralf Liedtke, Jasim Ahmed, and Aleksandar Kojic. A critical review of li/air batteries. *Journal of The Electrochemical Society*, 159(2):R1–R30, 2011.

[18] Kevin G. Gallagher, Steven Goebel, Thomas Greszler, Mark Mathias, Wolfgang Oelerich, Damla Eroglu, and Venkat Srinivasan. Quantifying the promise of lithium–air batteries for electric vehicles. *Energy Environ. Sci.*, 7:1555–1563, 2014.

[19] Yanguang Li and Jun Lu. Metal–air batteries: Will they be the future electrochemical energy storage device of choice? *ACS Energy Letters*, 2(6):1370–1377, 2017.

[20] E. Davari and D. G. Ivey. Bifunctional electrocatalysts for zn–air batteries. *Sustainable Energy Fuels*, 2:39–67, 2018.

[21] Peter C K Vesborg and Thomas F. Jaramillo. Addressing the terawatt challenge: Scalability in the supply of chemical elements for renewable energy. *RSC Advances*, 2(21):7933–7947, 2012.

[22] Prabal Sapkota and Honggon Kim. Zinc–air fuel cell, a potential candidate for alternative energy. *Journal of Industrial and Engineering Chemistry*, 15(4):445 – 450, 2009.

[23] J. Hojberg, K. B. Knudsen, J. Hjelm, and T. Vegge. Reactions and SEI Formation during Charging of Li-O2 Cells. *ECS Electrochemistry Letters*, 4(7):A63–A66, 2015.

[24] Jonathan Højberg, Tejs Vegge, Poul Norby, and Keld Johansen. Fundamental mechanisms in li-air battery electrochemistry, 2015.

[25] B. D. McCloskey, D. S. Bethune, R. M. Shelby, G. Girishkumar, and A. C. Luntz. Solvents critical role in nonaqueous Lithium-Oxygen battery electrochemistry. *Journal of Physical Chemistry Letters*, 2(10):1161–1166, 2011.

[26] Noémie Elgrishi, Kelley J. Rountree, Brian D. McCarthy, Eric S. Rountree, Thomas T. Eisenhart, and Jillian L. Dempsey. A practical beginner's guide to cyclic voltammetry. *Journal of Chemical Education*, 95(2):197–206, 2018.

[27] Stanley Bruckenstein and R. Rao Gadde. Use of a porous electrode for in situ mass spectrometric determination of volatile electrode reaction products. *Journal of the American Chemical Society*, 93(3):793–794, 1971.

[28] O. Wolter and J. Heitbaum. Differential electrochemical mass spectroscopy (dems) — a new method for the study of electrode processes. *Berichte der Bunsengesellschaft für physikalische Chemie*, 88(1):2–6, 1984.

[29] ZAS consorstium. Zinc air secondary innovative nanotech based batteries for efficient energy storage. Technical report, HORIZON2020, 2015.

[30] Patrick Bonnick and J. R. Dahn. A simple coin cell design for testing rechargeable zinc-air or alkaline battery systems. *Journal of The Electrochemical Society*, 159(7):A981–A989, 2012.

[31] Joseph F. Parker, Christopher N. Chervin, Irina R. Pala, Meinrad Machler, Michael F. Burz, Jeffrey W. Long, and Debra R. Rolison. Rechargeable nickel–3d zinc batteries: An energy-dense, safer alternative to lithium-ion. *Science*, 356(6336):415–418, 2017.

[32] Ze Ma, Pucheng Pei, Keliang Wang, Xizhong Wang, Huachi Xu, Yongfeng Liu, and Guanlin peng. Degradation characteristics of air cathode in zinc air fuel cells. *Journal of Power Sources*, 274:56 – 64, 2015.

[33] D. Kundu, B. D. Adams, V. Duffort, S. H. Vajargah, and L. F. Nazar. A high-capacity and long-life aqueous rechargeable zinc battery using a metal oxide intercalation cathode. *Nature Energy*, 1:16119, October 2016.

[34] Qingfang Shi, Louis J. Rendek, Wen-Bin Cai, and Daniel A. Scherson. In situ raman spectroscopy of single particle microelectrodes: Zinc passivation in alkaline electrolytes. *Electrochemical and Solid-State Letters*, 6(11):E35–E39, 2003.

[35] Qingfang Shi, Louis J. Rendek, Wen-Bin Cai, and Daniel A. Scherson. Avoiding short circuits from zinc metal dendrites in anode by backside-plating configuration. 7(11801), 2016.

[36] Zhao Yan, Erdong Wang, Luhua Jiang, and Gongquan Sun. Superior cycling stability and high rate capability of three-dimensional zn/cu foam electrodes for zinc-based alkaline batteries. *RSC Adv.*, 5:83781–83787, 2015.

[37] D. C. W. Kannangara and B. E. Conway. Zinc oxidation and redeposition processes in aqueous alkali and carbonate solutions: I . ph and carbonate ion effects in film formation and dissolution. *Journal of The Electrochemical Society*, 134(4):894–906, 1987.

[38] K. Ogle and S. Weber. Anodic dissolution of 304 stainless steel using atomic emission spectroelectrochemistry. *Journal of the Electrochemical Society*, 147(5):1770–1780, 2000. cited By 71.

[39] K. Ogle, J. Baeyens, J. Swiatowska, and P. Volovitch. Atomic emission spectroelectrochemistry applied to dealloying phenomena: I. the formation and dissolution of residual copper films on stainless steel. *Electrochimica Acta*, 54(22):5163 – 5170, 2009. ELECTROCHEMISTRY DOWN TO THE MOLECULAR LEVEL INTERFACIAL SCIENCE FOR LIFE AND TECHNOLOGY Selection of papers from the 59th Annual Meetingof the International Society of Electrochemistry7-12 September 2008, Seville, Spain.

[40] B. Miller. Split-ring disk study of the anodic processes at a copper electrode in alkaline solution. *Journal of The Electrochemical Society*, 116(12):1675–1680, 1969.

[41] Chong-Hong Pyun and Su-Moon Park. In situ spectroelectrochemical studies on anodic oxidation of copper in alkaline solution. *Journal of The Electrochemical Society*, 133(10):2024–2030, 1986.

[42] T. Tuvić, I. Pašti, and S. Mentus. Tungsten electrochemistry in alkaline solutions—anodic dissolution and oxygen reduction reaction. *Russian Journal of Physical Chemistry A*, 85(13):2399–2405, Dec 2011.

[43] G. Stephen Kelsey. The anodic oxidation of tungsten in aqueous base. *Journal of The Electrochemical Society*, 124(6):814–819, 1977.

[44] D. Kwaśniewski and M. Grdeń. Electrochemical behaviour of tin in alkaline electrolyte. *Electrochemistry Communications*, 61:125 – 128, 2015.

[45] Jianqiang Kang, Yifu Yang, Fengshan Jiang, and Huixia Shao. Study on the anodic reaction of ni in an alkaline solution by transient ph detection based on scanning electrochemical microscopy (secm). *Surface and Interface Analysis*, 39(11):877–884.

[46] Anna K. Schuppert, Angel A. Topalov, Ioannis Katsounaros, Sebastian O. Klemm, and Karl J. J. Mayrhofer. A scanning flow cell system for fully automated screening of electrocatalyst materials. *Journal of The Electrochemical Society*, 159(11):F670–F675, 2012.

[47] Yanguang Li and Hongjie Dai. Recent advances in Zinc-air batteries. *Chemical Society Reviews*, 43(15):5257–5275, 2014.

[48] Johannes Stamm, Alberto Varzi, Arnulf Latz, and Birger Horstmann. Modeling nucleation and growth of zinc oxide during discharge of primary zinc-air batteries. *Journal of Power Sources*, 360:136–149, 2017.

[49] Daniel Schröder, Neeraj Nitin Sinai Borker, Michael König, and Ulrike Krewer. Performance of zinc air batteries with addedk2co3in the alkaline electrolyte. *Journal of Applied Electrochemistry*, 45(5):427–437, May 2015.

[50] Lars Kucka, Eugeny Y. Kenig, and Andrzej Górak. Kinetics of the gas-liquid reaction between carbon dioxide and hydroxide ions. *Industrial & Engineering Chemistry Research*, 41(24):5952–5957, 2002.

[51] T. C. Adler, F. R. McLarnon, and E. J. Cairns. Investigations of a new family of alkaline-fluoride-carbonate electrolytes for zinc/nickel oxide cells. *Industrial & Engineering Chemistry Research*, 37(8):3237–3241, 1998.

[52] Fei Wang, Oleg Borodin, Tao Gao, Xiulin Fan, Wei Sun, Fudong Han, Antonio Faraone, Joseph A. Dura, Kang Xu, and Chunsheng Wang. Highly reversible zinc metal anode for aqueous batteries. *Nature Materials*, 17(6):543–549, 2018.

[53] Afriyanti Sumboja, Xiaoming Ge, Guangyuan Zheng, F. W.Thomas Goh, T. S.Andy Hor, Yun Zong, and Zhaolin Liu. Durable rechargeable zinc-air batteries with neutral electrolyte and manganese oxide catalyst. *Journal of Power Sources*, 332:330–336, 2016.

[54] F. W. Thomas Goh, Z. Liu, T. S. A. Hor, J. Zhang, X. Ge, Y. Zong, A. Yu, and W. Khoo. A Near-Neutral Chloride Electrolyte for Electrically Rechargeable Zinc-Air Batteries. *Journal of the Electrochemical Society*, 161(14):A2080–A2086, 2014.

[55] Simon Clark, Arnulf Latz, and Birger Horstmann. Rational Development of Neutral Aqueous Electrolytes for Zinc–Air Batteries. *ChemSusChem*, 10(23):4735–4747, 2017.

[56] Fei Wang, Oleg Borodin, Tao Gao, Xiulin Fan, Wei Sun, Fudong Han, Antonio Faraone, Joseph A. Dura, Kang Xu, and Chunsheng Wang. Highly reversible zinc metal anode for aqueous batteries. *Nature Materials*, 17(6):543–549, 2018.

[57] L M BAUGH, F L TYE, and N C WHITE. Corrosion and Polarization Characteristics of Zinc in Battery Electrolyte Analogs and the Effect of Amalgamation. *Journal of Applied Electrochemistry*, 13(5):623–635, 1983.

[58] Marcel L. Meeus IvanA. J. Strauven. Horst-udo dipl ing josegerd dipl chem jung (varta batterie ag), 1989.

[59] Marcel L. Meeus (Union Miniere) IvanA. J. Strauven. Zn-powder for alkaline batteries, 1994.

[60] J. Dutkiewicz and W. Zakulski. The in-zn (indium-zinc) system. *Bulletin of Alloy Phase Diagrams*, 5(3):284–289, Jun 1984.

[61] A. G. Muoz, S. B. Saidman, and J. B. Bessone. Influence of In on the corrosion of Zn-In alloys. *Corrosion Science*, 43(7):1245–1265, 2001.

[62] Chang Woo Lee, K. Sathiyanarayanan, Seung Wook Eom, and Mun Soo Yun. Novel alloys to improve the electrochemical behavior of zinc anodes for zinc/air battery. *Journal of Power Sources*, 160(2):1436 – 1441, 2006. Special issue including selected papers presented at the International Workshop on Molten Carbonate Fuel Cells and Related Science and Technology 2005 together with regular papers.

[63] Jiri Vizdal, Maria Helena Braga, Ales Kroupa, Klaus W. Richter, Delfim Soares, Luís Filipe Malheiros, and Jorge Ferreira. Thermodynamic assessment of the bi–sn–zn system. *Calphad*, 31(4):438 – 448, 2007.

[64] Roger Shepard (Gillette) Lifun Lin. Zinc/air cell, 2001.

[65] Yichun Wang Joseph E. Sunstrom In Tae Bae (Gillette) Cahit Eylem, Paul A. Christian. Primary alkaline battery containing bismuth metal oxide, 2008.

[66] M. Y. Chiu, S. S. Wang, and T. H. Chuang. Intermetallic compounds formed during interfacial reactions between liquid sn-8zn-3bi solders and ni substrates. *Journal of Electronic Materials*, 31(5):494–499, May 2002.

[67] J. McBreen and E. Gannon. Bismuth oxide as an additive in pasted zinc electrodes. *Journal of Power Sources*, 15(2):169 – 177, 1985.

[68] C. Zhang, J.M. Wang, L. Zhang, J.Q. Zhang, and C.N. Cao. Study of the performance of secondary alkaline pasted zinc electrodes. *Journal of Applied Electrochemistry*, 31(9):1049–1054, Sep 2001.

[69] Samira Siahrostami, Vladimir Tripković, Keld T. Lundgaard, Kristian E. Jensen, Heine A. Hansen, Jens S. Hummelshøj, Jón S.G. Mýrdal, Tejs Vegge, Jens K. Nørskov, and Jan Rossmeisl. First principles investigation of zinc-anode dissolution in zinc-air batteries. *Physical Chemistry Chemical Physics*, 15(17):6416–6421, 2013.

[70] Dennis Wittmaier, Natalia A. Cañas, Indro Biswas, and Kaspar Andreas Friedrich. Highly stable carbon-free ag/co3o4-cathodes for

lithium-air batteries: Electrochemical and structural investigations. *Advanced Energy Materials*, 5(19):1500763.

[71] Quinn C. Horn and Yang Shao-Horn. Morphology and Spatial Distribution of ZnO Formed in Discharged Alkaline Zn/MnO[sub 2] AA Cells. *Journal of The Electrochemical Society*, 150(5):A652, 2003.

[72] Daniel Schröder, Tobias Arlt, Ulrike Krewer, and Ingo Manke. Analyzing transport paths in the air electrode of a zinc air battery using X-ray tomography. *Electrochemistry Communications*, 40:88–91, 2014.

[73] Tobias Arlt, Daniel Schröder, Ulrike Krewer, and Ingo Manke. In operando monitoring of the state of charge and species distribution in zinc air batteries using X-ray tomography and model-based simulations. *Physical Chemistry Chemical Physics*, 16(40):22273–22280, 2014.

[74] Robert Franke-Lang, Tobias Arlt, Ingo Manke, and Julia Kowal. X-ray tomography as a powerful method for zinc-air battery research. *Journal of Power Sources*, 370:45–51, 2017.

[75] Akiyoshi Nakata, Haruno Murayama, Katsutoshi Fukuda, Tomokazu Yamane, Hajime Arai, Toshiro Hirai, Yoshiharu Uchimoto, Jun Ichi Yamaki, and Zempachi Ogumi. Transformation of leaf-like zinc dendrite in oxidation and reduction cycle. *Electrochimica Acta*, 166:82–87, 2015.

[76] Akiyoshi Nakata, Hajime Arai, Haruno Murayama, Katsutoshi Fukuda, Tomokazu Yamane, Toshiro Hirai, Yoshiharu Uchimoto, Jun Ichi Yamaki, and Zempachi Ogumi. In situ Zn/ZnO mapping elucidating for "shape change" of zinc electrode. *APL Materials*, 6(4), 2018.

[77] Aroa R Mainar, Elena Iruin, and Luis C Colmenares. *Systematic cycle life assessment of a secondary zinc - air battery as a function of the alkaline electrolyte composition Keywords.*

[78] Ann-Christin Dippel, Hanns-Peter Liermann, Jan Torben Delitz, Peter Walter, Horst Schulte-Schrepping, Oliver H. Seeck, and Hermann Franz. Beamline P02.1 at PETRA III for high-resolution and high-energy powder diffraction. *Journal of Synchrotron Radiation*, 22(3):675–687, May 2015.

[79] Mark Basham, Jacob Filik, Michael T. Wharmby, Peter C.Y. Chang, Baha El Kassaby, Matthew Gerring, Jun Aishima, Karl Levik, Bill C.A. Pulford, Irakli Sikharulidze, Duncan Sneddon, Matthew Webber, Sarnjeet S. Dhesi, Francesco Maccherozzi, Olof Svensson, Sandor Brockhauser, Gabor Náray, and Alun W. Ashton. Data Analysis WorkbeNch (DAWN). *Journal of Synchrotron Radiation*, 22:853–858, 2015.

[80] J. Filik, A. W. Ashton, P. C.Y. Chang, P. A. Chater, S. J. Day, M. Drakopoulos, M. W. Gerring, M. L. Hart, O. V. Magdysyuk, S. Michalik, A. Smith, C. C. Tang, N. J. Terrill, M. T. Wharmby, and H. Wilhelm. Processing two-dimensional X-ray diffraction and small-angle scattering data in DAWN 2. *Journal of Applied Crystallography*, 50(3):959–966, 2017.

Chapter 8

Appendix

8.1 Calibration of the Mass Spectrometer

In the present document we relay heavily on the quantitative measurement by the mass spectrometer that is employed in the DEMS. This equipment requires careful calibration using calibration gasses with know quantities. A mixture of 5 % O_2 and 5% CO_2 in 90 % Ar was used for this purpose. The process is well described by ref[24], and the intent of here is just to add this procedure and explain some of the underlying assumptions. Mass spectrometers are very sensitive towards changes in operation and it is recommended that they are always left on when not in use. Even so they cannot be expected to maintain constant sensitivity. For instance over a period of two months where the mass spectrometer was not being used the correction factor for O_2 drifted by 0.133. Therefore it is recommend to calibrate mass spectrometers as often as possible. In this document this process has been entirely hidden from the reader, but was performed about once per month or if the mass spec underwent power cycling due to maintenance or power cuts.

8.2 XRD - appendix

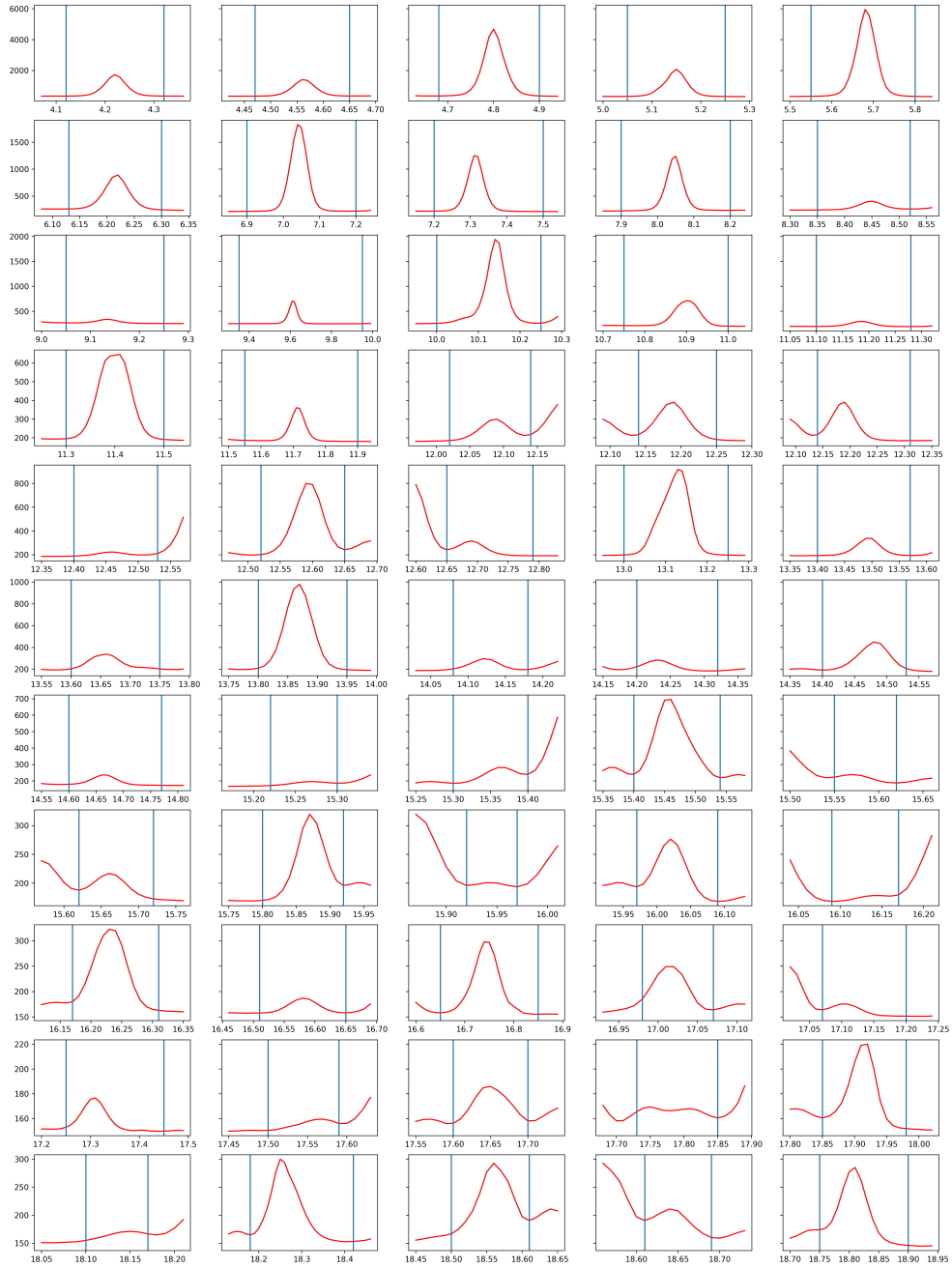

Figure 8.1: All reflections obtained from the from a single detector images in segment 2 for sample Zn3. The blue lines indicate the range in which the peak was integrated

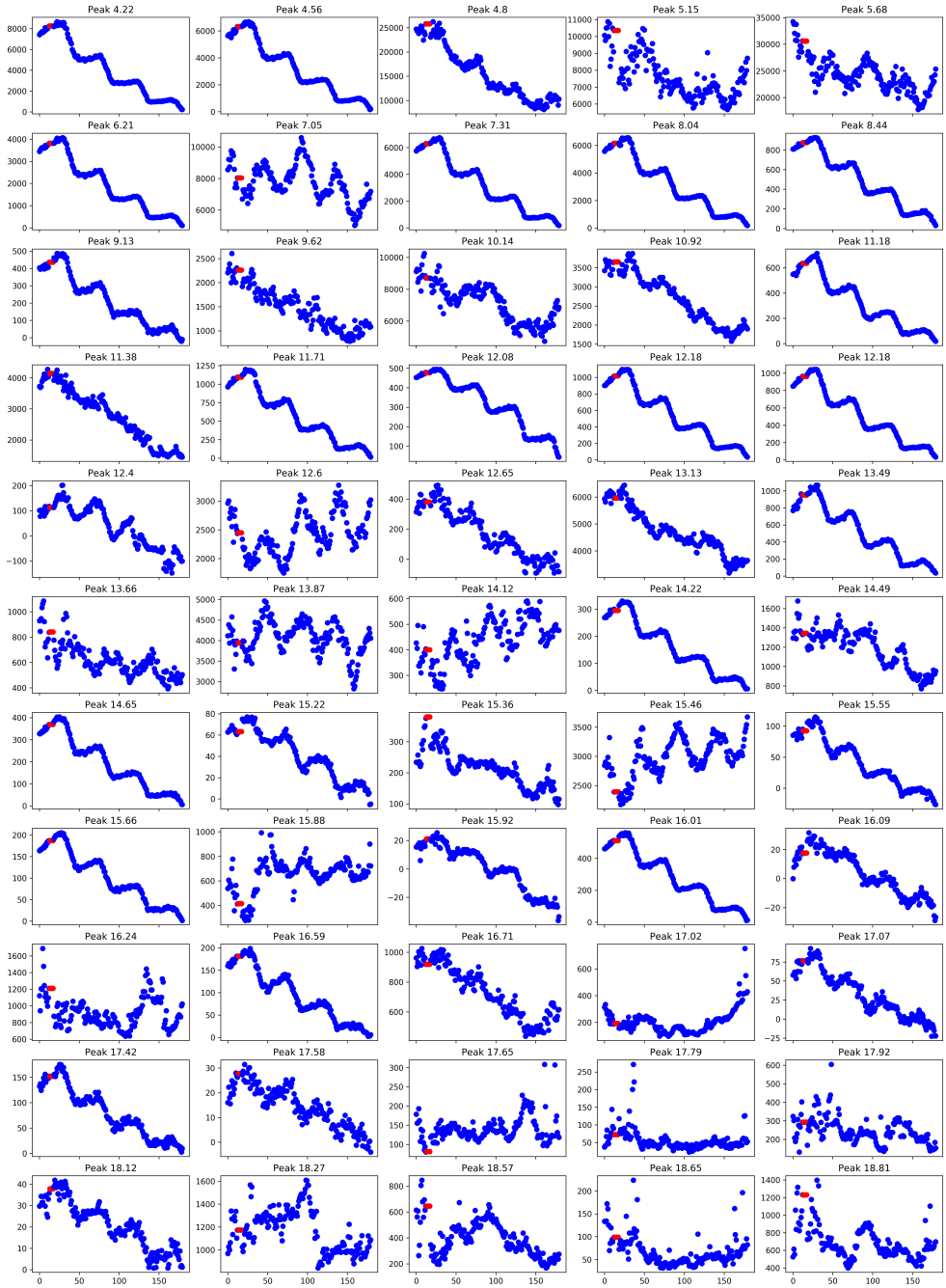

Figure 8.2: The evolution of all the peaks identified in segment 2 for sample Zn3 over time. Red data indicates placeholder data due to a dark image correction error.

Paper I

ChemPubSoc Europe

DOI: 10.1002/cssc.201800225

CHEMSUSCHEM Full Papers

Combined DFT and Differential Electrochemical Mass Spectrometry Investigation of the Effect of Dopants in Secondary Zinc–Air Batteries

Steen Lysgaard,* Mathias K. Christensen, Heine A. Hansen, Juan Maria García Lastra, Poul Norby, and Tejs Vegge*[a]

Zinc–air batteries offer the potential of low-cost energy storage with high specific energy, but at present secondary Zn–air batteries suffer from poor cyclability. To develop economically viable secondary Zn–air batteries, several properties need to be improved: choking of the cathode, catalyzing the oxygen evolution and reduction reactions, limiting dendrite formation and suppressing the hydrogen evolution reaction (HER). Understanding and alleviating HER at the negative electrode in a secondary Zn–air battery is a substantial challenge, for which it is necessary to combine computational and experimental research. Here, we combine differential electrochemical mass spectrometry (DEMS) and density functional theory (DFT) calculations to investigate the fundamental role and stability when cycling in the presence of selected beneficial additives, that is, In and Bi, and Ag as a potentially unfavorable additive. We show that both In and Bi have the desired property for a secondary battery, that is, upon recharging they will remain on the surface, thereby retaining the beneficial effects on Zn dissolution and suppression of HER. This is confirmed by DEMS, where it is observed that In reduces HER and Bi affects the discharge potential beneficially compared to a battery without additives. Using a simple procedure based on adsorption energies calculated with DFT, it is found that Ag suppresses OH adsorption, but, unlike In and Bi, it does not hinder HER. Finally, it is shown that mixing In and Bi is beneficial compared to the additives by themselves as it improves the electrochemical performance and cyclic stability of the secondary Zn–air battery.

Introduction

Today's challenge of transforming society from fossil fuel-based into one that is based on renewable energy requires the advent of more efficient and reliable energy storage media, both for transportation and to balance fluctuating clean energy sources such as wind and solar power. To this end, multiple technologies are currently under consideration, and secondary batteries are currently receiving a large amount of attention, primarily because of the widely successful Li-ion battery.[1] For large-scale storage, other battery types such as redox flow and metal–air batteries also hold promise.[2–4]

The commercially most successful metal–air battery is the primary Zn–air battery, widely used for small appliances that require a small amount of power for longer durations such as hearing aids. Zn–air batteries are attractive alternatives owing to the benign chemistry and high theoretical specific energy of 1086 Wh kg^{-1}, much higher than that of Li-ion batteries and only rivalled by few other chemistries such as Li–air,[5–8] The theoretical specific energy includes only the weight of Zn and the theoretical voltage. For practical purposes, the specific energy attainable in a typical Zn–air hearing-aid battery is currently 350–500 Wh kg^{-1},[9] which is approximately double of what is currently possible with Li-ion technology. For a secondary Zn–air battery the specific energy is lower because of restrictions with regard to the level of charge and discharge of the Zn electrode.[10] Rechargeable Zn–air batteries are especially promising for stationary storage of electricity because of its abundance in the earth crust and availability of Zn.[11]

In an alkaline Zn–air battery, reduction of oxygen to hydroxyl takes place at the cathode during discharge. The hydroxyl ions in the electrolyte then participate in the main reactions on the negative Zn electrode, which are:

$$Zn + 4\,OH^- \rightleftharpoons Zn(OH) + 3\,OH^- + e^- \rightleftharpoons Zn(OH)_2 + 2\,OH^- + 2\,e^- \quad (1)$$

$$Zn(OH)_2 + 2\,OH^- + 2\,e^- \rightleftharpoons [Zn(OH)_3]^- + OH^- + 2\,e^- \rightleftharpoons [Zn(OH)_4]^{2-} + 2\,e^- \quad (2)$$

The first two OH adsorption steps [Eq. (1)] are the electrochemical formation of zinc hydroxide ($Zn(OH)_2$), whereas the last two steps [Eq. (2)] are the chemical formation of zincate

[a] Dr. S. Lysgaard, M. K. Christensen, Prof. H. A. Hansen, Prof. J. M. García Lastra, Prof. P. Norby, Prof. T. Vegge
Department of Energy Conversion and Storage
Technical University of Denmark
2800 Kgs. Lyngby (Denmark)
E-mail: stly@dtu.dk
teve@dtu.dk
Homepage: http://www.asc.energy.dtu.dk/

Supporting Information and the ORCID identification number(s) for the author(s) of this article can be found under https://doi.org/10.1002/cssc.201800225.

This publication is part of a Special Issue on Interfacing Theory and Experiment for the Development of Energy Materials. Please visit the issue at http://doi.org/10.1002/cssc.v11.12.

ions ($[Zn(OH)_4]^{2-}$) in solution.[12] However, the dissolution of Zn starts already at $[Zn(OH)_3]^-$.[13] The zincate precipitates above its solubility limit as ZnO according to Equation (3):

$$Zn(OH)_4^{2-} \rightleftharpoons ZnO + H_2O + 2\,OH^- \quad (3)$$

The overall reaction is represented by Equation (4):

$$Zn + 2\,OH^- \rightleftharpoons ZnO + H_2O + 2\,e^- \quad (4)$$

Secondary Zn–air batteries face various challenges that arise from cycling the battery, including:

- dendrite formation:[14] as the zincate is dissolved it has no connection to the Zn electrode and is, therefore, free to adhere anywhere to the conducting electrode during charging. This can lead to dendrite formation, which in the worst case as some cycles can short circuit the battery.
- bifunctional cathode:[6,15,16] as the positive electrode should reduce and evolve oxygen during discharge and charge, respectively, a catalyst for both reactions needs to be employed (bifunctional catalyst). As an alternative, two separate electrodes could be used, but that would complicate the battery cell design and reduce the specific energy.
- precipitation of K_2CO_3 in the cathode as a side-effect of the alkaline electrolyte
- flooding of the cathode if the hydrophobic properties of the cathode are not retained[17]
- corrosion caused by hydrogen evolution

Hydrogen evolution follows the following overall chemical reaction [Eq. (5)]:

$$Zn + 2\,H_2O \rightarrow Zn(OH)_2 + H_2(g) \quad (5)$$

Here, the active material, Zn, is thus consumed without any electrons being transferred and $Zn(OH)_2$ is left.

As corrosion is also an issue in primary Zn–air batteries, it was previously alleviated through the addition of Hg to the Zn electrode.[18] Legislation has now limited the use of Hg in batteries because of its toxicity; therefore, other additives have been sought. At present, the negative electrode material in state-of-the-art primary Zn–air batteries consists of Zn with ppm doping levels of In, Bi, and Al.[19] The effect of these additives on long-term cycling is, however, poorly understood. Here follows a brief survey of the published effects of the doping elements and possible pollutants investigated in this study.

Indium: The In–Zn phase diagram[20] shows a very small solubility of In in Zn, that is, no mixing occurs except some solid solubility in mixtures with up to 0.2% In. Using Ni–In additives resulted in an apparent decrease in both hydrogen evolution reaction (HER) and dendrite formation.[21] In Ref. [22] In is shown to segregate to grain boundaries of Zn particles and decrease HER.

Bismuth: Bi is also used in Zn electrode alloys (always in conjunction with another element though) in low doping concentration. The Bi–Zn phase diagram shows a very small solubility of 0.1% Bi in Zn.[23] Bi is used as binder of particulate Zn to improve conductivity of Zn particles.[24,25] Plate-like Zn precipitates are found in Sn_8Zn_3Bi solder;[26] thus, it seems Bi does not have any positive effect on dendrite formation. McBreen and Gannon[27] reported that a metallic Bi matrix (used together with $Ca(OH)_2$ in Ref. [28]) is responsible for increasing the cycle lifetime of a Zn electrode.

Indium + bismuth: Yano et al.[29] reported a surface alloy of In and Bi to be responsible for suppressing HER on the same level as a Hg additive. Many patents already exist for different mixtures of In and Bi with Zn for use in primary batteries. They are primarily for use in Zn electrodes in alkaline electrochemical cells or paint.[19,30–32] The materials in these patents can include dopant levels of the following elements as well: Pb, Al, Ga, Cd, Li, Ca, Fe, and Mg. Although In and Bi are the most important additives, the other elements can play an important role as well if they have a preference for interacting with the active kink sites for Zn dissolution[12] as these sites can be infrequent on the Zn surface. Zn powders produced by Umicore, which were used to prepare the Zn electrode paste, contain approximately 100 ppm of the elements Bi, In, and Al.[33]

Silver: Ag in the negative Zn electrode is known to be responsible for greatly increasing hydrogen evolution, eventually making the battery effectively useless. Ag/Co_3O_4 is a promising catalyst for both the oxygen reduction reaction (ORR) and the oxygen evolution reaction (OER)[34,35] and thus perfectly suited for Zn–air batteries. For this reason, we have included Ag in this study as it may be transferred from the cathodic catalyst through the electrolyte to the anode, thereby influencing the electrochemical reactions.

Herein, we systematically investigate the possible effects of In, Bi, and Ag in a secondary Zn–air battery, focusing specifically on the behavior of the doping element on battery cycling and the effect of the dopant on especially the Zn dissolution and the HER. First, we will investigate the dissolution reaction on pure Zn surfaces using DFT and compare the results with previous studies to establish that our method is suitable. Next, we perform segregation studies to analyze how the surface is affected by different doping elements. Only elements that will stay on the surface during battery cycling will retain their effect in a secondary battery. We follow this by experimentally measuring the charge and discharge behavior of batteries with the theoretically determined additives on the negative electrode and quantifying the evolution of H_2 and O_2 using DEMS. Subsequently we use DFT to model adsorption of hydroxyl (OH) and hydrogen (H) to investigate Zn dissolution and HER, respectively, on doped Zn electrodes. As both reactions [Eqs. (1) and (5)] involve the formation of $Zn(OH)_2$, we compare the affinity of the Zn surface to both OH and H to evaluate which reaction is preferred and thereby explain why some additives inhibit and others enhance HER. Thus, by studying the doped Zn electrode with a combination of DFT calculations and DEMS measurements, we can pinpoint the effect of the doping elements and determine if the effect is retained upon cycling.

Results and Discussion

DFT study of zinc dissolution

Evaluating the free energy of electrochemical reactions with DFT within the framework of the computational-hydrogen-electrode approach[36] requires a few assumptions with regard to the aqueous environment that is not explicitly calculated. This has been introduced and thoroughly covered previously, which is why only an overview covering the terms needed for Zn surfaces with OH adsorbates is provided.[12] Water is the source of OH in aqueous electrochemistry; thus, the OH adsorption energy (ΔE) is calculated from the reaction: $H_2O + * \rightarrow OH^* + H^+ + e^-$, where * denotes a free surface site and OH* is hydroxyl adsorbed on that site. The change in zero-point energy (ΔZPE) and entropy (ΔS) can be estimated from the reaction by vibrational-mode analysis. The term $\Delta ZPE - T\Delta S$ is estimated to be 0.39 eV per OH molecule at 298.15 K.[12] Additionally, the aqueous environment stabilizes adsorbed species on the surface owing to hydrogen bonding (ΔE_{aq}), which was determined to be 0.57 eV per adsorbed OH molecule.[12] The applied potential is accounted for by adjusting the free energy by $-neU$, where n is the number of electrons transferred to the electrode, e is the electronic charge, and U is the applied electrode bias. For reactions in solutions with pH values different from 0, the free energy is corrected by $-kT \times \ln[H^+] = kT \times \ln 10 \times pH$, where k is the Boltzmann constant and T is the temperature in Kelvin. The Zn–air system investigated here uses an alkaline electrolyte; thus, we use a pH value of 14. In total, the adsorption free energy (ΔG_{ads}) of one OH molecule is calculated by Equation (6):

$$\Delta G_{ads} = \Delta E - \Delta E_{aq} + \Delta ZPE - T\Delta S - kT \times \ln 10 \times pH - neU \qquad (6)$$

The structures used for modelling the reactions are described in the method section. The surface comprises kink-terminated steps separated by (0001) terraces. It is important to note that, thermodynamically, a Zn atom prefers to be in the highest possible coordination. Thus, a real surface would be comprised of larger terraces with a much lower concentration of steps/kinks than those that are feasible to represent in a DFT simulation.

DFT-level modelling of the Zn electrode has only been reported to a limited degree in the literature. The starting point of the current investigation is the DFT study by Siahrostami et al.,[12] where the dissolution reaction of undoped Zn in alkaline solution is found to proceed by dissolving the Zn surface by sequential removal of the residual kink atom on the edge. This mechanism exhibits a low overpotential and has no thermodynamic energy barrier as the dissolved kink atom leaves a new kink atom, that is, an unchanged surface. This is in contrast to the most stable surface, the Zn (0001) terrace, where a dissolved atom leaves a surface vacancy, which entails an energy barrier. The same holds if a Zn atom in the middle of a step edge is dissolved. This and the fact that undercoordinated sites typically are much more reactive[37] result in the kink pathway to be the most probable for Zn dissolution. As illustrated by the atomic structures in Figure 1a, the mechanism starts with an OH molecule adsorbed at a bridge site between the two most undercoordinated Zn atoms (6- and 7-fold coordinated, respectively) on the edge. As more OH molecules adsorb, the Zn atom at the kink is loosened and finally released as $[Zn(OH)_3]^-$.

The graph in Figure 1a shows the free-energy diagram for Zn dissolution with the reaction mechanism going through the kink and edge site on a pure Zn surface. The reaction mechanism is depicted in the illustrations above and below the free-energy diagram for the reaction at the kink and edge sites, re-

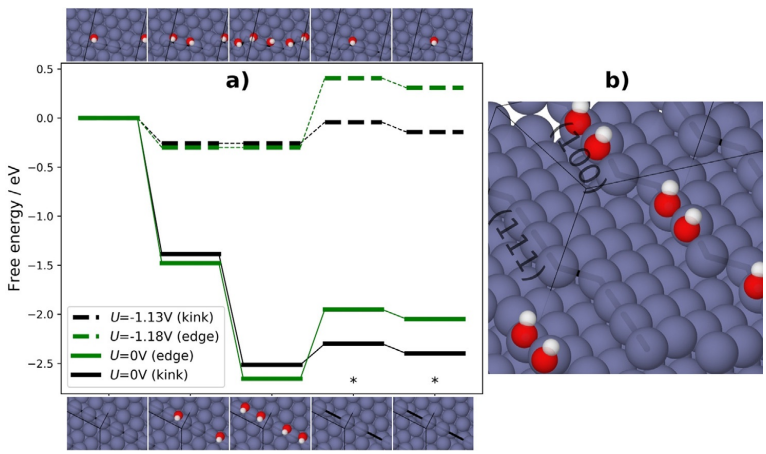

Figure 1. a) Free-energy diagram of the Zn dissolution reaction. Black and green lines represent kink and edge-site dissolution, respectively. The dashed lines show the energies when applying the limiting potentials as noted in the legend. The steps marked by * indicate the energy obtained from experimental dissolution potentials. Above and below the graph are illustrations of the atomic structures from a top view at each step of the reactions dissolving a kink and edge Zn atom, respectively. Zn atoms are grey, O atoms red, and H atoms white. b) Side view of the second step in the reaction involving kink-atom dissolution. The two types of microfacets (111) and (100) are indicated.[38]

spectively. The first two steps correspond to Equation (1) and the last two to Equation (2). Dissolved species are not well reproduced using DFT, and the final two energy levels are therefore fixed to experimental dissolution potentials of $[Zn(OH)_3]^-$ and $[Zn(OH)_4]^{2-}$, respectively. These are −1.15 and −1.199 V at pH 14.[39] The binding of OH is on average 0.1 eV stronger on the (100) microfacet compared to the (111) microfacet (see Figure 1 b); thus, all reported binding energies are from that step. The full lines represent the reactions with no applied bias whereas the dashed lines are the free-energy levels with the limiting potential applied. When a potential is applied, the free-energy levels are corrected by the right-most term in Equation (6). The limiting potential is defined as the highest potential at which no electrochemical steps are uphill in free energy; if the limiting potential is smaller than the equilibrium potential there is an overpotential. The kink-site dissolution has a limiting potential of −1.13 V, very close to the value obtained in Ref. [12], and leading to an overpotential of 0.07 V very close to 0.1 V, which is the experimentally measured overpotential for pure Zn.[40]

For comparison, the Zn dissolution reaction for edge sites is also shown in Figure 1. It has a very similar limiting potential, but that reaction requires an edge vacancy to be formed. We have determined the energy cost of forming an edge vacancy to be 0.35 eV by using bulk Zn as a reference. This energy cost is added to the steps in which a Zn atom, in the form of $[Zn(OH)_3]^-$ or $[Zn(OH)_4]^{2-}$, has left the surface (marked with * in Figure 1 a). This represents a chemical energy barrier for the mechanism in which an edge atom is removed that is not present when removing the kink atom. The reason for clarifying the reaction mechanism on the edge will become evident when studying doped Zn, especially in the case of doping with Bi.

DFT study on arrangement of doping elements

To elucidate which elements could have a positive effect in secondary Zn–air batteries, by being thermodynamically stable on the surface of Zn both with and without an OH coverage, we have performed a segregation study of a series of elements on Zn; this is included in Figure S3 in the Supporting Information. The three elements we will include in this study are In and Bi, which have a clear preference for the surface and has previously been shown to have beneficial effects for the negative Zn electrode, and Ag that has no clear surface preference but is known to have a disadvantageous effect on the Zn electrode. The preferential surface segregation of In and Bi implies that the concentration in the surface of these elements will be larger than the ppm levels reported as optimal for powders.

Figure 2 shows the relative energy for different placements of a single atom of In, Bi, and Ag on the kinked Zn surface without considering any adsorbate effect. Because the computational cell contains two steps, the (100) and (111) microfacets, which were not considered previously, the relative energy is an average of dopant placements at or near each step. The energy as a function of coordination follows the same trend at both steps. The kink site is the most favorable site for In and Bi

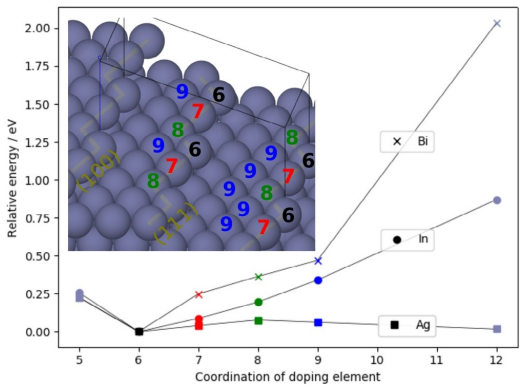

Figure 2. Relative energies of sites with different coordination of the dopant elements In, Bi, and Ag. The energy of the dopants at sites with coordination number 6 (kink site) is defined as zero. The inset is an illustration of the kink structure. The numbers on the atoms indicate the coordination number of that atom. Coordination 6: kink-site atom; coordination 7: edge atom; coordination 8: edge atom just behind a kink; and coordination 9: atom in the terrace. Not shown are sites on (coordination 3–5) and below the surface (coordination 10–12), which were all higher in energy. Indicated are also the two types of step microfacet ((100) and (111)) present in the computational cell.

to reside. For In, the 7-fold-coordinated step site is very close in energy to the kink site, whereas for Bi all other coordination types are related to large energy penalties. Sites with low coordination, such as adatoms on a terrace (coordination number 3), were also tested and found to be unfavorable. This means that the mechanism for Zn dissolution proposed for pure Zn in Ref. [12] will not proceed exactly as described in the doped systems because the active site in that process will change in the presence of In or Bi dopants. The site favored by Ag can not be established as clearly . The energy gain for a 6-coordinated Ag atom, at the kink site, is less than 0.1 eV compared to the other surface sites. Compared to a 12-fold coordinated bulk site the energy gain is even less. Thus, it is improbable that Ag will stay on the surface of Zn during recycling of a secondary battery. The risk of having Ag on the negative Zn electrode is, however, still present during cycling in a secondary Zn–air battery if it is used in combination with an unstable catalyst for the air electrode, for example, Ag/Co_3O_4. Thus, the effect of the element is still important to analyze. With these findings, we proceed with our experimental investigations to show that the additives influence charge/discharge voltages and investigate the influence on the performance during cycling in the presence of In, Bi, and Ag additives. We will revisit the dissolution reactions for doped Zn surfaces with DFT afterwards.

DEMS study on anode cycling with dopants

The galvanostatic cycling data in Figure 3 show the electrochemical behavior of a reference Zn–air battery and four similar batteries each with a different additive. Common features

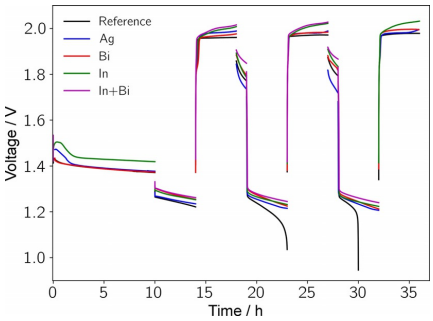

Figure 3. Galvanostatic cycling data consisting of discharge–charge cycles at 1 mA cm^{-2} for five Zn–air batteries with a Zn foil anode and a $NiCo_2O_4$ cathode. One reference battery, without any additives to the electrolyte, (black) and four batteries with additives Ag (blue), Bi (red), In (green), and a 50:50 mixture of In and Bi (purple) in the electrolyte were measured. Each discharge and charge were limited to 4 h. The OCV was measured for 10 h before the first cycle and for 1 h before the second and third discharge.

across all measurements are that the initial open-circuit voltage (OCV) decreases and that the first discharge plateau has a slight slope. See Figure S1 for an analysis of the slope for the different additives. Care should be taken when evaluating very small differences in the experimentally determined overpotential as contributions from, for example, contact resistance could influence the absolute value of the measured voltage. During charge, the reference Zn–air battery exhibits a flat charge plateau at 1.95 V whereas that of the cells with additives is slightly higher and increases with charging time. Particularly the cells containing In as additive show increasing charging potential over time. After the first charge, the OCV value is around 1.8 V. The increase in OCV compared to the pristine cell is attributed to a slight oxidation of the cathode. During the second discharge, the reference Zn–air cell potential shows a drastic decline until the discharge time limit. During the third charge, this feature is even more significant with the potential reaching the lower potential limit of 0.95 V. Despite this, the charging was continued for the full duration of 4 h for both the second and third charge. This is a result of nonelectrochemical reactions taking place during discharge (chemical oxidation and hydrogen evolution) and/or oxidation of other species (e.g., in the catalyst) taking place during charge.

The discharge potentials decrease with each cycle for all additives, see Figure S1 in the Supporting Information. The Ag additive results in a decreasing charging potential with each cycle, indicating that the effect of Ag diminishes over cycling. The charging potentials of the other additives increase slightly but their relative differences remain stable. The addition of In to the electrolyte is beneficial, resulting in higher OCV and discharging potential although during charging the overpotential increases. Although this does not initially appear to be beneficial, it is related to a suppression of parasitic reactions as discussed below. Bi has a similar low overpotential on discharge, but it increases with more cycles. On charging, the voltage is constant with a slightly higher overpotential than the reference Zn sample. The combination of In and Bi consistently has the highest OCV and discharging potentials. The same is true for the charging potentials but, as with In, the effect of suppressing parasitic reactions outweigh the detrimental effect on energy efficiency.

Based on the DEMS measurements it is possible to quantify the amount of H_2 and O_2 evolved and to correlate this with the number of electrons passed through the cell. This allows determination of the efficiency of the electrochemical processes (e.g., determining the number of electrons per O_2 evolved) and to detect parasitic reactions. In this study, the DEMS measurements were used to quantify the electrochemical oxygen evolution and determine the contribution from electrochemical and chemical hydrogen production. As mentioned earlier, the electrochemical hydrogen production is from water splitting whereas the chemical hydrogen evolution is from the chemical oxidation of Zn metal.

In Figure 4, the effect of the additives on OER and HER during charge is broken down into hourly production. The low initial signal during each charge is due to the large headspace of the electrochemical cell used, which creates a delay in detection of the gasses evolved. On the first cycle, the O_2 signals are similar for the reference and the cell with Ag as additive, but the Ag additive yields more H_2. With increased cycle number, the H_2 signal decreases along with the O_2 signal. The decreased H_2 signal with cycling is consistent with the DFT study on the additive arrangement (see Figure 2), which suggests that Ag is not preferred on the surface of Zn, also see Figure S2 and Table S1 in the Supporting Information for the exact DEMS signals. In the case of an Ag-containing air electrode such as Ag/Co_2O_3), additional Ag may shuttle to the Zn electrode, unless an Ag separator is used, resulting in enhanced H_2 evolution. The data support the theoretical findings that Bi primarily affects the potentials of the Zn–air battery as the H_2 and O_2 production levels are nearly identical to the reference battery, with Bi slightly promoting O_2. Adding In is beneficial as it, similarly to Bi, promotes O_2 evolution while simultaneously decreasing the H_2 evolution. During charging, the battery with In additives has a different charging profile with higher potential and higher slope than batteries with pure Zn or other additives. It is, however, important to note that at the same time the H_2 evolution is dramatically decreased compared to the batteries without In as additive, showing that the suppression of parasitic H_2 evolution increases with time and with the number of cycles. This also indicates that a more efficient distribution of In on the Zn surface is established during cycling. When Bi and In are added together, the O_2 evolution is similar to the that for the other additives and the H_2 evolution is the lowest of all experiments while still retaining the highest discharge potential (see Figure 3) and sustaining the positive effects over cycling. As such, the In + Bi additives dramatically affect the conditions and performance of the Zn electrode. By examining the ratio of O_2 to H_2, it is clear that Ag is not a desirable additive and although a similar statement could be made for Bi, the DEMS data suggest that the beneficial effect of Bi is primarily from the stabilization of the discharge potentials (Figure S1 in the Supporting Information) as well as further suppression of H_2 evolution when combined with In.

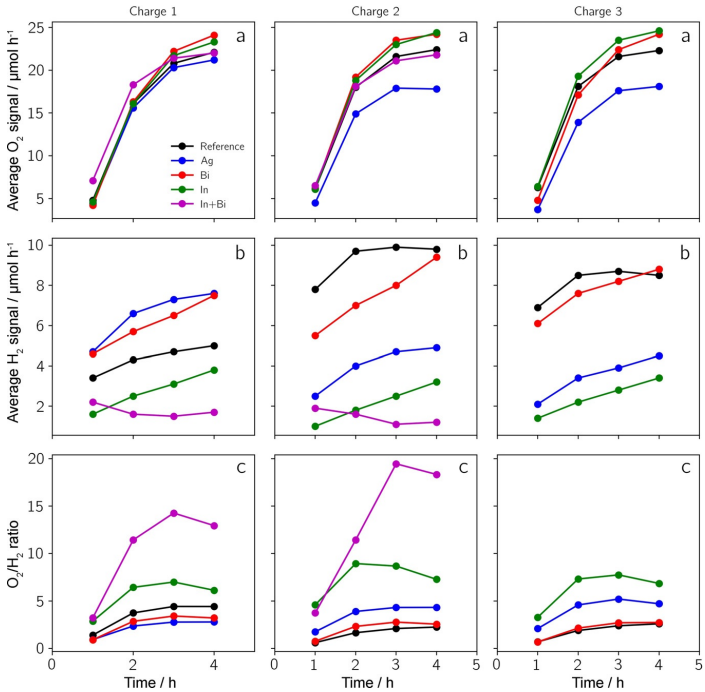

Figure 4. DEMS data collected during charge for each cell. Mass spectrometer data were collected every 10 min from the headspace of the cell and were averaged to obtain hourly gas production rate (µmol h^{-1}): a) hourly average O_2 signal, b) hourly average H_2 signal, and c) the respective O_2/H_2 ratio.

In summary, adding In is clearly beneficial despite the increased overpotential on charging, which would lower the apparent energy efficiency; however, because of the reduced H_2 evolution there is less degradation of the Zn electrode, thus improving cycle life. Mixing In and Bi combines the beneficial properties of each additive as it yields the best O_2-to-H_2 ratio, better than In by itself, and also yields high discharging potentials. To gain a better understanding of the synergy and further insights how the In and Bi additives affect the properties, we have performed additional DFT calculations on the Zn-dissolution reaction mechanism for the doped systems.

DFT study on Zn dissolution with dopants

Doped with Bi and In, the free-energy diagram for Zn dissolution takes the form shown in Figure 5a. The dissolution of a Zn atom from the step leaves a vacancy the energy of which is added to the third and second last steps in the free-energy diagram, with the final step rearranging the step on the surface and removing the vacancy. The last adsorption step of the OH molecule before the dissolution of $[Zn(OH)_3]^-$ on the Bi- and In-doped surfaces is shown in Figure 5b and c, respectively; two OH molecules are adsorbed and the Zn atom about to dissolve coordinates to both molecules. The different effects of the two dopants are clearly visible: OH avoids the Bi atom situated at the kink site, thus an edge atom is dissolved instead. Here, it should be noted that the low limiting potential of −0.73 V shown in Figure 5a is an artifact of the limited size of the computational cell. For a more realistic kink-to-kink distance, there would not be an interaction between the leaving Zn atom and the doping element on the next kink (see Figure 5b); therefore, the dissolution process would follow the edge mechanism, as shown in Figure 1a, leading to a limiting potential of approximately −1.18 V. The vacancy energy cost used here is 0.35 eV, the same as estimated for the pure-Zn edge. During the adsorption process, the small displacement of the In atom from the kink site allows OH to adsorb to the Zn atom closest to the kink; this atom dissolves from the step, with the vacancy formation energy penalty in this reaction stemming from the In atom moving back to its favored position at the kink, which is determined to be 0.2 eV for the (100) microfacet. The calculated limiting potential of the In-doped system is −1.21 V. As the equilibrium potential is −1.199 V, In doping effectively removes the fundamental overpotential. This effect comes from the stronger binding of the OH closest to the Zn, due to a favorable interaction with In.

The addition of both In and Bi is found to stabilize the cyclic performance as shown in Figure 3. Using DFT, we have determined that the combination of both elements at a step is in fact more stable than each step only having one of the two dopants. The energy gain by having two steps with Bi–In neighbors as an edge termination compared to one with In–In

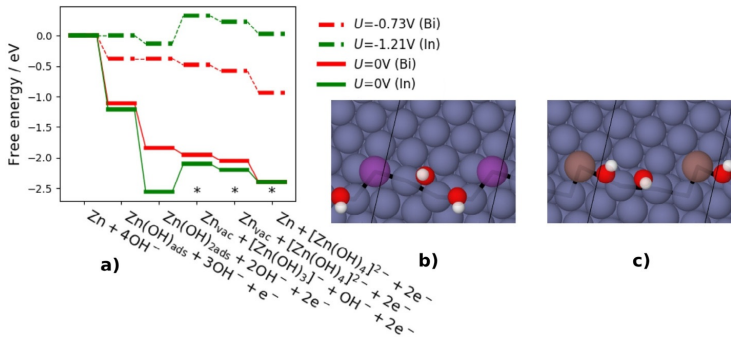

Figure 5. a) Free-energy diagram of the electrochemical steps of Zn dissolution on In- and Bi-doped Zn surfaces. Full and dashed lines are with no applied potential and with the limiting potential applied, respectively. * marks the energy levels fixed to experimental dissolution potentials. b) Atomic illustration of the second step in the reaction with Bi doping. c) as (b) but with In doping.

and one with Bi–Bi edge terminations is 0.1 eV per doping atom, that is, a significant stabilization, which would explain the almost constant charging and discharging potentials for In + Bi in Figure 3.

Figure S4 in the Supporting Information shows the free energy-diagram of Ag-doped Zn. The effect of Bi and Ag is very similar; adsorption of OH is weakened, leading to the Zn dissolution reaction involving Zn atoms on the edge. At this point, a question arises: if Ag and Bi apparently behave similarly, why is Ag detrimental for Zn–air batteries whereas Bi is used in the state-of-the-art Zn paste? The answer is revealed when looking at adsorption (and in turn production) of H_2.

DFT study of corrosion versus dissolution

As discussed in the introduction, both Zn dissolution and hydrogen evolution reactions occur through a $Zn(OH)_2$ intermediate, see Equations (1) and (5). In Figure 6, we compare the adsorption energies of H and OH on both pure and doped Zn with an increasing coverage of OH to determine how both reactions are influenced by dopants; a similar method was used previously to compare CO_2 reduction and HER.[41] According to the binding energies of OH in the bottom part of Figure 6, for both Bi and Ag the energy gain achieved by adsorbing OH decreases with respect to the pure Zn surface, thereby Zn hindering dissolution. The adsorption-energy curves for Bi and Ag are approaching the energy for terrace adsorption as the OH coverage increases; it is thus not unlikely that a too large concentration of Bi in the Zn electrode will block the edges completely and could drive Zn dissolution to take place on the terrace.

The adsorption energies of OH for the In-doped system has a bump at 2/3 coverage, but decreases with coverage; the same is seen for the adsorption of H. Thus, the reported decrease in HER in In-doped Zn,[22] also seen in Figure 4, must come from the fact that the decrease in adsorption energy of H is outweighed by the decrease in OH adsorption energy. Bi has the opposite effect on H adsorption; therefore, although the effect of Bi is seemingly detrimental to Zn dissolution by lowering the OH affinity, it is also detrimental to HER. Overall,

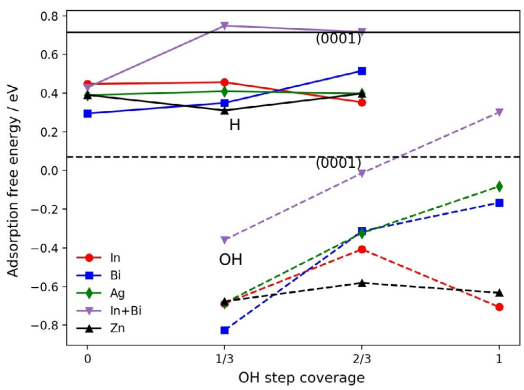

Figure 6. Comparison of binding energies of H (top) and OH (bottom) on kink surfaces of either pure Zn or Zn doped with In, Bi, or Ag. The graph shows the adsorption free energy of H and OH on the kink Zn surface as a function of the amount of OH already adsorbed (coverage). Full and dashed lines are for H and OH adsorption, respectively. The horizontal lines spanning the whole *x*-axis represent adsorption energies on the (0001) terrace.

the presence of Bi therefore has a positive effect on the Zn electrode, in particular when co-doped with In. On the other hand, Ag does not give rise to the same weakening of H adsorption as Bi, hence Ag only hinders Zn dissolution, leaving HER as the preferred process.

The combined In + Bi adsorption energies show a trend different from the other adsorbates. OH adsorption energies are markedly higher, but this can be explained by the limited number of sites available on the step; all dopant calculations have been performed on a constant-sized step. With two doping atoms there is effectively one less site available for adsorption. Thus, by shifting the In + Bi OH line to the right by 1/3 coverage one achieves almost identical values to the Bi doping. This cannot account for the H adsorption behavior, as the increase in adsorption energy occurs already at an OH coverage of 1/3, where free sites with only Zn are available. The

decrease must then come down to an electronic effect of combining In and Bi. Only the combination of both In and Bi can switch the most favorable adsorption site for H to the (0001) terrace where HER is not considered an issue.[2] For all other dopants, the adsorption energy of H on Zn (0001) is still 0.2 eV higher than the highest energy on the kink.

Conclusions

The Zn dissolution and parasitic hydrogen evolution reaction (HER) at the negative electrode in secondary Zn–air batteries were modelled using density functional theory (DFT) and measured experimentally using differential electrochemical mass spectrometry (DEMS) on In-, Bi-, and Ag-doped as well as pure Zn surfaces. To influence the negative electrode chemistry upon cycling of the battery, the doping elements need to be thermodynamically or kinetically stabilized on the surface as Zn is plated on the negative electrode during charging. DFT calculations showed that In and Bi strongly prefers the kink site, whereas there was no clear driving force for Ag to remain on the surface. This is also confirmed experimentally, where In and Bi change the potential characteristics as well as O_2/H_2 evolution consistently through cycling, compared to pure Zn foil, and the effect of Ag is lost after a few cycles. Both DFT calculations and DEMS measurements show that In decreases the overpotential for Zn dissolution. The primary effect of Bi is found to be stabilizing In on the Zn surface; DEMS measurements with both dopants show a constant behavior of the charge/discharge potentials with cycling. The DFT calculations confirm that steps with both Bi and In are 0.1 eV per doping atom more stable than individual steps with only one of the doping elements. The codoping of both In and Bi decreased the HER dramatically (Figure 4), and the decrease in HER was explained using DFT to stem from a much weaker H adsorption on Bi- and In-codoped steps. In the same manner, Ag was found to increase the HER, demonstrating a weakening of the OH binding energy, but has no effect on H binding, leaving HER as the preferred reaction.

Experimental Section

Computational details

The density functional theory calculations were all performed using the GPAW (v0.11.0) code,[42,43] which is a real-space implementation of the PAW method.[44] Structure manipulation and post analysis of calculations were performed using ASE (v3.9.1).[45] The RPBE functional[46] was used, this functional was developed to provide accurate adsorption energies for molecules on surfaces. All reported energies were calculated using the finite difference (fd) mode in GPAW, working on the real-space grid.

All geometrical relaxations of clean surfaces were performed in a two-step procedure, where the linear combination of atomic orbitals (LCAO) mode in GPAW[47] was used for the initial relaxation followed by a relaxation in fd mode. This allowed the computationally cheaper LCAO mode to do the heavy lifting of the geometrical relaxation of the Zn surface that, because of its low surface energy, tended to require many relaxation steps. For calculations of adsorbed species, this approach was not found to be advantageous, thus a full relaxation in fd mode was performed. It is known that the basis set superposition error (BSSE),[48] present in LCAO mode calculations, artificially enhances the interaction between adsorbate and substrate. This could lead to incorrect geometries as the correction scheme is not applicable when extracting forces from GPAW calculations at the moment.

The free-energy diagram of zinc dissolution was calculated from the adsorption energies using a well-known method[36] and also used in a previous DFT study on Zn dissolution.[12] We assumed the temperature to be 298.15 K and the pH value to be 14.

All adsorption energies, except the edge dissolution pathway illustrated in the lower part of Figure 1a, were reported from a structure with 4 atoms on each step in the unit cell, each step was terminated by a kink, which corresponds to a sixfold coordinated atom. For a representative illustration see Figure 1b and the inset in Figure 2. As previously mentioned, the computational cell contained two steps with microfacets of the types (100) and (111). If not stated otherwise, the reported energies stemmed from adsorption on the (100) step, as these are more stable. To avoid interaction between steps they were separated by 3 and 4 terrace rows. The interaction between a kink atom and its periodic image was minimal. The unit cell had four close-packed Zn atomic layers, during geometrical relaxation the bottom two were fixed to the bulk structure and lattice constant. We used the experimental lattice constant of $a=2.66$ Å and $c=4.94$ Å.[49] Perpendicular to the surface a vacuum of 12 Å was inserted to prevent interaction between computational slabs. We used a (3,3,1) *k*-point sampling in a Monkhorst–Pack scheme[50] and a grid spacing of 0.18 Å.

DEMS measurements

All electrochemical measurements were performed using a two electrode Air–Ni cell of the ECC series from EL-Cell. The cathode was $NiCo_2O_4$ (NCO) with PTFE for hydrophobicity and micrometer-sized Ni particles for conductivity supported on a Ni 40 mesh. The electrolyte was 200 μL 6 M KOH and contained two 260 μm thick GF/A Whatman glass fiber separators. The additives Ag, Bi, and In were added from 5 mM Ag/Bi/In-nitrate aqueous solutions. In one experiment, an additive containing 2.5 mM In nitrate and 2.5 mM Bi nitrate was added to a Zn–air cell. The metal nitrate salts were acquired from Sigma–Aldrich of at least 99.9% purity, and their concentrations were calculated from the anhydrous weight. Bi nitrate, which is not completely soluble in water, was sonicated and stirred before use to ensure that the particles were dispersed well in solution. 28 μL of the additive solution were added to the cell between the two separators before electrolyte was added. The current collector for the positive electrode was a perforated Ni plate from EL-Cell. The current collector for the negative electrode was a 8 μm thick 99.99% Cu foil from MTI corp.

Experimental procedure

Each cell was cycled three times for OCV measurements prior to each discharge–charge experiment. The Initial OCV time was 10 h whereas the flowing OCV measurement time was 1 h. The galvanostatic cycling was performed for 4 h at a current density of 1 mA cm^{-2} (geometric area) for both discharge and charge. DEMS measurements were performed during charging with the setup described in Refs. [51–53]. The gas was collected every 10 min. After each discharge the cell was flushed for 1 h to remove oxygen in the headspace of the cell.

Anode preparation

Zn foil electrodes were stamped from a 0.125 mm-thick Zn sheet (Goodfellow, 99.95%). After stamping, the foil was washed by submersion in a beaker with purified water, then in a beaker with ethanol and dried in a fumehood to remove any dustparticles from the packing.

Cathode preparation

The NCO cathodes were prepared on Ni 40 mesh (Alfa Aesar) using 39 wt% $NiCo_2O_4$ powder (Cerpotech), 23 wt% Ni powder (Strem Chemicals, 3–7 μm), 23 wt% Ni powder (Alfa Aesar, 150–200 mesh), and 15 wt% PTFE (Sigma–Aldrich) with a total loading of $157 \pm 25\ g\,cm^{-2}$. The powders were mixed, compressed at 3 bar per 18 cm^2 and heated at 340 °C for 1 h.[28]

Acknowledgements

This work was supported by the Horizon 2020 framework project ZAS, grant number 646186. We would also like to acknowledge Prof. Peter Holtappels and Dr. Vladimir Tripkovic for valuable discussions. Furthermore, Dr. Alexander Kube is acknowledged for providing the $NiCo_2O_4$ catalyst.

Conflict of interest

The authors declare no conflict of interest.

Keywords: batteries · density functional theory calculations · differential electrochemical mass spectrometry · doping · zinc

[1] V. Caramia, B. Bozzini, *Mater. Renewable Sustainable Energy* **2014**, *3*, 28.
[2] P. Gu, M. Zheng, Q. Zhao, X. Xiao, H. Xue, H. Pang, *J. Mater. Chem. A* **2017**, *5*, 7651 – 7666.
[3] M. A. Rahman, X. Wang, C. Wen, *J. Electrochem. Soc.* **2013**, *160*, A1759 – A1771.
[4] J. Fu, Z. P. Cano, M. G. Park, A. Yu, M. Fowler, Z. Chen, *Adv. Mater.* **2017**, *29*, 1604685.
[5] Y. Li, H. Dai, *Chem. Soc. Rev.* **2014**, *43*, 5257 – 5275.
[6] E. Davari, D. Ivey, *Sustainable Energy Fuels* **2018**, *2*, 39 – 67.
[7] K. G. Gallagher, S. Goebel, T. Greszler, M. Mathias, W. Oelerich, D. Eroglu, V. Srinivasan, *Energy Environ. Sci.* **2014**, *7*, 1555.
[8] T. Vegge, J. M. Garcia-Lastra, D. J. Siegel, *Curr. Opin. Electrochem.* **2017**, *6*, 100 – 107.
[9] Y. Li, J. Lu, *ACS Energy Lett.* **2017**, *2*, 1370 – 1377.
[10] O. Haas, J. Van Wesemael, *Encyclopedia of Electrochemical Power Sources*, Elsevier, **2009**.
[11] P. C. K. Vesborg, T. F. Jaramillo, *RSC Adv.* **2012**, *2*, 7933.
[12] S. Siahrostami, V. Tripković, K. T. Lundgaard, K. E. Jensen, H. A. Hansen, J. S. Hummelshøj, J. S. G. Mýrdal, T. Vegge, J. K. Nørskov, J. Rossmeisl, *Phys. Chem. Chem. Phys.* **2013**, *15*, 6416 – 6421.
[13] Y.-C. Chang, G. Prentice, *J. Electrochem. Soc.* **1984**, *131*, 1465.
[14] A. L. Zhu, D. P. Wilkinson, X. Zhang, Y. Xing, A. G. Rozhin, S. A. Kulinich, *J. Energy Storage* **2016**, *8*, 35 – 50.
[15] V. Tripkovic, H. A. Hansen, T. Vegge, *ChemSusChem* **2018**, *11*, 629 – 637.
[16] V. Tripkovic, H. A. Hansen, T. Vegge, *ACS Catal.* **2017**, *7*, 8558 – 8571.
[17] D. Schröder, T. Arlt, U. Krewer, I. Manke, *Electrochem. Commun.* **2014**, *40*, 88 – 91.
[18] L. M. Baugh, F. L. Tye, N. C. White, *J. Appl. Electrochem.* **1983**, *13*, 623 – 635.
[19] I. A. J. Strauven, M. L. Meeus, (Union Miniere), CA2153330 A1, **1994**.
[20] J. Dutkiewicz, W. Zakulski, *Bull. Alloy Phase Diagrams* **1984**, *5*, 284 – 289.
[21] C. W. Lee, K. Sathiyanarayanan, S. W. Eom, H. S. Kim, M. S. Yun, *J. Power Sources* **2006**, *159*, 1474 – 1477.
[22] A. G. Muñoz, S. B. Saidman, J. B. Bessone, *Corros. Sci.* **2001**, *43*, 1245 – 1265.
[23] J. Vizdal, M. H. Braga, A. Kroupa, K. W. Richter, D. Soares, L. F. Malheiros, J. Ferreira, *CALPHAD Comput. Coupling Phase Diagrams Thermochem* **2007**, *31*, 438 – 448.
[24] L. Lin, R. Shepard, (Gillette), US6300011 B1, **2001**.
[25] R. E. Durkot, L. Lin, P. B. Harris, (Duracell), US6284410 B1, **2001**.
[26] M. Y. Chiu, S. S. Wang, T. H. Chuang, *J. Electron. Mater.* **2002**, *31*, 494 – 499.
[27] J. McBreen, E. Gannon, *J. Power Sources* **1985**, *15*, 169 – 177.
[28] C. Zhang, J. M. Wang, L. Zhang, J. Q. Zhang, C. N. Cao, *J. Appl. Electrochem.* **2001**, *31*, 1049 – 1054.
[29] M. Yano, S. Fujitani, K. Nishio, Y. Akai, M. Kurimura, *J. Power Sources* **1998**, *74*, 129 – 134.
[30] C. Henninot, Y. Strauven, (Umicore), US20120096989 A1, **2012**.
[31] K. Kuwayama, J. Nakagawa, K. Tomii, K. Hagimori, (Toho Zinc), US4432937, **1984**.
[32] H. W. Sarkas, I. V Barsukov, (Nanophase Tech), US9105923 B2, **2015**.
[33] The contents of "Zn BIA100" is from the chemical analysis in a Umicore—Certificate of Analysis obtained during the purchase of the powder.
[34] R. Gao, Z. Yang, L. Zheng, L. Gu, L. Liu, Y. L. Lee, Z. Hu, X. Liu, *ACS Catal.* **2018**, *8*, 1955 – 1963.
[35] D. Wittmaier, N. A. Cañas, I. Biswas, K. A. Friedrich, *Adv. Energy Mater.* **2015**, *5*, 1500763.
[36] J. K. Nørskov, J. Rossmeisl, A. Logadottir, L. Lindqvist, J. R. Kitchin, T. Bligaard, H. Jónsson, *J. Phys. Chem. B* **2004**, *108*, 17886 – 17892.
[37] S. H. Brodersen, U. Grønbjerg, B. Hvolbæk, J. Schiøtz, *J. Catal.* **2011**, *284*, 34 – 41.
[38] M. A. Van Hove, G. A. Somorjai, *Surf. Sci.* **1980**, *92*, 489 – 518.
[39] M. Cai, S.-M. Park, *J. Electrochem. Soc.* **1996**, *143*, 2125.
[40] J. C. Salas-Morales, J. W. Evans, *J. Appl. Electrochem.* **1994**, *24*, 858 – 862.
[41] Y.-J. Zhang, V. Sethuraman, R. Michalsky, A. A. Peterson, *ACS Catal.* **2014**, *4*, 3742 – 3748.
[42] J. J. Mortensen, L. B. Hansen, K. W. Jacobsen, *Phys. Rev. B* **2005**, *71*, 35109 – 35111.
[43] J. Enkovaara, C. Rostgaard, J. J. Mortensen, J. Chen, M. Dulak, L. Ferrighi, J. Gavnholt, C. Glinsvad, V. Haikola, H. A. Hansen, et al., *J. Phys. Condensed Matter* **2010**, *22*, 253202.
[44] P. Blöchl, *Phys. Rev. B* **1994**, *50*, 17953 – 17979.
[45] A. Hjorth Larsen, J. J. Mortensen, J. Blomqvist, I. E. Castelli, R. Christensen, M. Dułak, J. Friis, M. N. Groves, B. Hammer, C. Hargus, et al., *J. Phys. Condens. Matter* **2017**, *29*, 273002.
[46] B. Hammer, L. Hansen, J. Nørskov, *Phys. Rev. B* **1999**, *59*, 7413 – 7421.
[47] A. H. Larsen, M. Vanin, J. J. Mortensen, K. S. Thygesen, K. W. Jacobsen, *Phys. Rev. B* **2009**, *80*, 195112.
[48] F. B. van Duijneveldt, J. G. C. M. van Duijneveldt-van de Rijdt, J. H. van Lenthe, *Chem. Rev.* **1994**, *94*, 1873 – 1885.
[49] N. W. Ashcroft, N. D. Mermin, *Solid State Physics*, Saunders, **1976**.
[50] H. J. Monkhorst, J. D. Pack, *Phys. Rev. B* **1976**, *13*, 5188 – 5192.
[51] J. Højberg, K. B. Knudsen, J. Hjelm, T. Vegge, *ECS Electrochem. Lett.* **2015**, *4*, A63 – A66.
[52] J. Højberg, *PhD Thesis*, Technical University of Denmark, **2015**.
[53] J. Højberg, B. D. McCloskey, J. Hjelm, T. Vegge, K. Johansen, P. Norby, A. C. Luntz, *ACS Appl. Mater. Interfaces* **2015**, *7*, 4039 – 4047.

Manuscript received: January 31, 2018
Revised manuscript received: March 23, 2018
Accepted manuscript online: March 30, 2018
Version of record online: May 2, 2018

CHEMISTRY & SUSTAINABILITY
CHEMSUSCHEM
ENERGY & MATERIALS

Supporting Information

Combined DFT and Differential Electrochemical Mass Spectrometry Investigation of the Effect of Dopants in Secondary Zinc–Air Batteries

Steen Lysgaard,* Mathias K. Christensen, Heine A. Hansen, Juan Maria García Lastra, Poul Norby, and Tejs Vegge*[a]

cssc_201800225_sm_miscellaneous_information.pdf

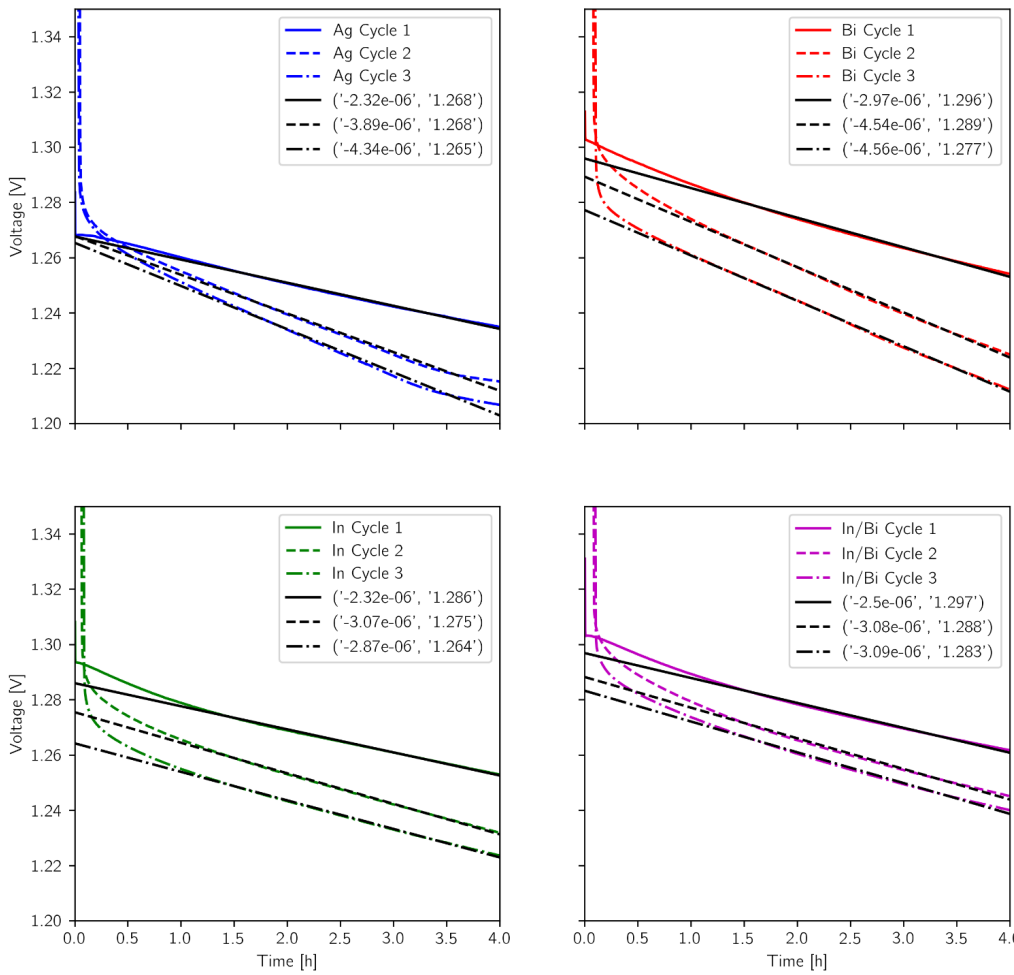

Figure S1: All discharge profiles for each additive with linear fits of the final 3 hours.

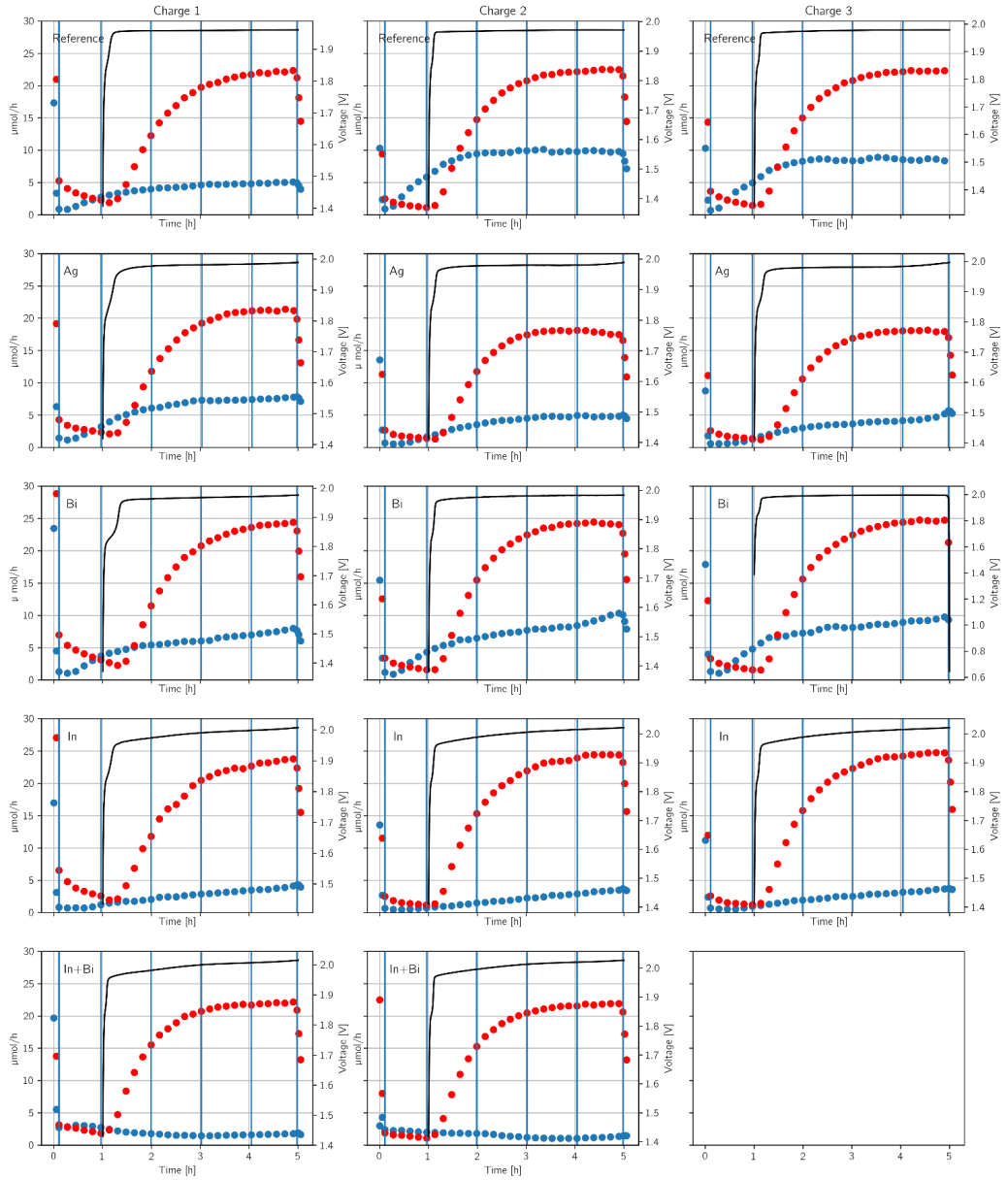
Charge 1
Charge 2
Charge 3
Reference
Ag
Bi
In
In+Bi
µmol/h
Voltage [V]
Time [h]

Figure S2: Charge potential (black line) with DEMS signal for O_2 (red dots) and H_2 (blue dots) for each charge cycle without additives and for each additive in the order of No additive, Ag, Bi, In, In/Bi. The vertical blue lines indicate what values are used to estimate production H_2 and O_2 production. The average production includes the data point that the lines crossed and the five data points to its right. The gas evolution during headspace gas purging before the charging starts is not included in any of the production numbers. Additionally, there are 3 data points taken at a faster sampling rate before and after charge. These are not used in any values in the article and has the primary purpose of checking the purging is correct.

Table 1: Differential Electrochemical Mass Spectrometry (DEMS) data for O_2 and H_2 measured in µmol/h for Zn-air batteries with additives during each hour of charge.

	No Additive		Ag		Bi		In		In+Bi	
	O_2	H_2	O_2	H_2	O_2	H_2	O_2	H_2	O_2	H_2
1 Charge	4.8	3.4	4.4	4.7	4.2	4.6	4.6	1.6	7.1	2.2
	16.1	4.3	15.6	6.6	16.3	5.7	16.1	2.5	18.3	1.6
	20.8	4.7	20.3	7.3	22.2	6.5	21.7	3.1	21.4	1.5
	22.1	5.0	21.2	7.6	24.1	7.5	23.3	3.8	22.0	1.7
2 Charge	6.1	7.8	4.5	2.5	6.2	5.5	6.1	1.0	6.5	1.9
	18.0	9.7	14.9	4.0	19.2	7.0	18.8	1.8	18.1	1.6
	21.6	9.9	17.9	4.7	23.5	8.0	23.0	2.5	21.1	1.1
	22.4	9.8	17.8	4.9	24.2	9.4	24.4	3.2	21.8	1.2
3 Charge	6.3	6.9	3.7	2.1	4.8	6.1	6.4	1.4	N/A	N/A
	18.1	8.5	13.9	3.4	17.1	7.6	19.3	2.2	N/A	N/A
	21.6	8.7	17.6	3.9	22.4	8.2	23.5	2.8	N/A	N/A
	22.3	8.5	18.1	4.5	24.2	8.8	24.6	3.4	N/A	N/A

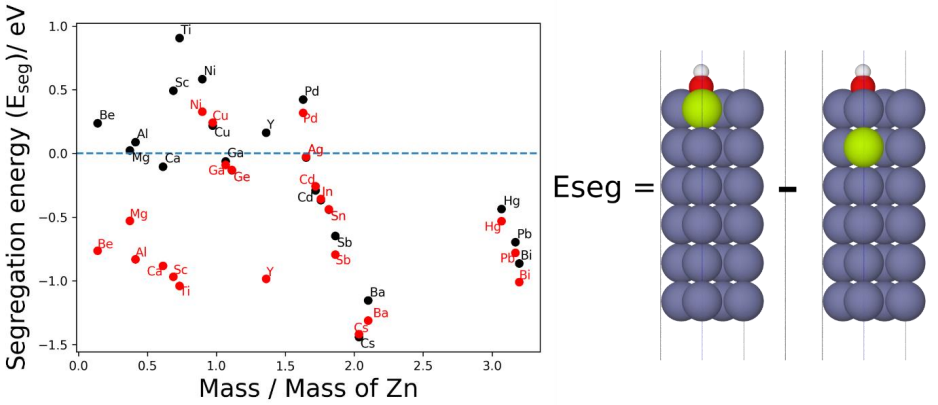

Figure S3: Segregation energy of a doping element in Zn (0001). The segregation energy is defined as the illustration to the left suggests; E_{seg} = E(dopant in surface layer) – E(dopant in subsurface layer). Red points are with a single OH adsorbed, as shown, corresponding to a coverage of ¼, black points are with no adsorbate. The computational cell has 2x2 atoms in each of the 6 layers. During relaxation all slab atoms are fixed so only the adsorbate can relax. This is done due to the small unit cell in which a single doping element corresponds to a large doping concentration and can as such induce great rearrangement of the Zn making the comparison between different doping elements impossible. All computational parameters are equal to the ones in the main paper, except the k-point sampling which is here (6, 6, 1).

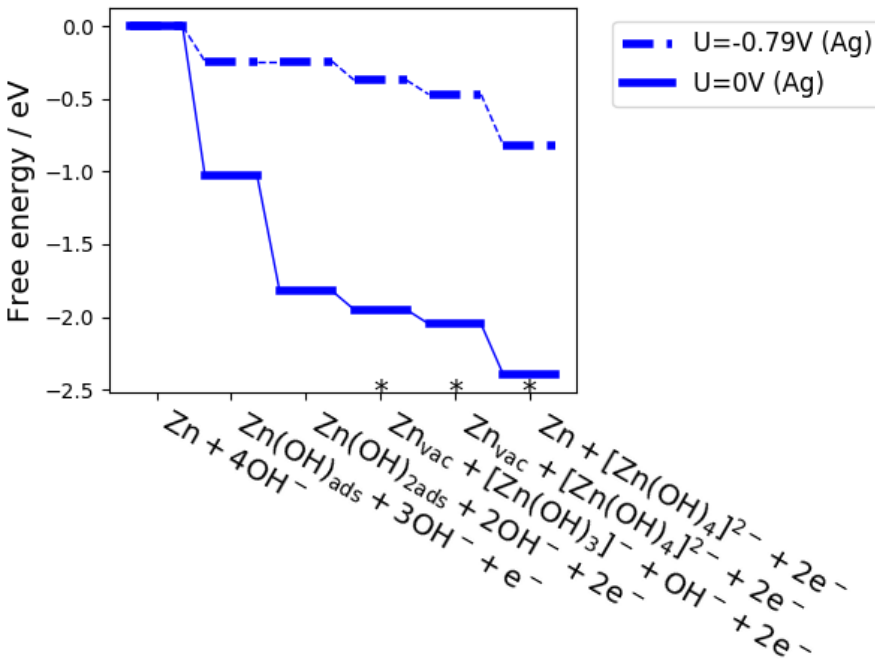

Figure S4: Free energy diagram of a Ag doped Zn surface

Paper II

Journal of Materials Chemistry A

ARTICLE

Transformation and migration in secondary zinc-air batteries studied by *in situ* synchrotron X-ray diffraction and X-ray tomography

Received 00th January 20xx,
Accepted 00th January 20xx

DOI: 10.1039/x0xx00000x

www.rsc.org/

Mathias K. Christensen,[a] Jette Katja Mathiesen [b], Søren Bredmose Simonsen[a] and Poul Norby*[a]

There are numerous challenges associated with developing secondary Zn-air batteries regarding e.g. power density and cycle life. Some of the challenges are related to morphological changes in the anode during cycling due to combined electrochemical and chemical processes involved in the reversible Zn – ZnO transformation. We present a unique *in situ* synchrotron X-ray diffraction study, where a combination of time and spatial resolution allows information about transformation and transport in a Zn/ZnO anode during discharge/charge operation. By tracking Zn and ZnO reflections during cycling of two Zn-air batteries we see that the conversion of these phases is accompanied by transport into the anode and the anode configuration does not return to its initial state after recharge due to ZnO migration to other parts of the battery. During charge Zn metal is deposited as microcrystalline material, changing the morphology and phase distribution in the anode. The XRD results were supported by qualitative *in situ* X-ray computed tomography that confirms depletion of ZnO and non-homogeneous distribution of Zn.

Introduction

With the increasing prevalence of intermittent renewable energy generation, the need for energy storage is becoming more important. Batteries are already being used towards this purpose and are anticipated in the future to contribute to an even larger degree[1]. The two most common battery types for this purpose are Li-ion and lead-acid batteries because of their high capacity and low price, respectively. With the ever-increasing demand, a battery that provides high energy storage capacity at low cost is needed. The Zn-air battery is an ideal candidate, due to the low price of zinc metal[2] and the high theoretical specific energy (1300 Wh/kg). The specific energy obtained for current Zn-air batteries are reported between 350 and 500 Wh/kg[1,3,4]. Zn-air batteries obtain these high capacities due to the open nature configuration of the cell, where the cathode (O_2) is outside the battery, leaving only an air electrode, electrolyte, separator and the active material to contribute to the weight.

During discharge oxygen is reduced at the cathode:

$$O_2 + 4\,e^- + 2H_2O \rightarrow 4OH^-$$

The hydroxide ions migrate toward the anode and create zincate ions in the electrochemical reaction with Zn according to the reaction:

$$Zn + 4OH^- \rightarrow Zn(OH)_4^{2-} + 2e^-$$

Non-electrochemical precipitation of ZnO from zincate occurs according to:

$$Zn(OH)_4^{2-} \leftrightarrow ZnO + H_2O + 2\,OH^-$$

Yielding the overall reaction (which is thereby a combination of an electrochemical and a chemical reaction):

$$2\,Zn + O_2 \rightarrow 2\,ZnO$$

Zn has a long history of being applied in batteries and the Zn-air battery has been well-established commercially since 1933, although only as a primary battery as electrical rechargeability is challenging[5]. In order for secondary Zn-air battery technology to reach large scale application in the market it needs to have high cycle stability. Consequently, to achieve long cycle-life a number of challenges need to be overcome:

1. Obtain highly stable, efficient and bi-functional catalysts.
2. Reduce reaction of alkaline electrolytes with CO_2, which leads to precipitation of K_2CO_3 in the pores and thereby choking of the air electrode.
3. Improve water management to reduce evaporation.
4. Hinder zinc dendrite formation.
5. Reduce self-corrosion and hydrogen formation of the anode.
6. Control and anticipate shape/morphology changes and redistribution of material in the anode during discharge/charge cycling.

[a] Department of Energy Conversion and Storage, Technical University of Denmark, 4000 Roskilde (Denmark).
[b] Department of Chemistry and Nanoscience Center, University of Copenhagen, 2100, Copenhagen (Denmark)
[c]

* Corresponding author
Electronic Supplementary Information (ESI) available: [details of any supplementary information available should be included here]. See DOI: 10.1039/x0xx00000x

Shape changes in the negative electrode are caused by: 1) Chemical expansion occurring due to the reaction of Zn to ZnO, causing the anode to expand and contract during cycling. Chemical expansion is the reason why commercial primary Zn-air button cells have a headspace to accommodate volume expansion[6]. 2) Transport of Zn species happens because the conversion between Zn and ZnO occurs through dissolved zincate ions, enabling non-electrochemical deposition of ZnO. This could lead to redistribution inside the electrode or migration to e.g. the separator or positive electrode.

A secondary zinc-air cell would therefore experience not only expansion and contraction of the negative electrode but also morphology changes. Anodes need to be carefully designed and well understood to retain performance over many cycles. As shape changes and transport has a direct effect on the performance and reversibility of the Zn-air battery, this is an important parameter to investigate, and *in situ* studies are necessary in order to obtain detailed information in real time about the processes involved.

Zn-air batteries have been investigated with the aim of understanding the mechanism of both primary and secondary batteries. Schröder *et al.* has applied tomography to commercial ZA13 button cell primary batteries to verify simulation results and found that zinc oxide formation initially occurs close to the separator and that Zn particles closest to the current collector would oxidize last during discharge. Associated with the conversion of Zn to ZnO a structural expansion factor for the Zn electrode of 1.5 was found. [7]

In 2014 Arlt *et. al.* developed a Zn-air battery design suitable for x-ray computed tomography and used it to investigate electrolyte redistribution during discharge. They observed that flooding of the pores in the air electrode contributed to end of life for the cell[8]. Franke-Lang *et. al.* improved on the technique and demonstrated that modifying the density of the Zn-matrix in the anode to accommodate expansion could reduce the stress induced by the structural expansion. They also highlighted how parasitic reactions could result in gassing that would also deteriorate the anode [9].

Nakata *et. al.* investigated artificially grown zinc dendrites and their effect on cycle life. It was shown that the zinc dendrites can be completely dissolved using low oxidation currents. Later they used *in situ* X-ray diffraction (XRD) to investigate in-plane changes in the Zn electrode of a Zn/NiOOH battery and found that suppressing non-uniform Zn deposition would enhance cycle life.[10,11]

Zn/MnO batteries with an ionic liquid electrolyte have been investigated by Abad *et. al.* using synchrotron X-ray diffraction and XPS to study how Zn was converted to ZnO through a $Zn(OH)_2$ intermediate[12].

In the present study we investigate morphology changes in a Zn-air battery and redistribution through the anode using time- and spatially resolved synchrotron X-ray diffraction. The anode is a mixture of Zn, ZnO in a paste-electrode; addition of ZnO to the anode facilitates ZnO deposition as it provides additional nucleation sites[6]. The goal is to increase the understanding of the redistribution and transport in the paste anode and through this to be able to increase the cycle life of the battery.

Experimental

In situ battery cells

The capillary-based *in situ* battery cell used in these experiments consisted of two sizes of borosilicate capillaries (Hilgenberg GmbH) with an OD of 3 mm and 2.4 mm and ID of 2 mm and 1.6 mm, respectively. The anode and cathode were contained in two pieces of the smaller capillary, which were inserted in a piece of the larger capillary, using a glass fiber separator and held in place with UV-glue U3200 and U3600 Cyberbond. The anode current collector was a 1.8 mm Cu-wire, which were inserted in the bottom of the glass pieces and held in place by UV glue. The Cu-wire was polished on the top to provide a smooth surface. The anode paste was made from 49.3wt. % Zn (Umicore BIA100), 21.1 wt. % ZnO (Umicore Pharma B) 28.2 wt. % electrolyte and 1.4 wt. % Cekol 30000P (CP Kelco), sodium Carboyxmethyl cellulose, gelling agent[13]. The electrolyte was added to the powders immediately before use and the entire anode glass part was weighed to determine the capacity. The weight of the anode for the two batteries used (named Zn1 and Zn2) was 10 mg and 9.2 mg, respectively, which yields an initial capacity of 4.0 mA and 3.75 mA.

The cathode was made from $NiCo_2O_4$ and PTFE with a 0.5 mm thick Ni wire inserted into as a current collector. The cathode was prepared from a powder mixture of 85 wt. % $NiCo_2O_4$ powder (Cerpotech) and 15 wt. % PTFE (Sigma Aldrich) powder. The mixture was dispersed in 300 wt. % of isopropanol and homogenized using a magnetic stirrer for 10 minutes. The resulting slurry was filled into the capillary to a height of at least 1 cm and the nickel wire was inserted all the way through. The glass capillary with wet slurry and Ni wire was heated to 340 ° C for one hour in a furnace. The procedure was adapted from Wittmaier *et al*[14]. For XRD measurements at a synchrotron, the capillary cell was mounted in 3D printed PLA plastic frame, which holds the wires and contact clips (Figure 1a). The electrolyte was 6 M aqueous solution of KOH from pellets (Sigma Aldrich). The separator was made using 20 mm long 1 mm wide Whatman GF/A separator. The batteries were assembled immediately before being mounted at the beamline.

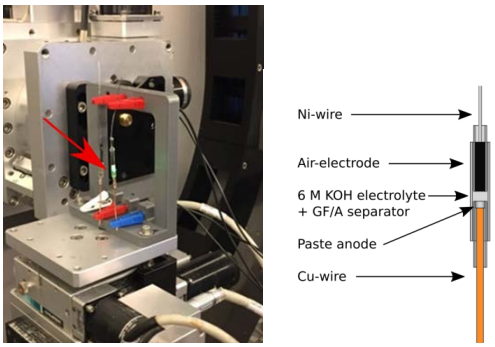

Figure 1a) The capillary cell mounted in the *in situ* XRD experiment, red arrow indicates the where the incoming interacts with the sample. b) Schematic illustration of the capillary Zn-air battery.

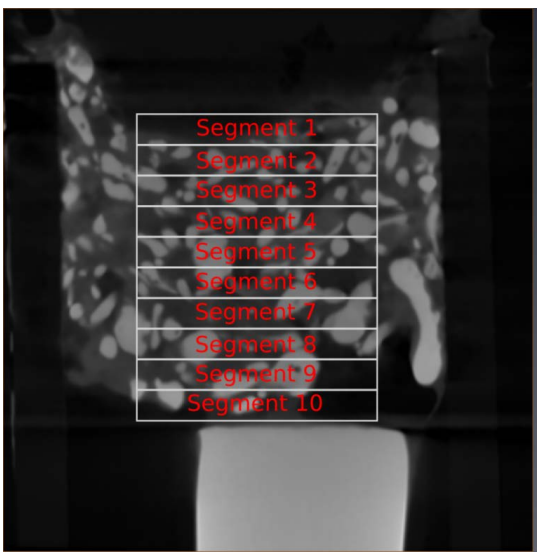

Figure 2: Cross section of a capillary cell anode that depicts the interaction volume with the beam designated as position 1-10 where 1 is closest to the separator. Position 10 is adjacent to the polished Cu wire.

Cells characterized by x-ray computed tomography (CT) were similar to the cells characterized by XRD, however, the anode and cathode current collector had a 63 µm diameter Cu wire attached by silver epoxy (Chemtronics) to allow for rotational freedom around the vertical axis of the cell. Similarly the Ni wire was glued to the side of the glass capillary to reduce the effect of torsion during rotation. The anode was contacted through the metal stage that held the sample.

Synchrotron X-ray diffraction

The *in situ* synchrotron X-ray diffraction experiments were performed at PETRA III, beamline P02.1. The X-ray beam was selected by a diamond 111 Laue crystal and a silicon 111 Laue crystal and collimated by slits. The wavelength was determined as 0.2072 Å using the diffraction pattern from a silicon standard (NIST). Diffraction data were collected using a PerkinElmer XRD1621 area detector (400 x 400 mm^2, pixel size 200 x 200 □m^2).

Time and spatially resolved diffraction data were collected with an X-ray beam defined by slits: vertically 0.2 mm and horizontally of 1 mm. The beam exposes between 8-10 points along the anode in a consecutive manner (Figure 2). The anode contains very fine-grained ZnO particles, which gives smooth Debye-Scherrer rings, and zinc metal powder with a wide size distribution, containing approximately 16 wt. % crystallites 425 µm. This results in very grainy Debye-Scherrer rings with over-exposed diffraction spots in the detector images.

Calibration of the sample-detector distance, tilt parameters, beam center etc. (using a LaB_6 standard sample) as well as reduction of the obtained 2D diffraction patterns, were performed using the DAWN software [15,16]. For data reduction a mask for the beam stop was used, as well as a threshold mask to eliminate over-exposed pixels from the large zinc crystallites. However, the presense of large zinc crystallites results in larger fluctuations in the integrated intensities for the zinc phase compared to the ZnO phase.

Data analysis: The presence of large Zn crystals, resulting in over-exposure of the detector, presents a challenge for the data analysis as the integrated intensity of diffraction peaks from the initial zinc crystallites do not necessarily quantitatively reflect the amount of crystalline material. For this reason, Rietveld or LeBail refinement of the diffraction data could not be used for extracting information about the relative and absolute amounts of the Zn and ZnO material present. Data analysis was performed using raw summation of selected diffraction peaks, subtracting a linear background determined at the ends of the integration interval and the diffraction patterns were normalized using background points. The synchrotron runs in top-up-mode, resulting in small fluctuations of the ring-current (ca 1%). The diffraction data were not corrected using the ring current due to the high stability of the ring current at the beamline.

For each position in the anode, see Figure 2, all the reflections from Zn and ZnO were identified and integrated between the selected boundaries as seen for sample two, position 2, in Figure S1. The resulting integrated intensities can be seen in Figure S3 for each of the reflections. In the following analysis we mostly focus on Zn (102) and ZnO (002) in several positions in each sample, but as can be seen in the supporting information (SI) the intensity variations are similar for the other reflections. Position 1 contains the interface between anode and electrolyte and displays intensity variations with time which are similar to those for position 2. However, the diffracted intensities are lower than for the other positions due to smaller amount of material in the beam. Also, volume changes in the anode move the electrolyte/anode interface resulting in significant intensity variations. The data from position 1 were not included in the analysis, but the time series can be found in in Figure S4 and S5.

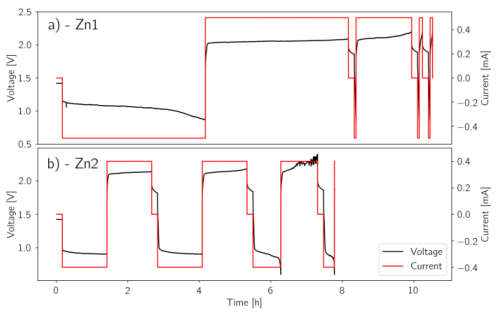

***Figure 3**:* Electrochemical cycling data for two batteries with a) 4 h of discharge/charge time, with 10 min OCV in between cycles and b) 1 h and 15 min of discharge/charge time with 10 min OCV between cycles.

In situ Micro X-ray CT

In situ X-ray micro Computed Tomography, µCT scans were conducted with an Xradia Versa XRM-410 instrument using a W reflection target. Scans were performed at a voltage of 140 kV, a power of 10 W, no filter, 4 x optical magnification, binning 4, an exposure time of 1 s and a total of 1451 projections over a 186° rotation, resulting in a pixel resolution of 4.5 µm. The acquisition of one tomogram was set to take ca. 1 hour, and 20 tomograms were recorded successively without breaks in between during cycling of the capillary Zn-air battery. The recorded data were reconstructed using Feldkamp-Davis-Kress reconstruction algorithm with a beam hardening constant of 0.05 and a smooth filter constant of 0.5. The commercial software AviZo was used for visualizations.

Post-mortem XRD

Post mortem in-house XRD conducted on the cathode and separator. ZnO was found in the separator along with other unidentified crystalline compounds. Some of these compounds are likely from reaction between the KOH and the glass fiber separator. In very long cycle experiments, these effects are detrimental to the battery as it dilutes the electrolyte and introduces potential contamination of the electrodes. Whatman GF/A was chosen for these experiments as it is easy to work with, holds electrolyte well and because the experiments are relatively short. No ZnO was observed in the cathode.

Results and discussions

Two Zn-air battery cells were investigated; Zn1 with a full discharge/charge cycle and Zn2 which was cycled using partial, time limited charge/discharge cycles with Open Circuit Voltage, OCV measurements in between cycles. In Figure 3 the electrochemical cycling profile for each of the battery cells are seen. Each battery cell has an initial OCV around 1.4 V. Battery Zn1 was discharged for four hours and charged for four hours at 0.5 mA. The total mass of the Zn1 anode is 10.0 mg yielding a capacity of 4.1 mAh resulting in a C-rate of 1/8. After the discharge/charge cycle no more discharge capacity was observed as the cell immediately hits the lower voltage limit of 0.85 V. An additional charge capacity was found as the battery was charged for 2 hours before hitting the upper voltage limit of 2.2 V. Battery Zn2 was cycled by discharging and charging at 0.4 mA for 1 h and 15 minutes three times with lower voltage limit of 0.6 V and upper voltage limit of 2.4 V. The mass of this anode is 9.2 mg resulting in a capacity of 3.76 mAh and a C-rate of 1/9. The discharge potential decreases for each cycle, and from cycle three the discharge capacity decreases and the battery hits the low voltage limit. The charge plateau is constantly around 2 V.

XRD

Following the normalized intensities of a Zn and ZnO peak over time in each sample it is evident that significant changes are taking place both in phase distribution and morphology of the zinc metal crystallites. From the raw detector images in Figure 4 the grainy nature of the Debye-Scherrer rings from Zn is clearly seen due to the large zinc crystallites (Fig. 4a). When looking at a series of raw diffraction images (Video included in Supplementary Information) it was observed that diffraction spots disappear and appear rapidly in the Debye-Scherrer rings indicating that the orientation of the individual Zn crystals changes quickly during the experiment. Because the anode paste is viscous any movement can affect the arrangement of the particles in the paste. Perturbations could be from gas evolution from parasitic reactions or from the aggregated effect of the entire electrode undergoing shape change. The dynamic nature of the crystallite orientation makes it impossible to mask out the individual reflections from the larger Zn particles.

A dramatic change in the Debye-Scherrer rings of Zn is observed from the initial sample (Figure 4a) to the recharged battery (Figure 4b). The final Debye-Scherrer rings of Zn after almost 6 hours of recharge (Figure 4c) are smooth and well defined as opposed to the grainy rings from the initial zinc powder. This shows that Zn is re-deposited as small crystallites.

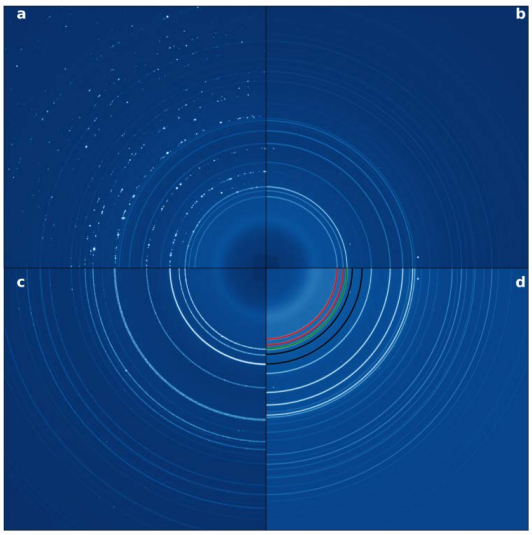

Figure 4: Cutout of detector images obtained during cycling of battery Zn1, position 2 (0.2 mm beneath the anode electrode interface) in the anode. a) Initial anode obtained during OCV. b) After 4 hours of discharge. c) After subsequent charging for 4 hours. d) A reference image to facilitate interpretation using highlighted Debye Scherrer-rings. Red: ZnO, Green: Overlapping reflection (Zn + ZnO) and Black: Zn.

Figure 5 shows the integrated intensities of the ZnO(002) and Zn(102) reflections as a function of time for position 2-5. In position 2, 0.2 mm below the anode electrolyte interface i.e. from the top part of the anode (Figure 5a) it is seen that despite the large particles, Zn is completely consumed within two hours of discharge while ZnO is deposited. In position 3, 0.4 mm below the interface (Figure 5b) Zn is consumed after almost 4 hours. Even further below the interface Zn is not entirely consumed during discharge (Figure 5c, d). The results show clearly that the degree of transformation (Zn → ZnO) is larger close to the electrode/electrolyte interface and that the reaction is initiated at the interface and propagate through the anode towards the current collector.

A similar behavior is observed during charge. ZnO is fully consumed within 2-3 hours in position 2 while in position 5, 0.4 mm deeper into the anode, ZnO is consumed after 4 hours of charge. Again it is observed that the reaction is fastest close to the electrode/electrolyte interface displaying a high degree of conversion, while deeper into the anode conversion is delayed. However, as seen in Figure 6, which shows the sum of the integrated intensities for all positions, a considerable amount of ZnO is consumed during the first 4 hours of charging, amounting to 115% of the amount produced during discharge. As the initial discharge was 4 hours and the operating current was the same during charge and discharge, some of the ZnO initially present in the anode paste must be consumed during charge. From Figure 6 it can be seen that the main reason for the discrepancy is found in the first hour of discharge, where the formation rate of ZnO is slower than expected. As the zinc oxidation process proceeds via a zincate anion, the delay may be caused by establishment of equilibrium and concentration gradients due to local pH variations. After the first hour of charge, the rate of ZnO formation during discharge is similar to the rate of ZnO consumption during charge, indicating a reversible Zn/ZnO conversion reaction.

The charge was continued for a total of 6 hours which resulted in a complete conversion of ZnO in the anode, Figure 6, showing that overall the charging process and oxygen evolution reaction is very efficient. However, a significant dependence of the conversion progress with position in the anode is observed. In the part of the anode closest to the separator (up to 0.8 mm into the anode) all ZnO is consumed within the first four hours, including the ZnO in the original paste. This shows that the conversion is very inhomogeneous, and that it is important to take into account the spatial variation in the conversion, when composing the anode mixtures. From Figure 5 it can also be seen that when ZnO is depleted the Zn signal levels off. However, close to the separator, e.g. in position 2, the amount of Zn continues to increase, although not at the same pace as when ZnO is present in the same layer. The fundamental mechanism of the Zn conversion that entails the soluble zincate ion is responsible for the migration. The electrolyte and remaining ZnO can both contribute to deposition of Zn in the electrolyte interface as when the concentration of the ion decreases. To enhance cycle life of an anode this should be taken into account.

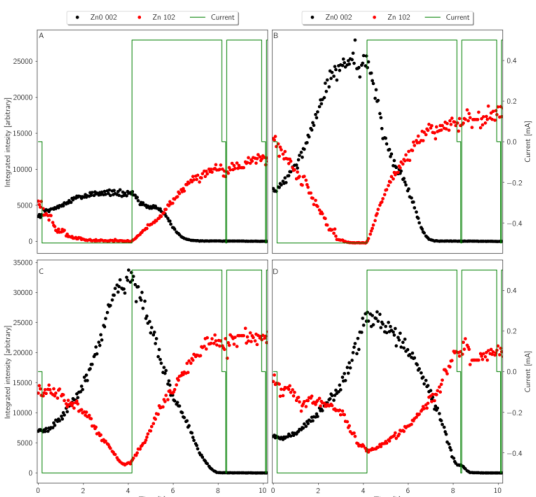

Figure 5. Integrated intensities of the red Zn (102) and black ZnO (002) reflections from battery Zn1 over time in different positions in the anode starting a): 0.2 mm (position 2), b) 0.4 mm (position 3), c) 0.6 mm position (4) and d) 0.8 mm (position5) below the anode electrolyte interface, the positions can be seen in Figure 2. The green line indicates the current in the battery.

A second *in situ* battery cell (Zn2) was investigated using three discharge/charge cycles with the current set to 0.4 mA and the

discharge and charge time reduced to 1 hour and 15 min. Ideally, the deposition and consumption during one charge/discharge cycle should match. However, as seen from Figure 7 ZnO is still consumed over time, although there is clearly re-deposition of ZnO during discharge. Especially close to the electrolyte the ZnO deposition during discharge is smaller than ZnO consumption during discharge resulting in an overall downward slope. The amount of Zn is closer to following the expected saw tooth pattern (0.2 mm and 0.4 mm below the separator) and is increasing slightly in this depth toward the end of the experiment. This indicates that there is a redistribution of materials over time, where Zn is accumulated in the top of the anode and ZnO is absent. In position 5, Figure 5d, 1 mm below the separator, which is halfway to the Cu-current collector, there is a slight change in the amount of ZnO and almost no variation in the amount of Zn indicating that ZnO is moving into the separator or possibly into the cathode as suggested by Franke-Lang *et al.*[8] If ZnO was deposited in the cathode it would obviously be undesirable. Redistribution of Zn and ZnO in the anode will severely limit how many cycles the anode can experience before it affects the performance of the cell, due to transport limitations or loss of nucleation sites and percolation. The solution could be to not utilize the full capacity of the anode and run asymmetrical currents or timescales during discharge and charge to avoid severe redistribution. The primary redistribution is removal of ZnO, which is controlled by the concentration of $Zn(OH)_4^{2-}$ in the battery, and lower currents, i.e. slower conversion rates could increase the homogeneity by giving more time for the intermediate to diffuse.

Looking at the battery as a whole, Figure 6, the amount of Zn and ZnO should be inversely correlated, when the intensities of the Zn and ZnO reflections from all positions are added. As seen in Figure 6a this is the case for 4 h cycling data, while it for the 1 h and 15 min cycles, Figure 6b, is less clear. It is however clear that the intensity of the ZnO (002) reflection is decreasing in both instances and the Zn (102) signals increase even after the ZnO is entirely depleted in the anode. This means that ZnO migrates from elsewhere in the battery and before being converted to Zn.

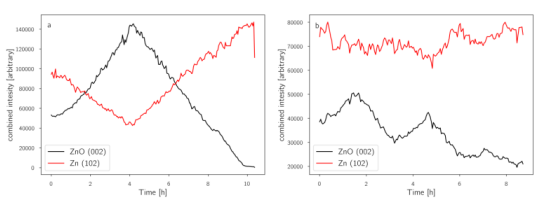

Figure 6: Accumulated intensities for Zn (102) and ZnO (002) in a) battery Zn1 and b) Zn2 over the entire anode as a function of time.

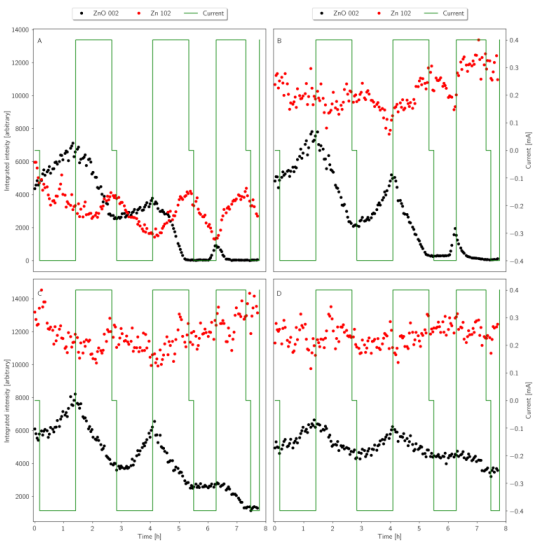

Figure 7 Sample Zn2 integrated intensities of Zn (102) and ZnO (002) signal over time in different positions in the anode starting a): 0.2 mm, b) 0.4 mm, c) 0.6 mm and d) 0.8 mm below the anode electrolyte interface. The green line indicates the current in the battery.

Quasi *in situ* X-ray CT

Figure 8 depicts the electrochemical data for the *in situ* tomography cell. The cell has a normal OCV of around 1.4 V, but on discharge there is a high overpotential as the cell voltage is close to 0 V. The voltage displays noise throughout the experiment in the order of 0.1 V. The noise and overpotential is likely related to poor oxygen transport into the cathode or loss of hydrophobicity in the cathode.

In the tomographic cross sections displayed in Figure 9, the density is displayed in grey scale where the densest material appears white and lighter materials appear dark. We therefore interpret the brightest regions as Zn particles and as the Cu current collector below, darkest regions as electrolyte and the intermediate contrast regions as ZnO. The initial paste contains large and sometimes elongated Zn-particles, while ZnO is much finer particles that are too small to be resolved and dispersed between the Zn particles in the slurry of ZnO and KOH. During discharge Zn is initially consumed in the top, leaving dark (electrolyte) areas in the top quarter of the anode. When the charging starts, Zn reappears in the interface with the electrolyte, although the particles are smaller and their boundary is less well defined as seen in Figure 9d. During the second discharge, seen in Figure 9e, the top of the anode dissolves to an even larger degree, leaving the anode hollow and dark. Unlike the end of the previous the discharge, the top part of the anode is no longer filled with ZnO, which agrees with the findings of the XRD measurements. During the second charge the Zn is redeposited, again as a porous mass. In the final tomogram collected two hours into the second charge, Figure 9f, the top of the anode appears darker indicating a low

content of ZnO. The larger Zn particles in the anode are not fully converted and the bottom part contains dark areas that might be small air bubbles from when the cell was assembled.

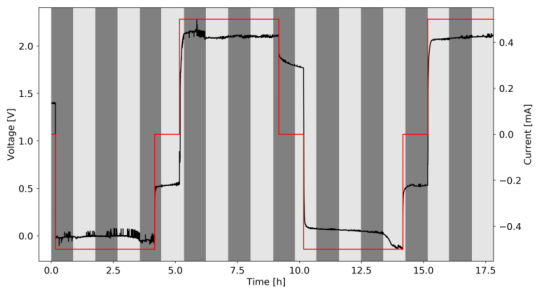

Figure 8: Electrochemical cycling data for the tomography battery with the alternating background shading displaying the duration of each tomogram.

In the rest of the anode, the large Zn particles have mostly disappeared and the ones that remain have fuzzy outlines, meaning that the surface has been converted at some point in the experiment. This is consistent with the XRD, which indicates that Zn is redeposited as fine particles. Throughout the entirety of the experiment there is no discernable gas build-up in the anode from corrosion of the Zn. In the final tomogram Zn is building up as bright spots in the top of the anode. Measuring the number of pixels the final tomogram, Figure 9f, ZnO is depleted to a depth of 0.42 mm. This is consistent with the XRD experiments on Zn 1 which show that after 4 hours of discharge, Zn is entirely depleted, in the top of the anode.

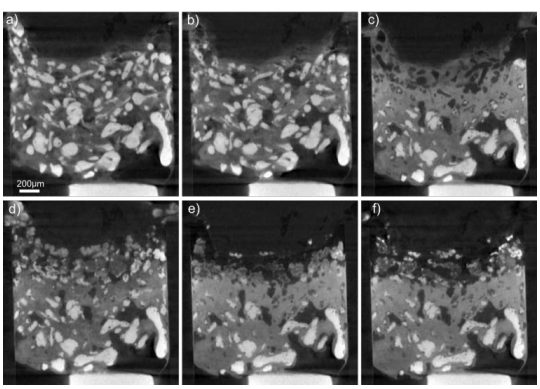

Figure 9: Ortho slices displaying a cross-section of the anode a) before discharge b) the second cross-section obtained after 104 minutes c) after the first discharge c) after the first charge, d) after the second discharge and e) during the second charge.

Conclusions

The conversion of Zn and ZnO during cycling of a zinc-air battery was investigated by spatially and time-resolved synchrotron X-ray diffraction and in-house X-ray tomography using an *in situ* capillary battery cell. The initial cathode consisted of a mixture of large-grained Zn and microcrystalline ZnO, which was added to facilitate nucleation of zinc oxide during discharge. By tracking the Zn (102) and ZnO (002) diffraction peaks over time for various positions along the anode it was possible to determine the redistribution of the active materials in the anode. It was shown that Zn and ZnO conversion initially happens in the top of the anode, i.e. closest to the cathode, and progresses downwards over time. Zn was initially present as large crystallites, but during charge it is redeposited as very fine microcrystalline material. Zinc oxide was totally consumed during the first charge in a large part of the anode closest to the electrode/electrolyte interface.

The results from the *in situ* diffraction experiment show that the phase distribution, composition, morphology and size distribution in the anode changes dramatically even after the first discharge/charge cycle. After several discharge/charge cycles the total amount of ZnO did not return to its original value, meaning that it is slowly removed from the anode and migrates to other parts in the battery. Using in-house post mortem XRD on cells after the *in situ* experiment it was shown that ZnO was present in the separator, but neither Zn nor ZnO was found in the cathode.

The observed anode materials redistribution during cycling was supported by in-house X-ray tomography on a similar capillary cell. It was seen that conversion primarily occurs closest to the electrolyte and by cycling, zinc is becoming the prevalent phase in the top part of the anode.

Conflicts of interest

There are no conflicts to declare.

Acknowledgements

We acknowledge DESY (Hamburg, Germany), a member of the Helmholtz Association HGF, for the provision of experimental facilities. Parts of this research were carried out at beamline P02.1 at PETRA III and we would like to thank Michael Wharmby for assistance in using beamline P02.1. The project was supported by DANSCATT and by MAX4ESSFUN, the European Regional Development Fund Interreg Öresund-Kattegat-Skagerrak (project DTU-039). Additionally, the 3D Imaging Centre at The Technical University of Denmark is gratefully acknowledged.

Notes and references

1. Li, Y. & Lu, J. Metal-Air Batteries: Will They Be the Future Electrochemical Energy Storage Device of Choice? *ACS Energy Lett.* **2,** 1370–1377 (2017).

2. Vesborg, P. C. K. & Jaramillo, T. F. Addressing the terawatt challenge: Scalability in the supply of chemical elements for renewable energy. *RSC Adv.* **2,** 7933–7947 (2012).
3. Davari, E. & Ivey, D. Bifunctional Electrocatalysts for Zn-air Batteries. *Sustain. Energy Fuels* 39–67 (2017). doi:10.1039/C7SE00413C
4. Xu, M., Ivey, D. G., Xie, Z. & Qu, W. Rechargeable Zn-air batteries: Progress in electrolyte development and cell configuration advancement. *J. Power Sources* **283,** 358–371 (2015).
5. Heise, G. W. Air depolarized primary battery. (1933).
6. Stamm, J., Varzi, A., Latz, A. & Horstmann, B. Modeling nucleation and growth of zinc oxide during discharge of primary zinc-air batteries. *J. Power Sources* **360,** 136–149 (2017).
7. Arlt, T., Schröder, D., Krewer, U. & Manke, I. In operando monitoring of the state of charge and species distribution in zinc air batteries using X-ray tomography and model-based simulations. *Phys. Chem. Chem. Phys.* **16,** 22273–22280 (2014).
8. Franke-Lang, R., Arlt, T., Manke, I. & Kowal, J. X-ray tomography as a powerful method for zinc-air battery research. *J. Power Sources* **370,** 45–51 (2017).
9. Schröder, D., Arlt, T., Krewer, U. & Manke, I. Analyzing transport paths in the air electrode of a zinc air battery using X-ray tomography. *Electrochem. commun.* **40,** 88–91 (2014).
10. Nakata, A. *et al.* Transformation of leaf-like zinc dendrite in oxidation and reduction cycle. *Electrochim. Acta* **166,** 82–87 (2015).
11. Nakata, A. *et al.* In situ Zn/ZnO mapping elucidating for 'shape change' of zinc electrode. *APL Mater.* **6,** (2018).
12. Abad, J. *et al.* A synchrotron x-ray diffraction and hard x-ray photoelectron spectroscopy study of Zn negative electrodes at different charge and discharge states of Zn/MnO2batteries using an ionic liquid-based gel polymer electrolyte. *J. Power Sources* **363,** 199–208 (2017).
13. Mainar, A. R., Iruin, E., Colmenares, L. C., Blázquez, J. A. & Grande, H. Systematic cycle life assessment of a secondary zinc – air battery as a function of the alkaline electrolyte composition. (2018). doi:10.1002/ese3.191
14. Wittmaier, D., Cañas, N. A., Biswas, I. & Friedrich, K. A. Highly Stable Carbon-Free Ag/Co3O4-Cathodes for Lithium-Air Batteries: Electrochemical and Structural Investigations. *Adv. Energy Mater.* **5,** 1–8 (2015).
15. Filik, J. *et al.* Processing two-dimensional X-ray diffraction and small-angle scattering data in DAWN 2. *J. Appl. Crystallogr.* **50,** 959–966 (2017).
16. Basham, M. *et al.* Data Analysis WorkbeNch (DAWN). *J. Synchrotron Radiat.* **22,** 853–858 (2015).

Supporting information

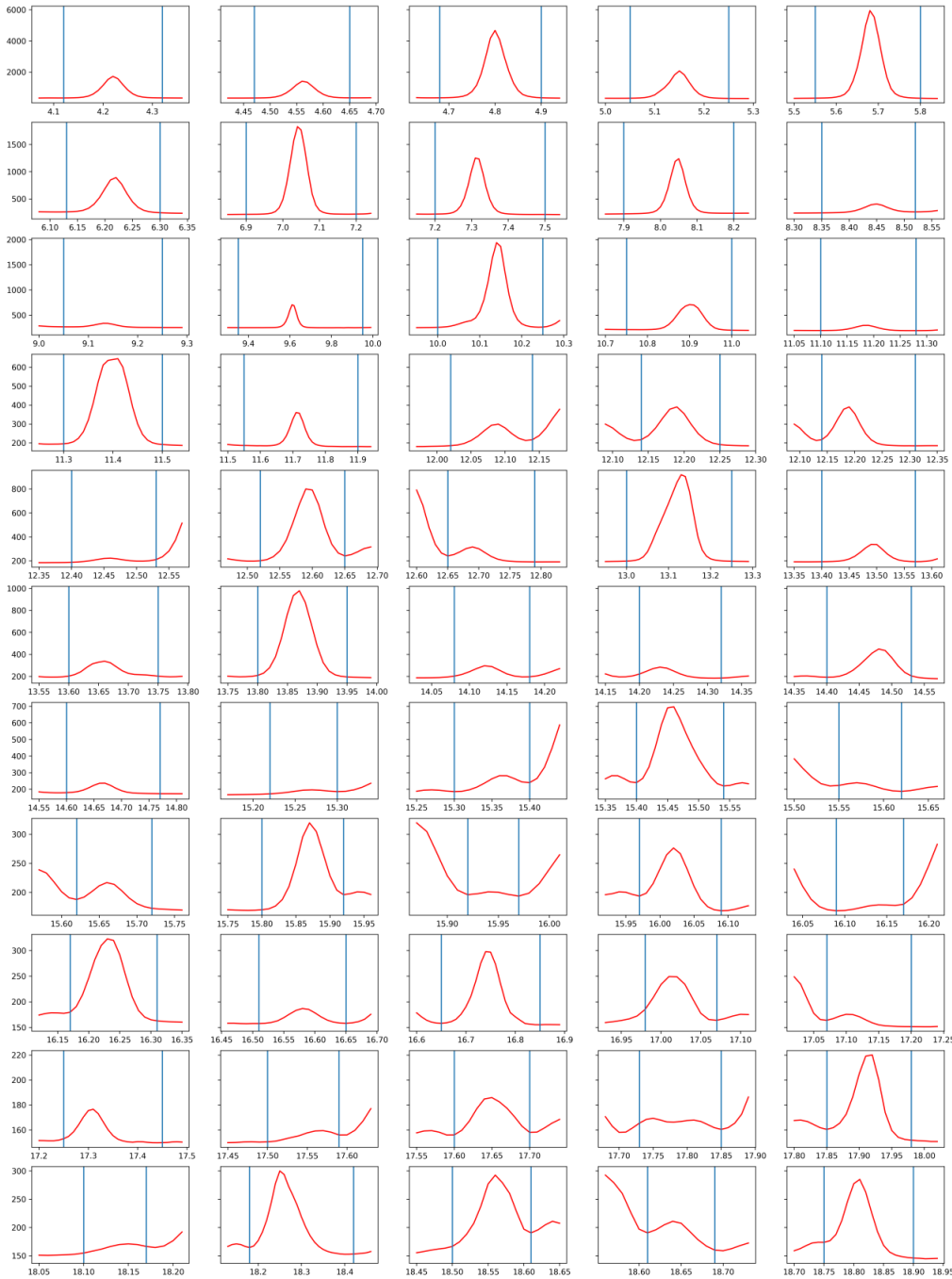

Figure 1: All of the significant reflections in the diffractomgram obtained in a single slice of the anode during the experiment. The vertical lines indicate the borders used to calculate the aggregated intensities for the given peak.

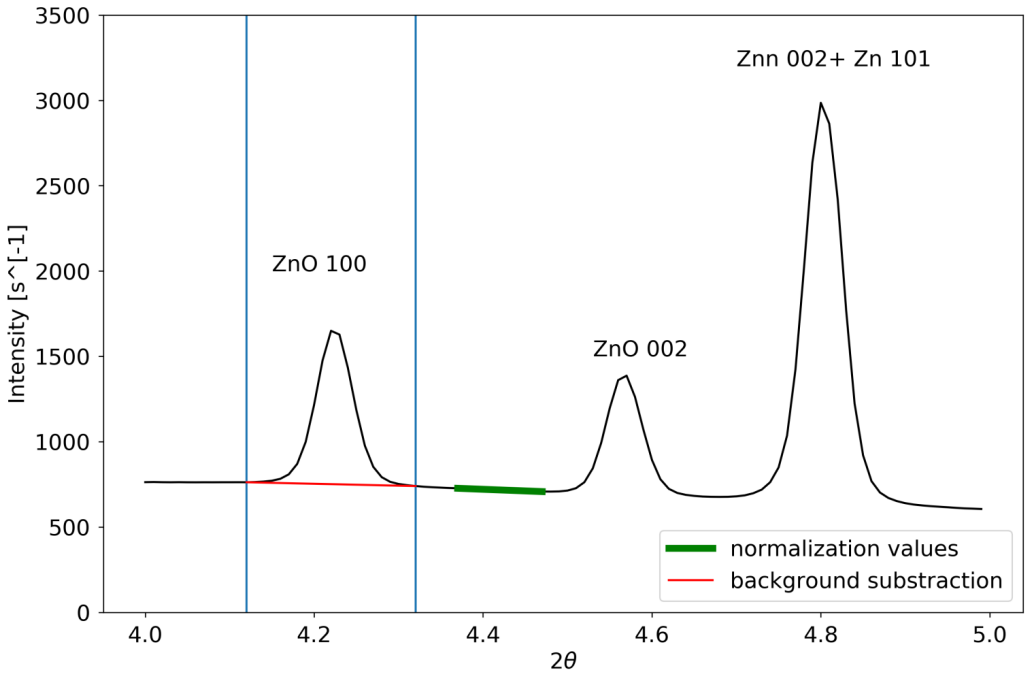

Figure 2. Example of XRD data show a peak is identified at the points used for normalization.

The pixel detectors have some challenges with "after glow", i.e. higher intensity parts of the detector are not entirely cleared in the read-out process, and may contribute in the following images. With regular intervals (10 minutes) a dark image was collected and used to partially compensate for this effect.

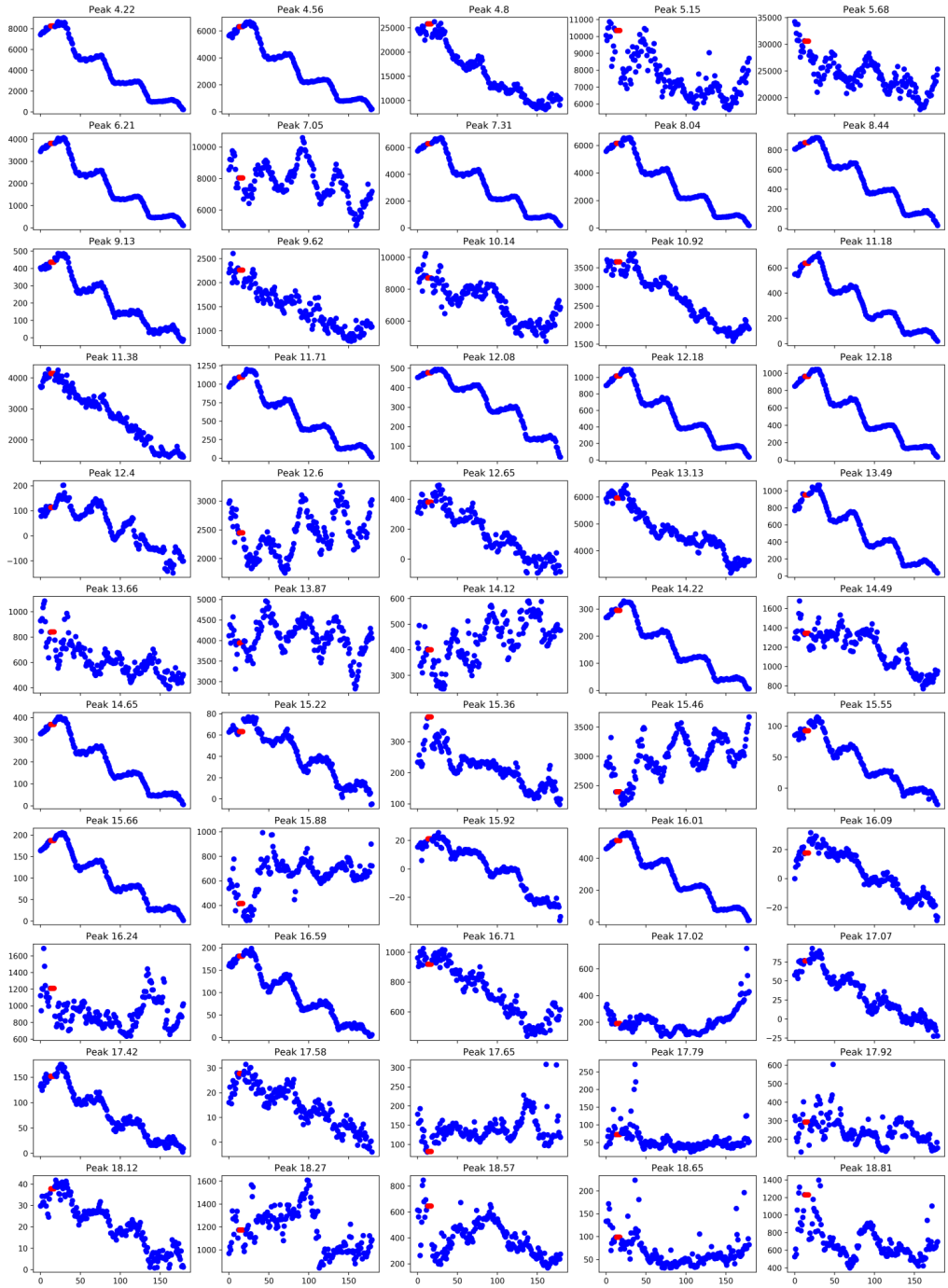

Figure 3: The aggregated intensities of each reflection in a single slice of the anode during the entire experiment. Red points indicates placeholder data, due to incorrect dark image correction.

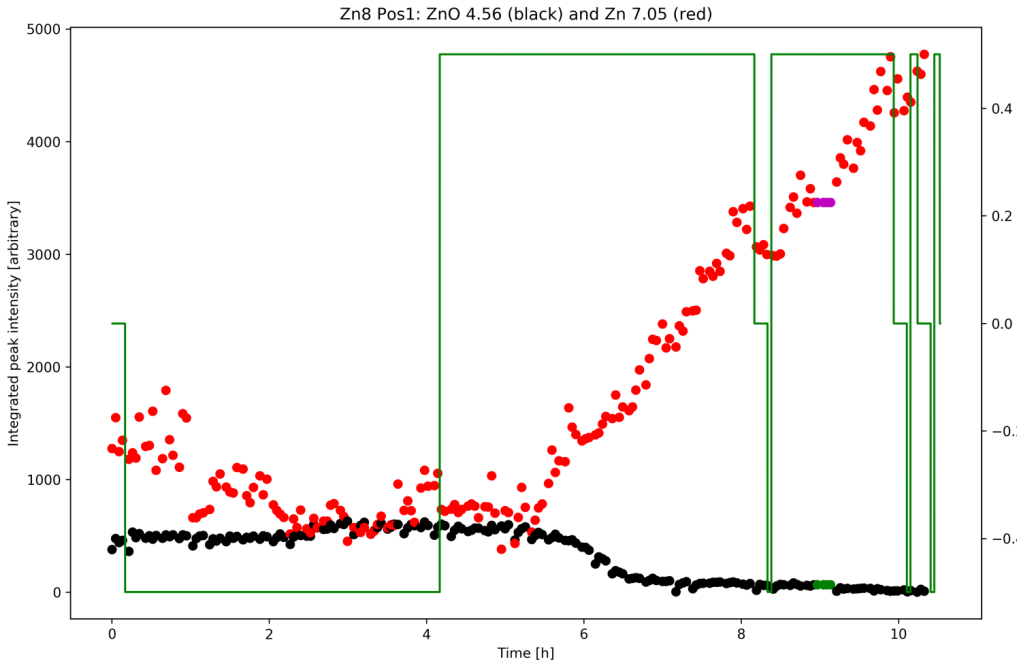

Figure 4 Integrated intensities of Zn (102) and ZnO (002) signal over time in Anode electrode interface in sample Zn1, green and purple points are placeholder data due to incorrect dark image correction.

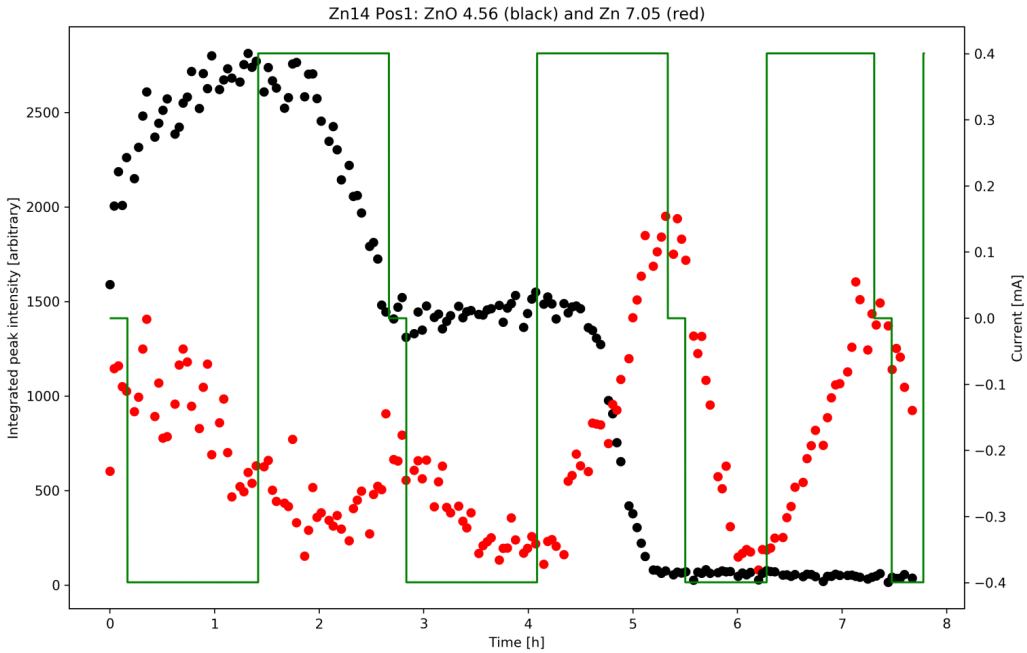

Figure 5 Integrated intensities of Zn (102) and ZnO (002) signal over time in Anode electrode interface in sample Zn2

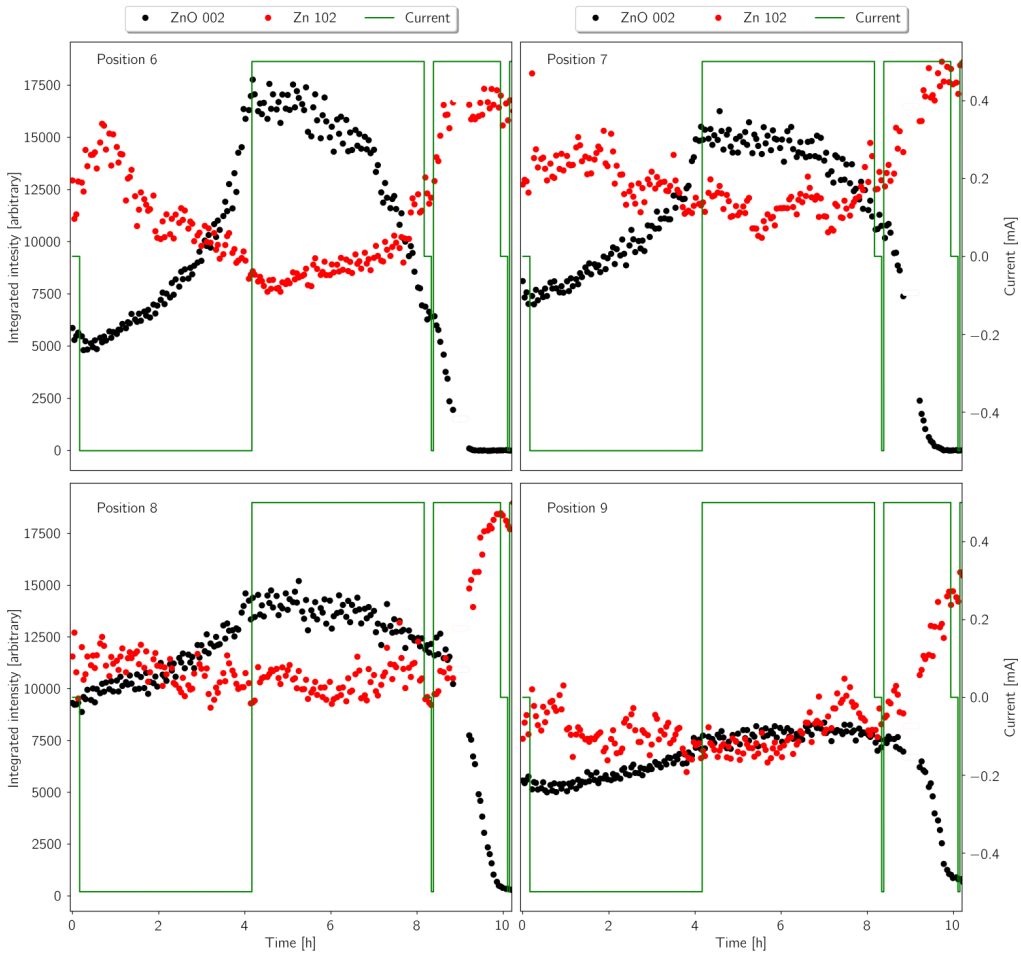

Figure 6. The bottom four position closest to the current collector for sample Zn1. Position 6 is between 1.0-1.2 mm below the electrolyte interface. Position 7 is between 1.2-1.4 mm below the electrolyte interface. Position 8 is 1.4-1.6 mm below the electrolyte interface. Position 9 is 1.6-1.8 mm below the electrolyte interface.

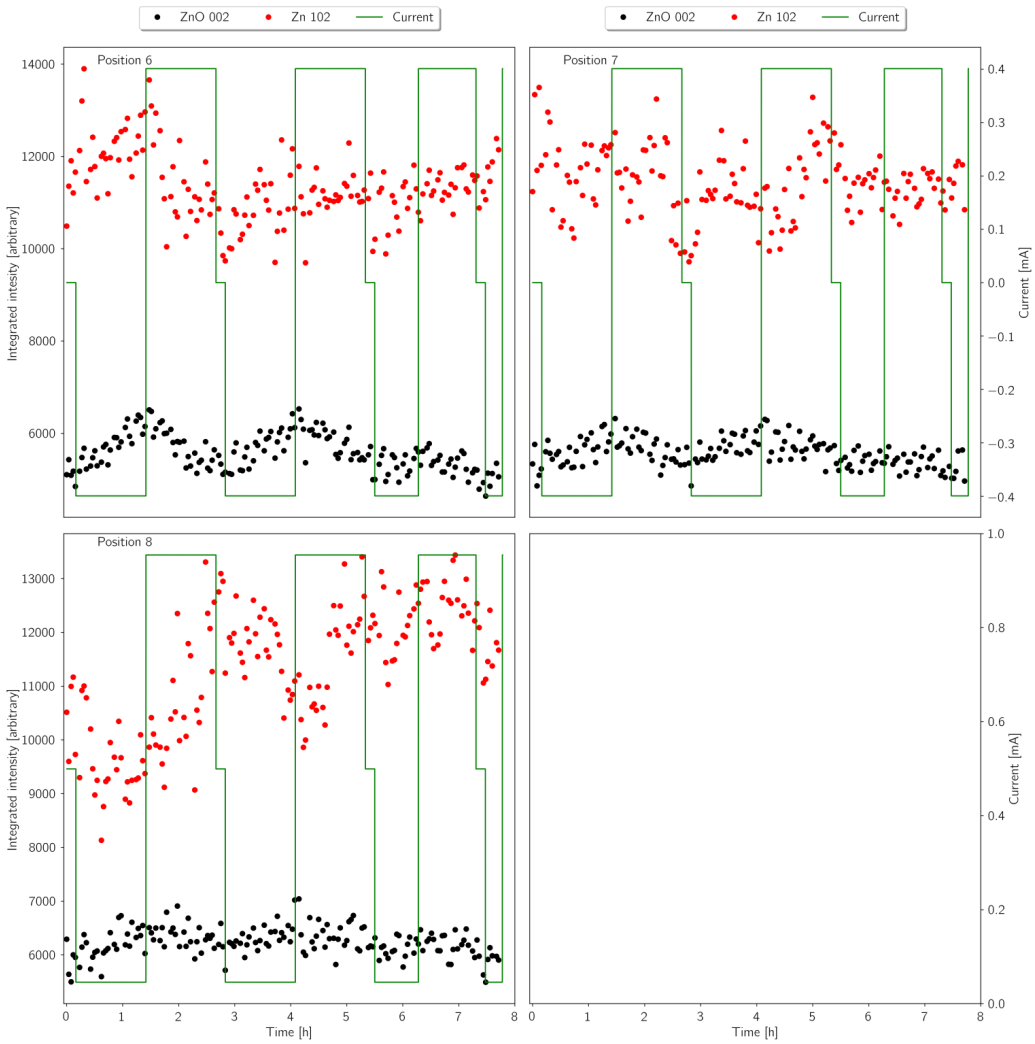

Figure 7. The three position closest to the current collector for sample Zn2. Position 6 is between 1.0-1.2 mm below the electrolyte interface. Position 7 is between 1.2-1.4 mm below the electrolyte interface. Position 8 is 1.4-1.6 mm below the electrolyte interface.

Paper III

DEMS investigation of Alkaline Zn-air batteries

Mathias K. Christensen[a] and Poul Norby[a]*

[a] Department of Energy Conversion and Storage

Technical University of Denmark, 4000 Roskilde (Denmark)

Email: M. K. Christensen: mkch@dtu.dk, P. Norby: pnor@dtu.dk

ORCID: P. Norby 0000-0002-2590-7050

Introduction

Electrochemical energy storage has received increasing attention in recent years due to the increasing prevalence of intermittent renewable energy. A solution such as pumped hydroelectricity is the largest contributor to stored energy, but this technology is hard to implement in some locations. Electrochemical energy is therefore considered to become increasingly important for this role. There is a variety of possible solutions such as the lead-acid battery or the Li-ion, where the focus is increasingly on the latter. However, both of these technologies are reaching their limit [reference] and sufficient availability of raw materials such as Co, for current Li-ion batteries is not certain. Other electrochemical devices such as metal-air batteries or organic flow batteries could provide high capacity, low cost storage with relatively abundant materials. Metal-air batteries while attractive due to their high energy storage capacity are difficult to realize. Additionally, they are not considered ideal for vehicular or mobile applications due to power limitations and need for air purification. Zn-air batteries are considered the most commercially successful as they have been commercially available as primary batteries since 1933[1]. The theoretical specific energy is about 3 times higher than current Li-ion batteries, although practical applications are roughly comparable. However, for these batteries to obtain a central role as secondary batteries and energy storage devices improved energy efficiency, higher power density and long cycle life are required. Currently this is limited by self corrosion, dendrite formation, CO_2 absorption in the air electrode and the need for high performance bi-functional catalysts for ORR (Oxygen reduction) and OER (Oxygen evolution) reactions.

To gain insights into these problems *in situ* techniques can be applied to elucidate various effects. X-rays can be applied to find structural or surface information. Methods such as Rotating disc electrode, RDE, can be applied to characterize and quantify what species are in solution. This has been done e.g. by Goh *et al,* who investigated an Ag nanoparticle-MnO_2 air electrode and determined the electron transfer numbers for this catalyst to be 3.7 during ORR [2]. Hu *et. al.* studied a similar Ag-MnO_2/Single Wall carbon nanotube catalyst and

found values between 3.4 and 3.8[3]. This was suggested to originate from the MnO catalyst's slight affinity towards partial oxidation of O_2 to HO_2^-, a two electron reaction[4]. While Ag provides excellent activity towards the 4 electron pathway for ORR[5], it is not ideal for alkaline Zn-air batteries as Ag enhances the self-corrosion when mixed into the Zn-surface[6]. In the present paper we apply Differential Electrochemical Mass Spectrometry DEMS[7,8] to investigate gas output and composition and determine the electron transfer numbers of full Zn-air batteries using pressure measurements and mass spectrometer analysis. Using this setup it is possible to determine the electron to oxygen ratio using the formula:

$$n_{e^-/O_2} = \frac{\Delta Q * R * T}{\Delta P * V * F}$$

Where Q is the charge passed during the measurement, F is faradays constant, P is the pressure, R is the Ideal gas constant and T is the temperature in K. In practice rather than calculating these numbers by insertion, a pressure line is created and linear regression is used to determine n_{e^-/O_2} from agreement between the calculated and measured pressure profiles.

Experimental

Two Zn-air batteries were assembled in an ECC-Air-Ni battery test cell from EL-Cell Gmbh and tested galvanostatically in a two-electrode configuration. The anode was a 18 mm diameter, 0.125 mm thick 99.95 % pure Zn foil (Goodfellow) punched out using an MTI disc cutting tool. The anode was placed on 99.99% pure 8 μm thick Cu foil from MTI Corp. The electrolyte was 200 μL 6 M KOH made from >85 % pure KOH pellets (Sigma Aldrich). Two Whatman GF/A separators were used.

The cathode was made with 39 wt % $NiCo_2O_4$ powder(Cerpotech), 23 wt % Ni powder (Strem Chemicals, 3-7μm), 23 % Ni powder (Alfa Aesar, 150-200 mesh) and 15 wt % PTFE (Sigma-Aldrich) with a total loading of 157 ±25 mg cm^{-2}. The powders were dry mixed, compressed at 3 bar per 18 cm^2 onto a Ni 40 mesh (Alfa Aesar) and heated at 340 ^{O}C for 1 hour. Each cathode was cut to 18 mm diameter on a MTI disc cutting tool.

The electrochemical cycling was conducted using galvanostatic cycling at 2.54 mA (1 mA/cm^2 for the electrodes) for 4 hours with voltage limits of 0.95 V and 2.2 V. The cycling was preceded by 1 h of OCV measurement. Battery 1 had 40 minutes of wait time between each transition to check for leaks. For battery 2 the cell was purged for 1 h before the charge started to remove trace O_2. The gas evolution that was collected in the headspace of the cell was collected and quantified every 10 minutes throughout the 4 hour charge. To quantify the gas evolution using the mass spectrometer the volumes of the setup and the EL-cell were determined using calibration gasses using known quantities of the relevant gasses.

Results and discussion

The first Zn-air battery was cycled 3 times at $1mA/cm^2$ while connected to a hermetically sealed compartment of the DEMS setup filled with pure O_2. The cycling profile can be seen in Figure 1, where a flat discharge plateau above 1.3 V is observed in all three cycles although the voltage decreases to just below this value after the full discharge time. During charge there is a slight shoulder in the charging profile above 1.8 V before stabilization into a plateau that starts at 1.94 V and increases to almost 2 V by the end of the charge. Between the first charge and second discharge there is a shoulder similar to the one for the first charge. This shoulder is found to be to related to the cathode: When a charged air electrode is transferred to a pristine battery it displays the same feature around 1.7V before the initial discharge. This indicates that the surface of the air electrode is slightly oxidized during charge and needs to be reduced before discharge. In the subsequent charge cycles the profile is the same with slight increases in overpotential as the cycle number grows.

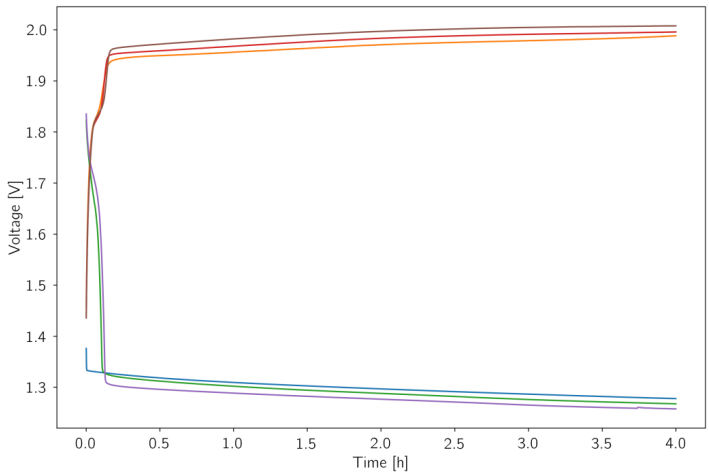

Figure 1: Electrochemical cycling data for a Zn-air battery cycled in pure oxygen 3 times at 1 mA/cm^2.

The pressure measured during this cycling can be seen in Figure 2. It is seen that the pressure increases slightly initially during the during the OCV measurement, which is likely caused by H_2 evolution. The total pressure increases during this time is 4 mbar. After 1 hour the discharge starts and the pressure decreases linearly for 4 hours. After the 40 minute wait time (not shown) the pressure had increased slightly by 4 mbar similar to the pressure increase during OCV. When the charge begins there is a brief time where the pressure does not increase after which the pressure increases linearly. The pressure delay is related to the shoulder in the voltage profile during charging again indicating an electrochemical process not involving gaseous species. The general trend in the pressure development is similar in the following two discharge charge cycles but there is an increase in pressure during the experiment. The pressure cannot be explained by variations in temperature (shown also in Figure 2). The monitored temperature increase seen after 12 hours is related to the morning sun

hitting the laboratory, thereby increasing the temperature.

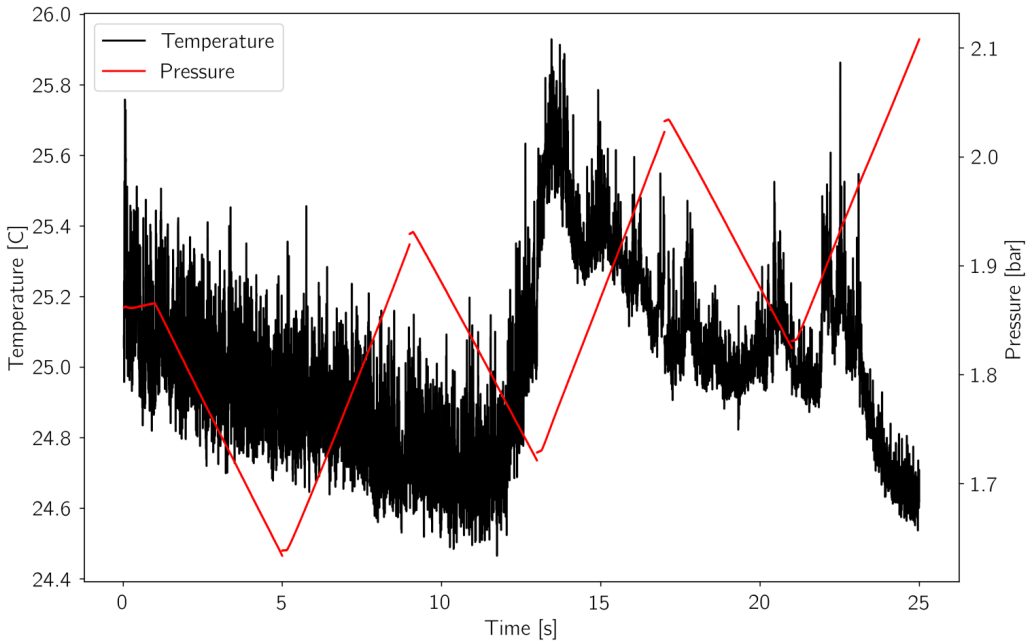

Figure 2 Temperature (black) and pressure (red) development 1 h OCV measurement followed by 3 discharge/charge cyles of a Zn-air battery at 1 mA/cm^2. Not shown: 40 wait minutes between each discharge and charge.

Using the accumulated data the electron to charge ratio can be calculated using the formula described above. The charging profile is only calculated for the part of the plot where we know there is gas evolution and consumption, meaning that during the discharge and charging the observed shoulders where no gas evolution/consumption is observed are omitted in the fit. Including these would result in an artificially low charge to oxygen ratio. Having determined the H_2 evolution during OCV and assuming it is constant, as indicated by the wait time between the discharge and charge, it is possible to correct for the hydrogen evolution. The correction method is exemplified in Figure 3 which shows the pressure measured and the

corrected pressure curves for first cycle of Battery 1. The additional pressure due to hydrogen evolution is estimated from extrapolation of the pressure during OCV and subtracted from the pressure curves.

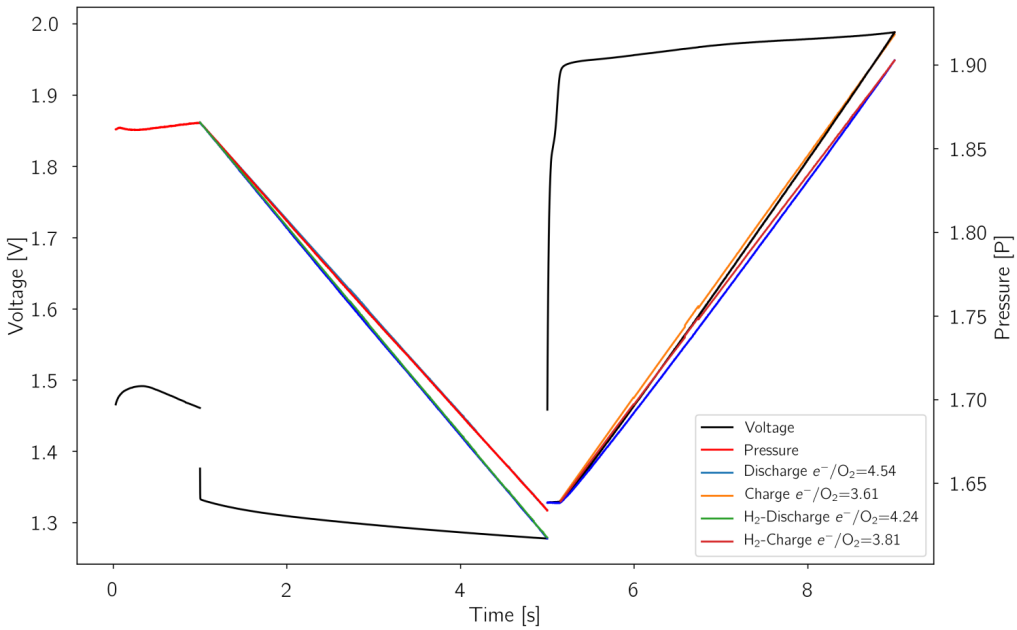

Figure 3 Voltage and pressure profiles for battery 1 during the first cycle with calculated pressure lines given with and without H_2 correction. The obtained e^-/O_2 numbers are shown in the legends.

By constructing a similar cell and subjecting it to same cycling parameters using the mass spectrometer to determine O_2 evolution during charge we can obtain e/O_2 values during charge for comparison with the values obtyained from the pressure measurements. The cycling profiles for this cell is similar to the battery 1 apart from slightly higher overpotentials (Figure SI1). The resulting H_2 and O_2 gas evolution can be seen in Figure 4. When the charge starts the O_2 signal increases but does not reach a plateau until after 2 hours of charging despite the fact that the voltage reaches ORR potentials within the first hour. This is due to the volume of the

EL-cell used in this experiment, which is large compared to the amount of gas evolved. H_2-evolution is observed even before the charge starts, indicating that H_2 is related to self-corrosion in a chemical process rather than an electrochemical one. The derived e^-/O_2 ratios from the pressure experiemnts as well as for the DEMS measurements during charge can be seen in Table 1.

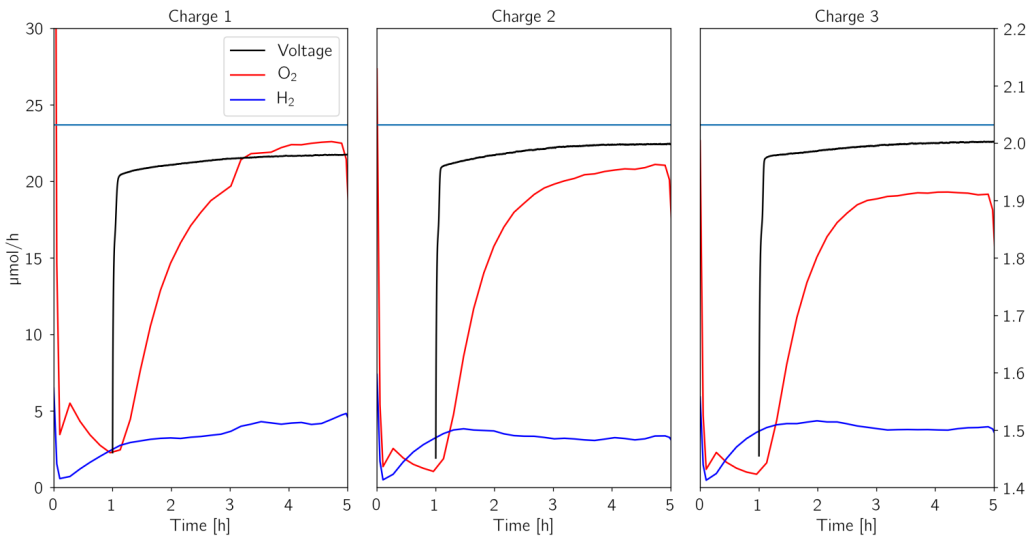

Figure 4 O_2 (red) and H_2 (blue) evolution along with the voltage profile for each charge. The blue horizontal line in each frame indicates the expected O_2 from a 4.0 e^-/O_2 ratio.

From the uncorrected e^-/O_2 ratios from the pressure experiments it is seen that the ratios get progressively worse as the cycle number increases. The high ratios during discharge are indicative of a deficit of gas consumption, i.e. the pressure signal changes to *little*, which indicates that there are competing electrochemical reactions. During charge the e^-/O_2 ratios are below 4, as a result of the gas pressure increasing more than expected from the oxygen evolution reaction.

The values corrected for H_2-evolution are closer to the ideal value, but especially during discharge the number becomes progressively worse while charge numbers are more stable. It is beyond the capability of this setup to identify processes which do not produce gasses. It is also not possible to determine if this process originates from the anode or the air-electrode. No other gasses aside from H_2, O_2, Ar and H_2O were detected by the MS.

	Measured e^-/O_2		H_2 corrected e^-/O_2		DEMS e^-/O_2
	Discharge	Charge	Discharge	Charge	Charge
Cycle 1	4.54	3.61	4.24	3.81	4.21
Cycle 2	4.79	3.50	4.49	3.68	4.53
Cycle 3	4.83	3.49	4.50	3.83	4.93

Table 1 e/O_2 collected Zn-air batteries during discharge and charge, with and without H_2-correction. The last column is determined by the mass spectrometer.

From the DEMS data during charge the e^-/O_2 ratios were derived from the ratio between the oxygen evolution rate calculated using the 4-electron oxygen evolution process and the observed oxygen evolution rate, Figure 4. As seen in Table 1 the values found are consistently higher than 4, in contrast to the values determined from the pressure experiments. However, as seen from Figure 4 hydrogen is also detected and the combined pressure would result in e^-/O_2 ratios below 4.

Conclusion

Full Zn-air batteries with $NiCo_2O_4$ and Ni air electrode and a Zn foil anode were tested and in the DEMS setup and e^-/O_2 numbers were determined during discharge and charge using pressure measurements while accounting for H_2-evolution from self-corrosion of the anode. For these batteries the numbers were 4.24 and 3.81 e^-/O_2 for the first cycle while the third and final cycles yielded 4.50 and 3.83 e^-/O_2 indicating that the ORR gets progressively harder while OER is roughly the same. Using mass spectrometry the oxygen evolution during

charge was quantified and showed significantly higher electron numbers, above 4 e^-/O_2. Hydrogen was detected by the MS during charge and when taking this into account an agreement with the electron numbers determined from the pressure experiments was found.

Comparison between the results from the pressure and the DEMS experiments shows that while pressure experiments are very efficient for determination of electron numbers for electrochemical reactions involving gas formation care must be taken to identify and quantify all reactions taking place. By combining quantitative mass spectrometry and pressure evaluation a better understanding of the performance of the cells electrodes can be obtained.

Bibliography

1. Heise, G. W. Air depolarized primary battery. (1933).
2. Goh, F. W. T. *et al.* Ag nanoparticle-modified MnO2 nanorods catalyst for use as an air electrode in zinc-air battery. *Electrochim. Acta* **114,** 598–604 (2013).
3. Hu, F. P., Zhang, X. G., Xiao, F. & Zhang, J. L. Oxygen reduction on Ag-MnO2/SWNT and Ag-MnO2/AB electrodes. *Carbon N. Y.* **43,** 2931–2936 (2005).
4. Liden, D. & Reddy, T. *Handbook of batteries*. *Cell* (2004). doi:10.1016/0378-7753(86)80059-3
5. Spendelow, J. S. & Wieckowski, A. Electrocatalysis of oxygen reduction and small alcohol oxidation in alkaline media. *Phys. Chem. Chem. Phys.* **9,** 2654–2675 (2007).
6. Lysgaard, S. *et al.* Combined DFT and Differential Electrochemical Mass Spectrometry Investigation of the Effect of Dopants in Secondary Zinc–Air Batteries. *ChemSusChem* **11,** 1933–1941 (2018).
7. Højberg, J. Fundamental mechanisms in Li-air battery electrochemistry. (Technical University Of Denmark, 2015).
8. Højberg, J. *et al.* An electrochemical impedance spectroscopy investigation of the overpotentials in Li-O2 batteries. *ACS Appl. Mater. Interfaces* **7,** 4039–4047 (2015).

Supporting information – DEMS investigation of Alkaline Zn-Air batteries

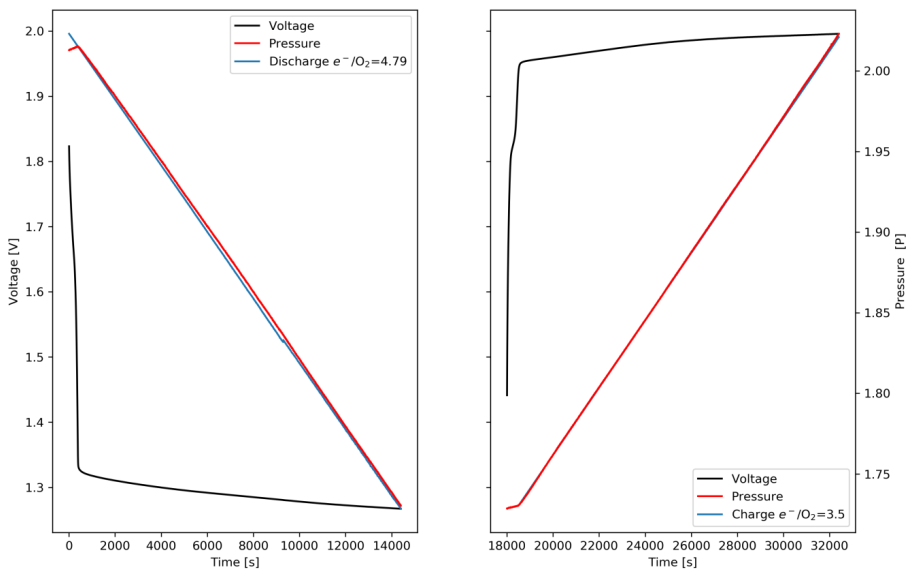

Figure 1: Voltage and pressure data used to obtain e/O_2 numbers for a Zn air battery in its second cycle without H_2 correction

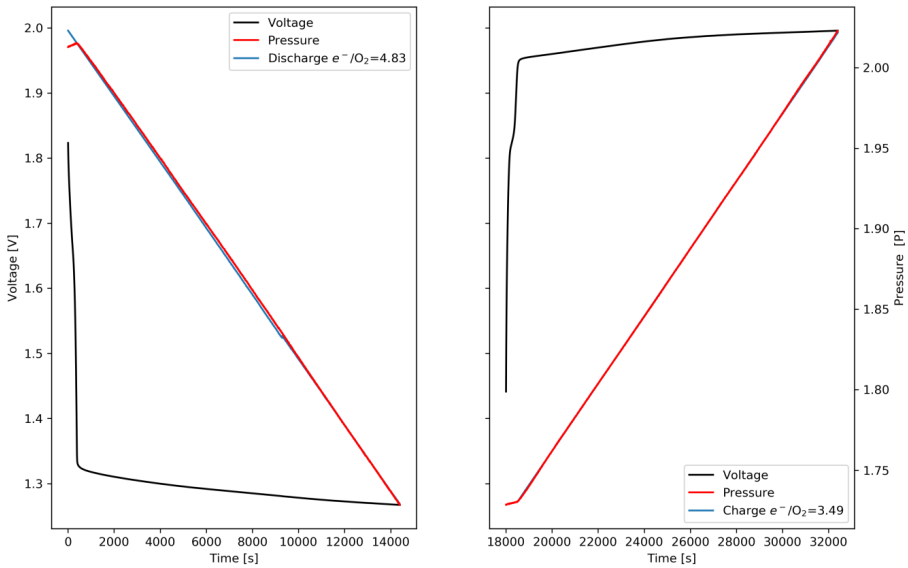
Voltage
Pressure
Discharge e^-/O_2=4.83
Voltage [V]
Time [s]
Voltage
Pressure
Charge e^-/O_2=3.49
Pressure [P]
Time [s]

Figure 2

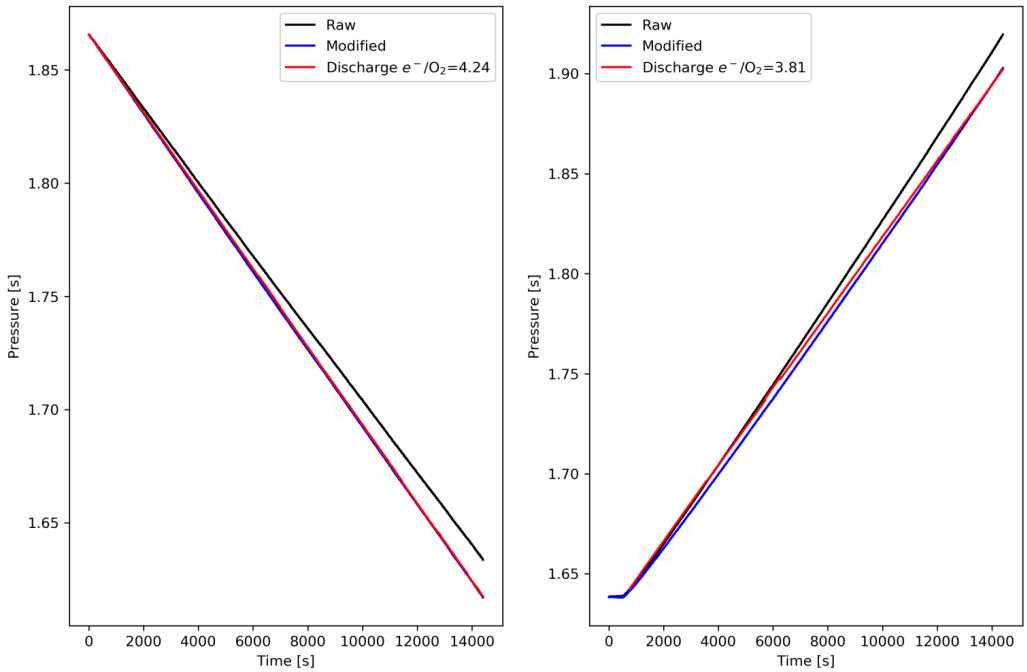

Figure 3 Voltage and pressure data used to obtain e/O_2 numbers for a Zn air battery in its first cycle without H_2 correction

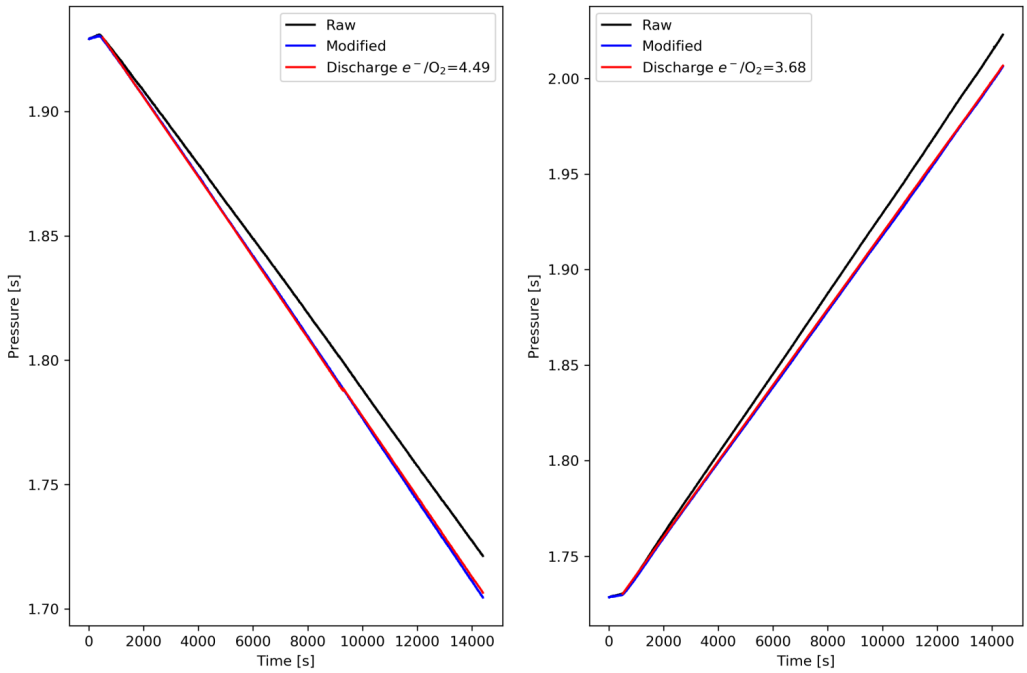

Figure 4 Pressure data used to obtain e/O_2 numbers for a Zn air battery in its third cycle with H_2 correction

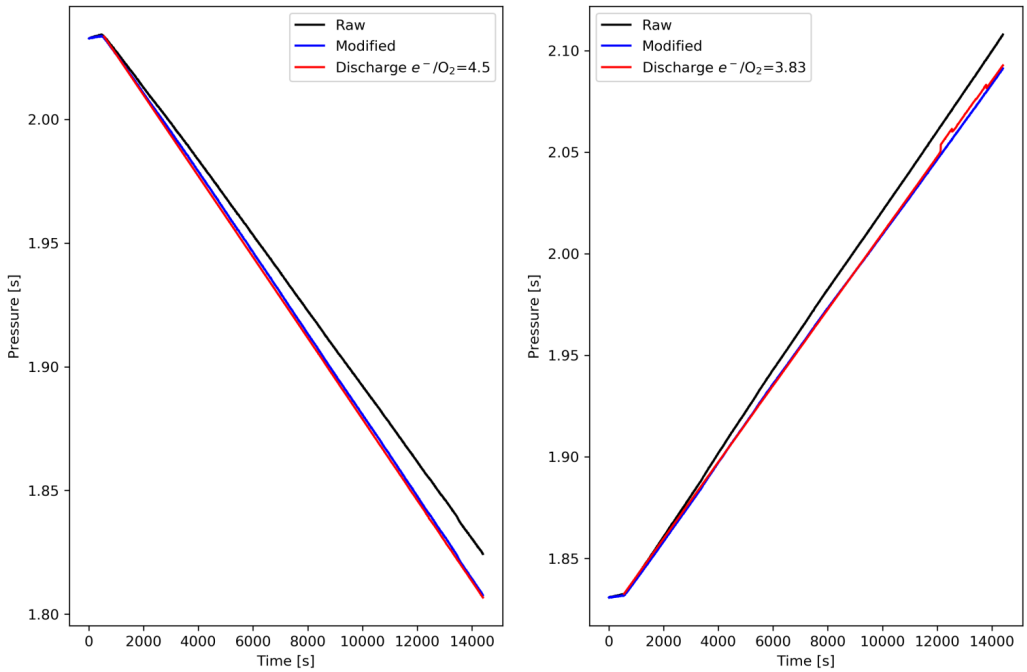

Figure 5 Pressure data used to obtain e/O_2 numbers for a Zn air battery in its third cycle with H_2 correction

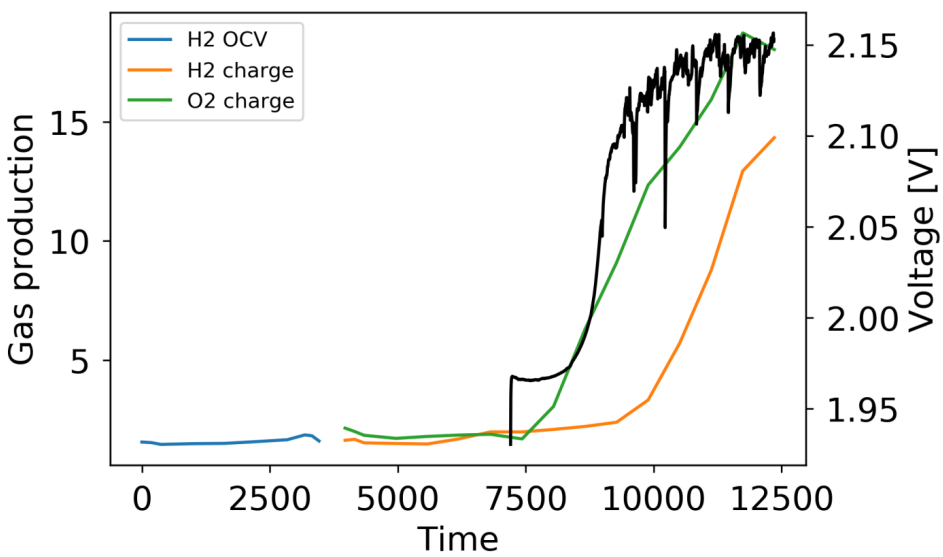

Figure 6 Hydrogen and Oxygen data for a Zn-Plate with no air-electrode during OCV and and charge.